Copyright Statement

Interdisciplinary study of hydrodynamic and biogeochemical processes of a large-scale river plume

Robert A. McEwan

School of Marine Science and Engineering

University of Plymouth

A thesis submitted to the University of Plymouth in partial fulfilment for the degree of

Doctor of Philosophy

February 2013

Abstract

Interdisciplinary study of hydrodynamic and biogeochemical processes of a large-scale river plume

Robert A. McEwan

This research has utilised the Massachusetts Institute of Technology general circulation model (MITgcm) along with observations taken as part of the River Influences on Shelf Ecosystems (RISE) study to investigate the dynamic processes associated with the Columbia River plume at different temporal and spatial scales.

Firstly, a high resolution (δx=δy=25 m) investigation of the near-field plume was undertaken using the fully non-hydrostatic mode of the MITgcm. This resulted in the reproduction of a detailed inner plume as well as a series of radiated internal waves. In addition to first mode internal waves, second order waves were radiated from the plume boundary when propagation velocity becomes sub-critical. Third mode internal waves were also observed, trapped at the plume head. The fine plume structure produced revealed secondary fronts within the plume that also generated internal waves. These features increase the mixing occurring inside the plume, resulting in greater entrainment of underlying waters into the plume. The use of Lagrangian drifters within the model produced detailed results of the recirculation taking place within the emerging plume and how this recirculation changes with

depth. This has implications for the near-field recirculation of biologically important solutes present in the plume waters.

A second coarser resolution horizontal grid (δx=δy=500 m) was implemented to investigate the processes of the large-scale plume with the addition of wind forcing. Experiments with both simplified and realistic wind scenarios were carried out and comparisons with in-situ data were made. This revealed the dominance of wind effects on the outer plume and tidal effects on the inner plume. In the simplified wind cases, the classical theory of plume propagation under the action of upwelling and downwelling favourable winds was recreated. For the case of realistic winds, there was some success in reproducing a hindcast of the plume location. Tracer fields were used to represent nutrient concentrations based on observed data. Whilst these results showed variations from observations, they did allow a spatially and temporally complete view to be taken of nutrient distribution in the region.

Acknowledgements

I would like to begin by thanking my supervisors, Dr. Vasiliy Vlasenko, Dr. Nataliya Stashchuk and Dr. Maeve Lohan, for their guidance and knowledge throughout my Ph.D. Their generous time and support has been an important feature throughout my Ph.D.

I would also like to thank my family Alex, Edith and Andrew McEwan for their support and encouragement during my many years of study, which have culminated in this thesis. Special thanks also goes to Sabine for being there through all the ups and downs that a Ph.D. entails.

Finally, I would like to thank all my friends, colleagues and teachers throughout the years that have helped me in numerous small ways to reach this point.

Declaration

At no time during the registration for the degree of Doctor of Philosophy has the author been registered for any other University award without prior agreement of the Graduate Committee. This study was financed by a studentship from The University of Plymouth.

Relevant scientific seminars and conferences were attended at which work from this thesis was presented. One paper has been submitted for publication and a second is currently in preparation.

Word count of main body of thesis: 25,000

Signed .....

Date .....

Publications - Submitted and in preparation:

Vlasenko, V., Stashchuk, N., **McEwan, R.A.**, (under-review) High-resolution modelling of a large-scale river plume. Ocean Dynamics.

McEwan, R.A., Vlasenko, V., Stashchuk, N., Lohan, M., (in prep) Large scale dynamics and nutrient distribution of the Columbia River plume.

Technical reports:

McEwan, R.A., Ford, D., Quantification of biophysical feedbacks and their impact on ocean physics, Met Office technical report, 2011.

Oral presentations:

McEwan, R.A., Lohan, M., Stashchuk, N., Vlasenko, V. - Where's the chemistry? Numerical modelling of nutrient distribution within a large-sale river plume. 2^{nd} Annual Biogeochemistry Centre Conference, Plymouth, UK, 17^{th} December 2010.

McEwan, R.A., Lohan, M., Stashchuk, N., Vlasenko, V. - Modelling the dynamics of a large-scale river plume and their effect on nutrient distribution. JONSMOD 2012, IFREMER, Brest, France, 21^{st}-23^{rd} May 2012.

Poster presentations:

McEwan, R.A., Stashchuk, N., Lohan, M., Vlasenko, V. - Non-hydrostatic effects in a propagating large-scale river plume. 14^{th} Biennial Challenger Conference for Marine Science, Southampton, UK, 6^{th}-9^{th} September, 2010.

McEwan, R.A., Lohan, M., Stashchuk, N., Vlasenko, V. - Modelling nutrient distributions in a large-scale river plume. EGU General Assembly 2011, Vienna, Austria, 3^{rd}-8^{th} April, 2011.

McEwan, R.A., Lohan, M., Stashchuk, N., Vlasenko, V. - Modelling nutrient distributions in a large-scale river plume. AMEMR III, Plymouth, UK, 27^{th}-30^{th} June, 2011.

Courses attended:

Alpine Summer School XVIII: Buoyancy Driven Flows. Aosta, Italy, 21^{st} June - 30^{th} June, 2010. Directors, Claudia Cenedese (WHOI, Woods Hole, MA, USA), Eric Chassignet (FSU, Tallahassee, FL, USA), Jacques Verron (LEGI, Grenoble, France).

Internship:

Met Office Summer Internship, Ocean forecasting, June-September, 2011.

Contents

List of Figures

LIST OF FIGURES

List of Tables

LIST OF TABLES

Chapter 1

Introduction

In this chapter, the motivation, aims and the objectives of this project are outlined and the presentation of the thesis is described.

1.1 Study motivation

Human interaction with the ocean is greatest at the coast. In 2008 52% of the contiguous United States population lived in coastal watershed counties (U.S. Census Bureau, 2010). The coastal regions of the oceans, into which rivers flow, are of special interest as rivers transport fresh water containing terrigenous material, including nutrients and pollutants into the ocean. This means that as well as changing the physical properties of coastal regions, river plumes can also affect the regional ecology, which has implications for water quality and fisheries.

The Columbia River by volume, is the fourth largest river in the United States and the largest source of fresh water to the Eastern Pacific. The Columbia River as well as discharging large volumes of fresh water into the Pacific is also a source of dissolved silicate and iron to the region (Lohan and Bruland, 2006).The plume has been shown to significantly alter nutrient supply and primary productivity rates as well as enhance export of material from productive coastal regions (Hickey et al., 2010).

Mixing processes between the plume and surrounding waters are complex and understanding them is crucial as the plume can strongly influence the biogeochemical cycling in the region (Kudela et al., 2010). These processes can be examined in detail by the utilisation of high resolution 3 dimensional numerical modelling. Due to wind stress, strong tides and ambient currents, it is expected that transport at an eastern boundary such at the Oregon-Washington coast will be high. It is therefore of interest

to investigate the effect of different forcings on the Columbia River plume and how they affect the distribution of plume waters and dissolved constituents across the shelf.

1.2 Aim and objectives

In order to establish an understanding of the dynamic processes of the Columbia River plume at several scales, a numerical modelling approach with comparison to in-situ measurements is required. To achieve this, the following aims and objectives were set: Aim **(1)** To thoroughly investigate the vertical and horizontal structure and mixing effects produced by the Columbia river plume, including investigation of internal waves generated by the plume, analysis of mixing processes affecting the plume, determining the importance of non-hydrostaticity in modelling the plume and identifying a detailed understanding of near-field circulation. Aim **(2)** of this study was to determine the nature of the large-scale dynamics of the plume under the action of wind forcing, including the description of the plume response to upwelling and downwelling winds, investigation into the effect of realistic wind forcing and the influence of plume dynamics on the nutrient circulation associated with the plume.

The necessary objectives to achieve aim **(1)** were:

- Use a high resolution model to resolve the detailed structure of internal waves generated by the plume.
- Analyse model output to determine the importance of entrainment and detrainment processes on mixing at the plume boundary.
- Generate and compare high resolution output from hydrostatic and non-hydrostatic model runs, in order to identify the role which non-hydrostatic effects play in plume dynamics.
- Utilise Lagrangian tracers within a high resolution model to identify the multi-layer circulation induced by the moving the plume.

In order to successfully address aim **(2)**, the necessary objectives to be accomplished were:

- Using a large area model produce upwelling and downwelling responses to a typical wind stress.
- Generate a month long hindcast of the larger plume region using realistic forcing and compare to in-situ measurements.
- Introduce a passive tracer field into the model to represent nutrients and compare with collected data.

1.3 Thesis structure

This thesis is arranged into a series of chapters in the following way. The 'Review chapter', Chapter 2, considers some of the relevant areas of importance to river plume study by reference to current literature on the subject. The third chapter entitled 'The Columbia River plume' focuses on the Columbia River plume and examines all aspects relating to its dynamics and importance to the region. This includes an analysis of the important forcings that will be later used in the modelling investigations. The 'Methodology' chapter, Chapter 4, describes the equations and assumptions utilised by the model. Chapter 5 presents the high resolution near-field investigation results that were the outcome of the first study objective including how the model was set up, and interpretation of the results and their significance. The second study objective is addressed in Chapter 6, which includes the results of the large-scale modelling investigation and the comparison with observational data. The final chapter, Chapter 7, summarises the findings of this study and presents some suggestions as to how this work may be built on in the future.

Chapter 2

An introduction to river plume dynamics

This chapter discusses some of the foundation as well as the most current research into river plume processes. Here, the importance of river plumes as an area of study is shown by presenting the literature relating to this field.

2.1 Plume fronts

River plumes are buoyancy driven surface flows and can be found in many of the world's coastal regions. When less dense river water of low salinity flows into more saline, denser coastal water, a spreading buoyant lens with a sharp interface to the ambient water is produced from the river mouth. Depending on wind and tidal conditions, these plumes may transport material for large distances alongshore or offshore, due to the pressure gradients created by differences in density of the converging waters. As a result, river plumes are important to the circulation of waters over the continental shelf (Simpson, 1982).

River plume water properties tend to differ from the surrounding coastal waters in many ways, including: salinity, temperature, dissolved constituents, suspended matter and biological content. The transport of riverine nutrients and pollutants across large areas of coastal ocean makes the understanding of river plume dynamics an important field of study, due to their potential to significantly influence the highly productive and diverse coastal zones (Jickells, 1998). Coastal areas, into which significant volumes of relatively fresh river or estuarine water flows, are often referred to as Regions of Fresh Water Influence (ROFI's) as the physical properties and dynamics of these areas are significantly modified by the presence of river outflow (Simpson, 1997*b*).

2. AN INTRODUCTION TO RIVER PLUME DYNAMICS

If freshwater discharge is significantly large or mixing and advection significantly weak, then a river plume can change the long-term properties of the regional coastal waters. In many cases, the differing optical properties of plume and coastal waters means that at the surface the plume can often be visible. River plumes have been observed optically and through measurements of temperature and salinity for many years. Remote sensing has been used to describe the variability in plume shape (Fiedler and Laurs, 1990; Walker, 1994). In-situ observation of the three dimensional plume structure is difficult, due to the large areas involved and rapidly changing system. Nevertheless, early studies such as Garvine and Monk (1974) have helped define the vertical structure of plume fronts. The use of simplified Laboratory experiments such as those undertaken by Stern et al. (1982); Griffiths and Hopfinger (1983) and Huq (2009), have enabled the identification of processes, which cannot be isolated via in-situ observations alone. Further to this, numerical modelling experiments have been used to investigate the detailed processes involved in river plume circulation at a range of length scales (Garvine, 1982, 1987; Chao, 1990; Garvine, 1998).

The fate of the plume waters is determined by a number of factors, including the rotational force of the earth, tides, wind, and bathymetry. If the width of the buoyant current is greater than the internal Rossby radius of deformation, it is turned to the right (in the northern hemisphere) and flows along the coast (Wiseman and Garvine, 1995). Where downwelling favourable winds prevail, the flow is further constrained to the coast becoming a deeper narrow flow that travels with increased velocity along the coast. When the wind direction produces upwelling conditions, the alongshore flow is reduced and the plume becomes shallower and spreads offshore. Several modelling investigations show that, in the absence of wind forcing, an anticyclonic bulge of recirculating plume water forms (Chao and Boicourt, 1986; Oey and Mellor, 1993; Kourafalou et al., 1996*a*). This bulge expands offshore as a result of mixing which reduces coastal propagation speed and has been observed at the Columbia River (Hickey et al., 1998; Horner-Devine,

2009), and for the Hudson River (Chant et al., 2008). Whilst some modelling studies use simplified forcing, investigations such as Kourafalou et al. (1996*b*) on the south-east U.S. have been successful in using realistic wind and tidal forcing in determining the fate of river discharge.

The narrow coastal current can be of three forms as described by Yankovsky and Chapman (1997), depending on inflow width, inflow velocity, inflow depth, reduced gravity and the Coriolis parameter. Firstly, a surface-advected plume in which the bottom boundary layer does not transport buoyancy offshore. Secondly, a purely bottom-advected plume and a third intermediate case.

2.2 Mixing in plumes

Mixing of plume waters is important as the balance of entrainment and detrainment affects the buoyancy of the plume with respect to the surrounding waters. Since the plume is a buoyancy-driven, flow these effects alter the propagation of the plume. The bulge created by the plume can spread offshore when mixing reduces the coastal propagation speed relative to the estuarine propagation speed (Horner-Devine, 2009). Mixing is also important biologically as it allows nutrient-rich waters to be brought up into the euphotic zone increasing primary productivity (Lohan and Bruland, 2006). The River water is mixed by the wind and tides, and over time is turned into shelf water. This process begins within the estuary where tidal mixing is dominant and continues within the plume where wind mixing is significant (MacCready et al., 2009). The presence of bathymetric features such as the Astoria Canyon also results in mixing produced by internal tides. Mixing is also generated by shear with the surrounding waters as the plume propagates. Much of this mixing occurs behind the turbulent head of the gravity current as described by Simpson (1997*a*) and shown in Figure 2.1. Experiments carried out by Britter and Simpson (1978) show that Kelvin-Helmholtz billows formed on the

front of the head are responsible for much of the mixing. Observations recorded by Orton and Jay (2005) of the Columbia River plume show downwelling velocities of up to 0.35 m s^{-1} and strong mixing behind the head with eddy diffusivity of O(0.2 m^2 s^{-1}). High levels of mixing behind a plume head have also been observed in a small plume, with mixing being modulated by the estuarine tidal outflow and across frontal velocity (Pritchard and Huntley, 2002). It has been observed that a highly stratified estuarine front thins and accelerates creating greater vertical shear which leads to turbulent mixing (MacDonald and Geyer, 2004).

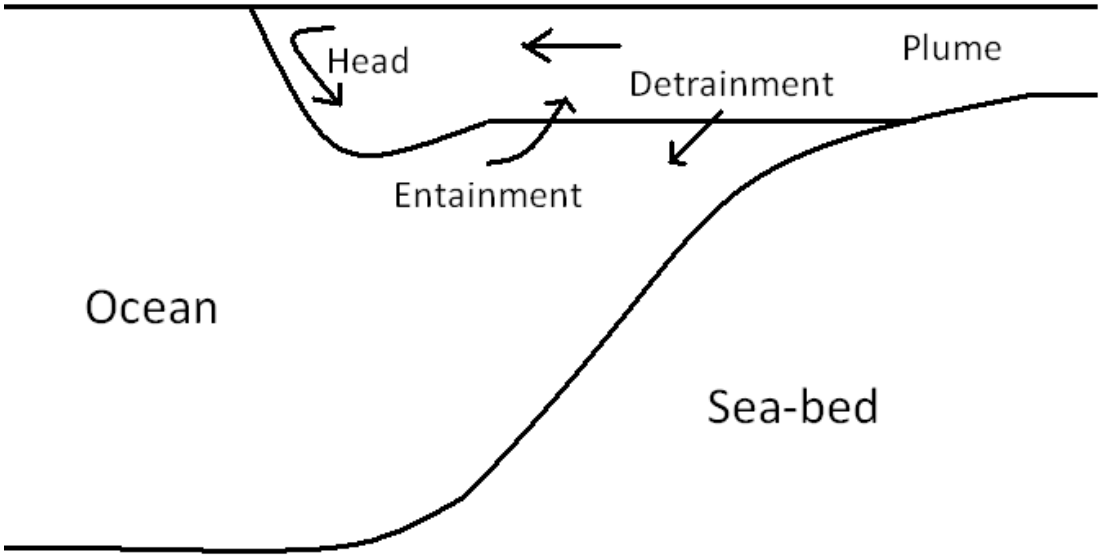

Figure 2.1: Schematic cross section showing plume head shape and location of mixing

2.3 Dimensionless analysis of stratified flows

Stratified flows may be estimated by using a variety of dimensionless parameters, such as Froude numbers and Richardson numbers. The Froude number is used to define critical flow conditions and the Richardson number is used to define mixing conditions.

In the following sub-sections, the versions of Froude and Richardson numbers used in this investigation are defined.

2.3.1 Froude numbers

The Froude number is the ratio of a flow velocity to a gravitational wave velocity and is defined as,

$$Fr = \frac{V}{c} \tag{2.1}$$

where V is a characteristic velocity and c is the propagation velocity of a water wave. For surface waves, wave velocity is given by $c = \sqrt{gh}$. For internal waves, which are propagating along the interface between two water layers, the wave velocity is given by $c = \sqrt{(\Delta\rho/\rho)gh}$, so the Froude number then becomes,

$$Fr = \frac{u}{\sqrt{(\Delta\rho/\rho)gh}} \tag{2.2}$$

where h is the surface layer height. When the Froude number is less then 1, the flow is sub-critical and when greater than 1, it is super-critical. When the Froude number approaches 1, an internal hydraulic jump may occur.

2.3.2 Richardson numbers

The Richardson number is a ratio of mechanical to density effects and indicates when mixing will take place. The Richardson number is defined as,

$$Ri = N^2 / \left(\frac{\partial u}{\partial z}\right)^2 \tag{2.3}$$

where the buoyancy frequency is $N = \sqrt{-(g/\rho)(\partial\rho/\partial z)}$. If $Ri > 0.25$, there is little mixing and flow is considered laminar. If $Ri < 0.25$, mixing is taking place and the flow is unstable. As the shear between 2 layers increases, the Richardson number decreases and Kelvin-Helmholtz waves form at the interface, which can become unstable and break generating mixing.

Chapter 3

The Columbia River plume

In this chapter, all relevant aspects of the Columbia River plume that are needed to fully understand the investigations that were undertaken are described in detail.

3.1 The Columbia River plume

With a drainage basin of approximately 668,000 km^2 and mean discharge of 7,300 m $^3s^{-1}$ the Columbia River is the largest source of fresh water to the Northwest Pacific (Garcia Berdeal et al., 2002). River discharge varies throughout the year with maximum flow between May and June, due to snow melt and minimum flow during late summer (Fiedler and Laurs, 1990). The Columbia river estuary is wide and shallow but restricted at the mouth by two jetties to just under 4 km width, with a depth of less than 20 m producing ebb tidal velocities exceeding 3 m s^{-1} (Hickey et al., 2010). Due to heavy damming along the length of the river there are less suspended sediments transported into the ocean than may be expected from a river of this size.

The region is dominated by wind-driven currents, the southward California Current in the summer and the northward Davidson Current in the winter. The onset of the California Current produces an upwelling of low oxygen, nutrient-rich water from the continental slope onto the shelf (Hickey et al., 2010). This upwelling of nutrients fuels the highly productive ecosystem through the spring bloom and into summer. The interaction of the Columbia River plume with these upwelled waters has been investigated by Banas et al. (2009) using a tested model (MacCready et al., 2009) to track Lagrangian particles released in the estuary. It was found that the presence of the plume significantly increased the cross shelf transport of surface waters and increased retention on the shelf of upwelled waters.

3. THE COLUMBIA RIVER PLUME

The shelf along the Pacific coast of North America is narrow, approximately 50 km and falls away steeply to a depth of over 2000 m, just 125 km from the coast. There is a deep canyon that cuts across the continental slope directly west of the Columbia River mouth. Cross-shelf canyons have been shown to increase upwelling and therefore increase nutrient flux onto the shelf (Allen and Hickey, 2010; Hickey and Banas, 2008). The Columbia River plume has been shown to have a higher chlorophyll concentration than the surrounding waters (Landry et al., 1989; Thomas and Weatherbee, 2006). This may be attributed to the formation of a recirculating bulge which forms at the mouth of the river and increases the residence time of the bulge waters to a few days (Horner-Devine, 2009; Horner-Devine et al., 2009).

The supercritical outflow of the Columbia River plume has been shown to produce non-linear internal waves in the stratified shelf waters (Nash and Moum, 2005). It was found by Pan and Jay (2009*a*) that 70% of the total frontal energy is carried by eight internal solitons and that they contribute to the exchange between ambient and plume waters. It was also found by Pan and Jay (2009*b*) that the presence of strong velocity shear increased the depth at which the solitons of maximum amplitude were found.

The creation of these solitons have been replicated in a modelling study by Stashchuk and Vlasenko (2009), which show that the internal waves detaching from the decelerating plume and propagating freely over the shelf. Soliton detachment was found to be sensitive to stratification with the best conditions for wave detachment being when buoyancy frequency decays dramatically with depth. These recent investigations lead the way to further analysis of the production of internal waves by the Columbia River plume.

There is no evidence of an investigation into the importance of non-hydrostaticity to the process of internal wave generation. Also, no literature has been found on the generation of higher mode internal waves, which could prove to further increase mixing of the plume. Both of these subjects will be addressed in this thesis.

The response of the river plumes to wind forcing is a much studied area and the effect of wind on the Columbia River plume has been deduced in the recent modelling studies (Garcia Berdeal et al., 2002; Burla et al., 2010). There has not, however, been an investigation of wind effects using a high resolution (both temporally and spatially), non-hydrostatic model. Therefore, it was an objective of this thesis to fully investigate the response of the Columbia River plume to wind forcing over a short period. The effect of upwelling favourable wind on plumes has also been recently investigated by Fong and Geyer (2001), who show that plumes respond in line with Ekman dynamics and that shear-induced mixing is important depending on the bulk Richardson number. This work has been furthered by Lentz (2004) and Hetland (2008, 2010) by accounting for entrainment to the plume. Using these findings an analysis of the Columbia River plume's response to wind driven mixing was undertaken in this thesis.

The fate of the Columbia River plume is largely determined by the tide, the wind and river discharge as well as the currents found in the area (Figure 3.1), all of which vary considerably in space and time. These driving forces fluctuate with time creating a very dynamic system. The plume volume depends on the discharge of the river, but its size and shape in three dimensional space are a result of its interactions with the dynamics and bathymetry of the surrounding environment.

The plume thickness varies with distance from the coast. At a distance of 20 km from the coast, the plume thickness is normally less than 10 m and generally closer to 5 m (Kilcher and Nash, 2010). In the vicinity of the river mouth, however, the plume may be as thick as 18 m and in the estuary river waters regularly extend to the bottom. Depending on the wind strength and direction, strength and phase of the tide and river discharge, the plume my spread for tens of kilometres away from the coast and hundreds of kilometres in the along-shore direction (Thomas and Weatherbee, 2006).

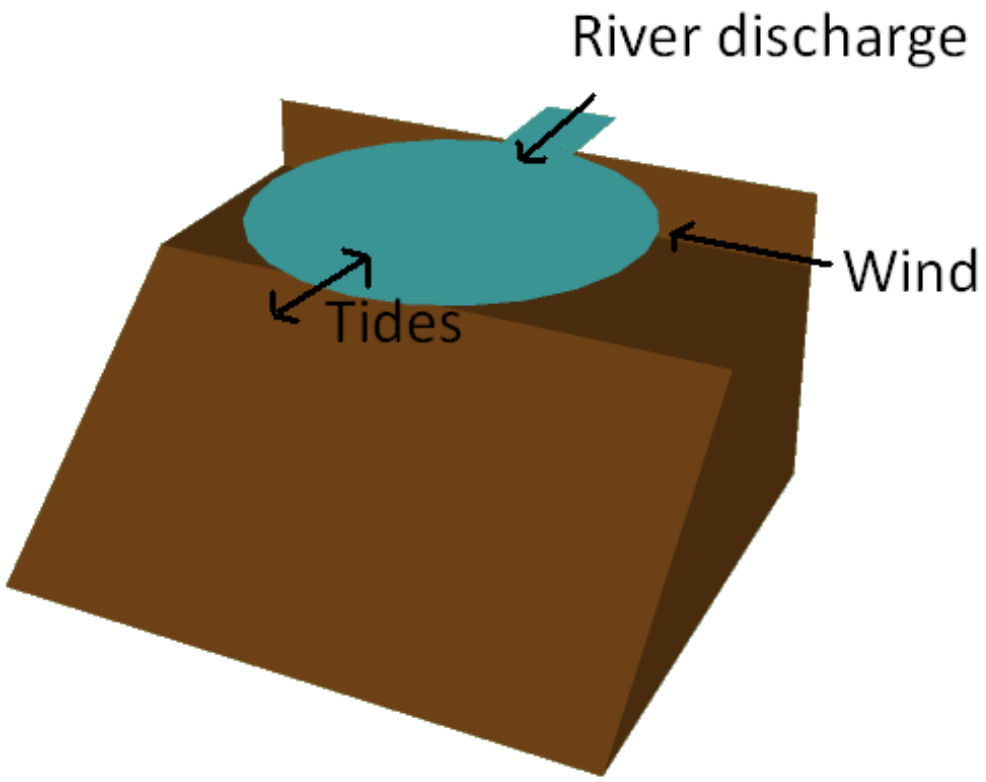

Figure 3.1: A schematic of the driving forces acting on a river plume

3.1.1 Bathymetry

The mouth of the Columbia river is approximately 3.8 km wide, constrained between constructed jetties. The bar across the river mouth is on average 18 m deep. The estuary widens and shallows inland to 7 km and this wide part of the estuary stretches for over 35 km. With the exception of two channels, which are navigable by large vessels, the estuary is relatively shallow, O(10)m, with a large drying area. The Kelvin number, the ratio of river mouth width to the internal deformation radius, is generally less than 0.5 so dynamically the estuary an be considered narrow (Hickey et al., 2010).

Beyond the mouth of the river the continental shelf stretches for 40 km before reaching the steep continental slope, which drops rapidly to a depth of over 2000 m

(Figure 3.2). The shelf to the north of the river mouth is wider and less steep than that to the south, potentially increasing the transport of upwelled nutrients in this area (Bruland et al., 2001). A large, deep canyon (Astoria Canyon) cuts though this slope adjacent to the river mouth, facilitating the transport of nutrient rich deep water up onto the shelf. The topography immediately outside the river mouth appears to turn the central jet of the plume to the south (Stashchuk and Vlasenko, 2009).

3.1.2 Discharge

The discharge of the Columbia River is modified by damming (14 main stem dams) and extraction of water along its entire length. Despite these anthropological interactions flow varies seasonally with a broad maximum flow over winter of ≈ 8000 m^3 s^{-1} due to high precipitation rates in the catchment area, followed by a spring peak of 10000 m^3 s^{-1} which coincides with the increase of meltwater reaching the river, and a late summer minimum of ≈ 3000 m^3 s^{-1} (Kilcher and Nash, 2010), when both precipitation and meltwater levels are low. This variability in mean daily discharge is shown in Figure 3.3, for the 10 years, 2000 to 2009, as measured at Beaver Army terminal. This variability in discharge results in a seasonal variation in plume volume with larger volume plumes coinciding with larger discharge, the volume ranges between 2 and 11×10^{10} m^3 (Hickey et al., 2005).

3.1.3 Tide

The discharge of the river is regulated by the tides of the region, which are mixed semi-diurnal with diurnal inequality (Hughes and Rattray, 1980), so whilst the area experiences two tides per day, the amplitude of consecutive tides can vary considerably. The output of the TPXO7.2 barotropic tidal model described by Egbert and Erofeeva (2002), for the tidal elevation at the Columbia River mouth for August 2005 is shown in Figure 3.4 and the tidal constituents in Table 3.1. The mean tidal range at the mouth

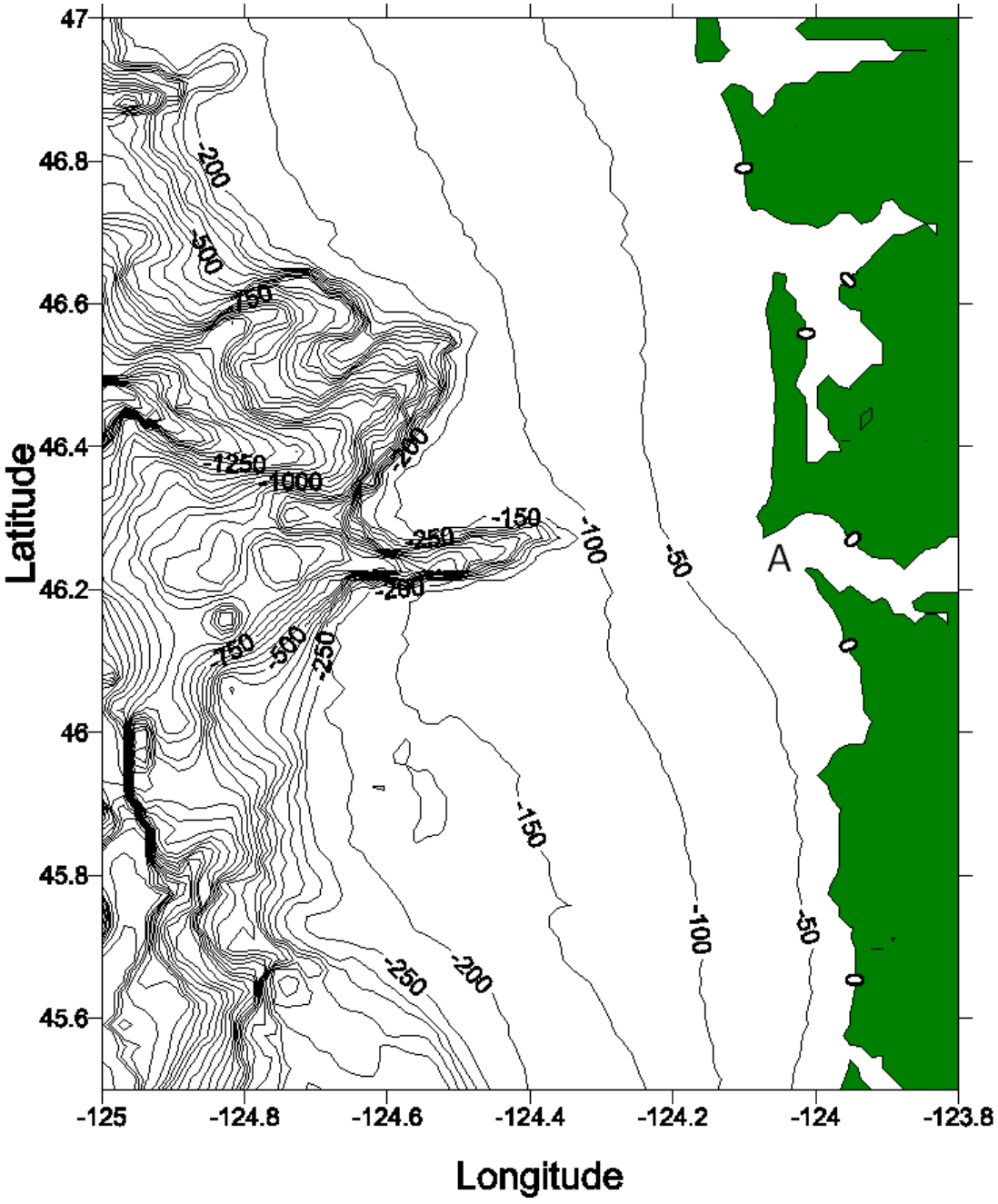

Figure 3.2: Bathymetry of the shelf and slope adjacent to the Columbia River mouth, A

(North Jetty) is 1.68 m (National Oceanic and Atmospheric Administration, 2011) and moderate spring tides can produce a range of $\approx$ 2.5 m (Orton and Jay, 2005).

Figure 3.3: Mean daily discharge of the Columbia River at Beaver Army Terminal for the 10 year period 2000-2009

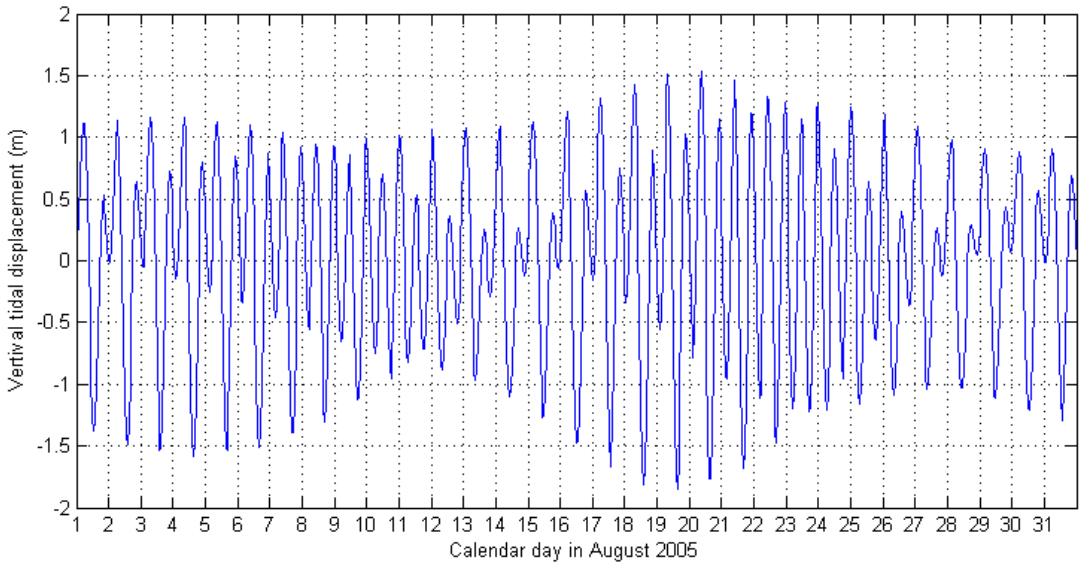

Figure 3.4: Tidal displacement for August 2005 at the mouth of the Columbia River (lat=46.235 long=236.0167) as given by the TPXO7.2 tidal model

This tidal regime produces estuarine outflow velocities as high as 3 m s^{-1}, reversing with the tides generating a pulsed discharge (Horner-Devine et al., 2009). During the flood tide, shelf water penetrates the estuary and outflow is minimal until the ebb tide, when a fast flowing jet of estuary water exits the mouth. This can be seen in observations presented by Nash et al. (2009) of salinity and velocity measurements taken within the estuary (Figure3.5). The maximum salinity intrusion is 50 km (Simenstad et al., 1992), although the tidal influence is present 135 km from the river mouth. This produces a pulsating plume with a semi-diurnal phase which varies in size with the spring/neap tidal cycle. Within the estuary, the tides influence the transport of sediments with accumulations occurring during neap tides and remobilization during spring tides. This process determines the location of the turbidity maximum within the estuary, which, during spring tides, can be advected by up to 20 km (Geyer, 1993).

Figure has been removed due to copyright restrictions

Figure 3.5: (a) Salinity, (b) along-channel velocity, during 17-18th August 2005. Data are plotted with respect to height above bottom, and profile to profile changes in the vertical extent of data thus reflect changes in the bottom depth (due to ship location). The trend represents the 3-m surface tide η_0 (shown above Figure a). The bottom boundary layer height h_{bbl} is shown in Figures a (black line), times are in UTC. *from* Nash et al. (2009)

3.1.4 Stratification

The stratification of the estuarine and shelf waters plays an important role in several plume processes. The five year interdisciplinary RISE (River Influences on Shelf Ecosystems) study gathered salinity and temperature profiles from the Columbia River Plume region with CTD's. Some of the the collected profiles are shown in Figure 3.6.

Table 3.1: Tidal constituents generated by TPXO7.2 with amplitudes and phases at the Columbia River mouth

Tidal constituent	Amplitude (m)	Phase (h)
M2	0.8927	7.637
S2	0.2531	8.538
N2	0.1888	6.792
K2	0.0686	8.249
K1	0.4226	7.874
O1	0.2599	7.406
P1	0.1322	7.804
Q1	0.0447	7.187
MF	0.0139	5.533
MM	0.0064	5.453

The stratification of the shelf waters is important for internal wave generation, separation and evolution as shown in Stashchuk and Vlasenko (2009)with well mixed waters being shown to stop the emergence of internal waves.

The estuary is often highly stratified except during periods of low river discharge and strong tides, which result in weak stratification or partial mixing. Strong tidal currents often result in a salt wedge formation and Hughes and Rattray (1980) found that tidal pumping accounted for over half of the up estuary salt flux. The remnants of the plume in the shelf waters increase localised stratification until they become thoroughly mixed with the shelf waters by the wind. During the low wind conditions of summer, this increased stratification can cap the upwelling (Hickey et al., 2005), so reducing the transport of nutrients to the surface resulting in a reduction of productivity.

3.1.5 Wind

The strength and direction of the wind has been shown to cause river plumes to vary by inducing currents in the shelf waters and by direct forcing of the plume (Fong et al., 1997; Kourafalou, 1999; Garcia Berdeal et al., 2002). The region has seasonal

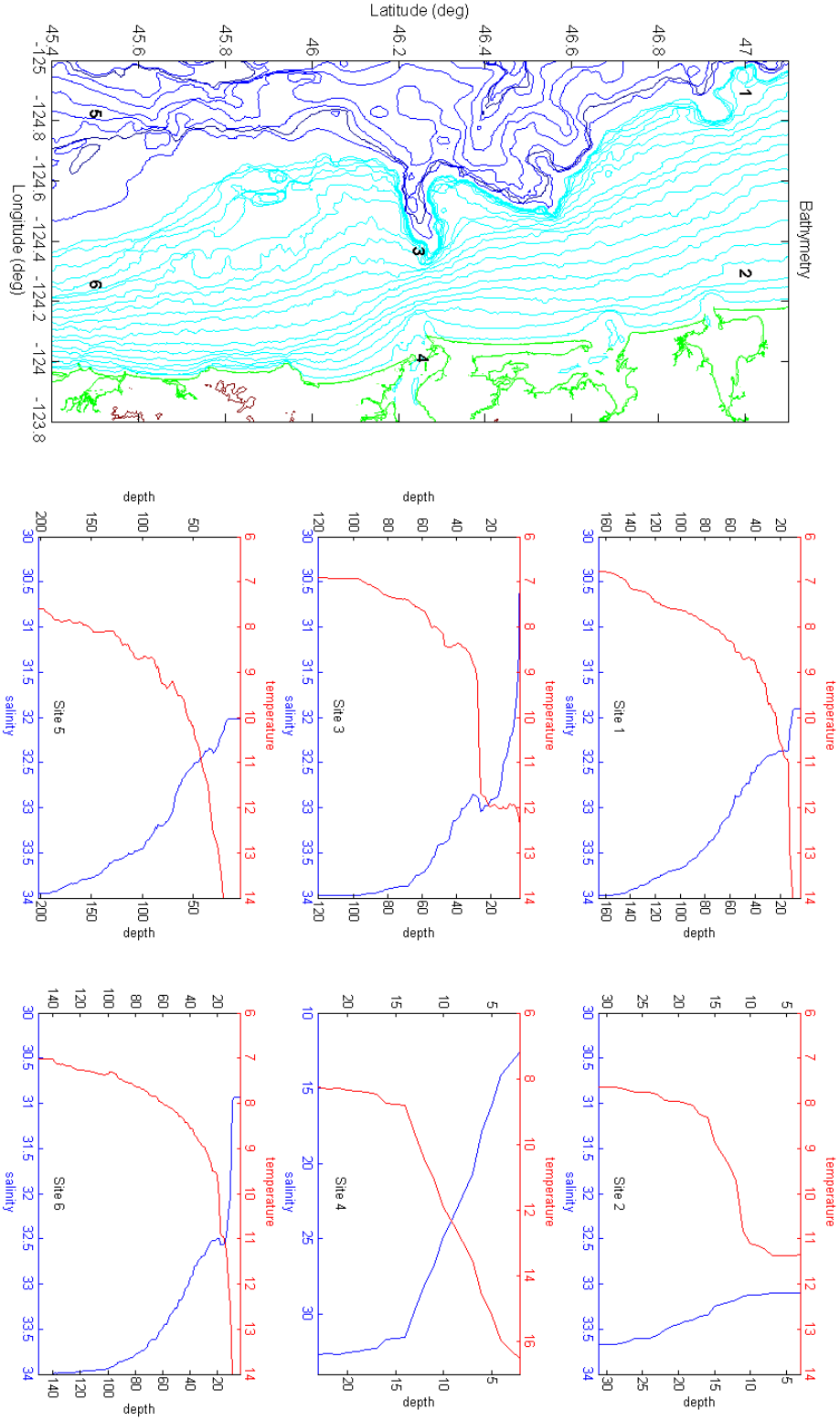

Figure 3.6: Salinity and temperature profiles taken during the RISE cruise August 2005. Profile sites relate to number locations on bathymetry. Bathymetry plot shows 10 m cyan contour to 200 m and 200 m contours in blue

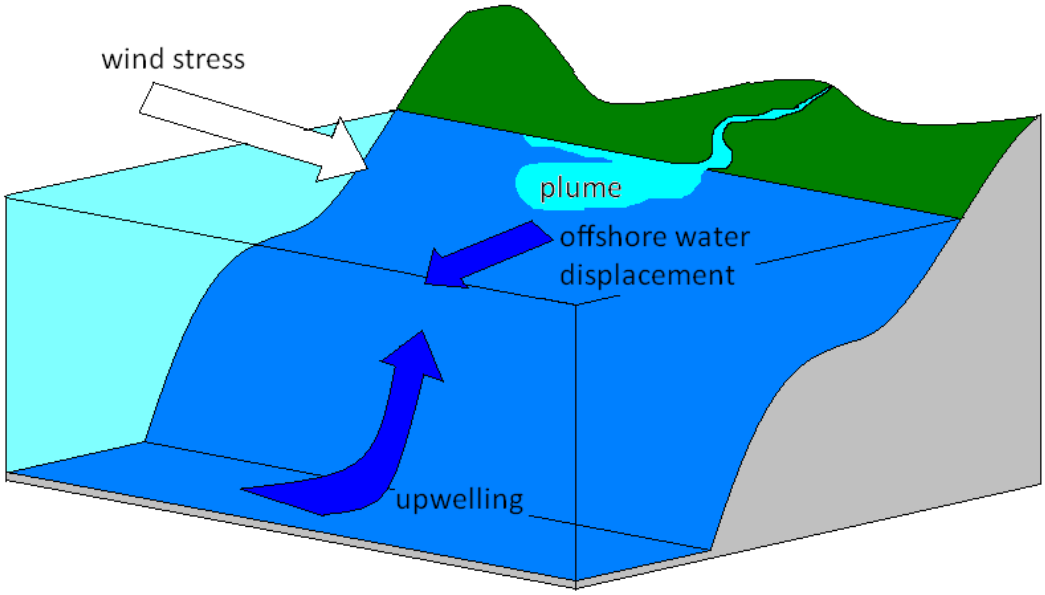

Figure 3.7: Schematic of the effect of upwelling wind. Winds from the north produce an offshore current which induces upwelling of deep water

weather patterns with predominant northerly winds during the summer and southerly winds during winter. Due to Ekman transport, northerly winds push the plume and surrounding water offshore in a south-westerly direction and induce the upwelling of water from the slope, Figure 3.7. Conversely, southerly winds produce an onshore transport of water, trapping the buoyant plume to the Washington coast and producing downwelling conditions. Frequently, the plume also becomes bi-directional when wind direction switches between downwelling and upwelling states (Hickey et al., 2005). There are regular wind reversals produced by passing weather systems, however, it is not uncommon for southerly summer winds to persist for 2 to 3 weeks. Wind speeds rarely exceed 10 m s^{-1} during summer months.

3.1.6 Internal waves

As observed by Nash and Moum (2005) during the ebb phase of the tide, the Columbia River plume generates internal waves that are released and propagate freely when the

plume becomes sub-critical (Froude number <1). Figure 3.9, taken from Nash and Moum (2005), shows measurements of density, acoustic back scatter and velocity taken across the plume front. The stages of frontal growth (panel a) and wave fission (panels b and c) have been captured over a period of 1 hour 20 minutes. The horizontal velocity convergence produced at the plume edge converts some of the plume's kinetic energy into potential energy creating vertical displacements of $\approx$ 25 m. As the plume decelerates and u_f drops to 0.4 m s^{-1}, wave fission occurs and a freely propagating soliton is released from the plume travelling at a speed of 0.4 m s^{-1} to 0.45 m s^{-1} with an amplitude of 20 m (panel b). After a further 2 hours 30 minutes, a train of 6 freely propagating waves can be seen (panel d).

The released waves can clearly be seen in Figure 3.8, a synthetic aperture radar (SAR) image in which the signature of internal waves can be seen radiating from the river mouth. Internal waves leave a surface roughness signature visible to SAR as described by Alpers (1985). The leading and trailing edges of the waves are associated with convergence and divergence zones, which are seen as light and dark bands on SAR images, due to the respective increase and decrease in Bragg wave amplitude (Figure 3.10). Findings of Alpers (1985), show that the horizontal gradient $\delta u/\delta x$ is proportional to the deviation in backscattering detected by SAR. By calculating the horizontal velocity gradient in the model surface layer, it is possible to visualise the position of internal waves.

3.1.7 Biogeochemistry

The Columbia River is an important source of both macro- and micro-nutrients to the region and therefore influences the local biological productivity (Kudela and Peterson, 2009; Aguilar-Islas and Bruland, 2006; Lohan and Bruland, 2006). However, unlike many large estuarine systems, such as the Mississippi, it does not supply a large quantity of nitrate or iron to the plume region (Turner and Rabalais, 1994; Lohan and Bruland,

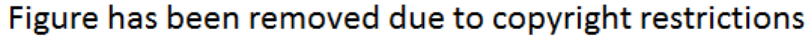

Figure 3.8: Synthetic Aperture Radar (SAR) image of the Columbia River Plume on August 9, 2002. Image indicates regions of enhanced surface roughness associated with plume-front and internal wave velocity convergences. Image processed at the Alaska Satellite Facility, copyright Canadian Space Agency (2002) *from* Nash and Moum (2005)

2006). In summer, it supplies very high levels of silicic acid which is important for the growth of marine diatoms. Nitrate concentrations are highest in May and June and lowest in July and August (Bruland et al., 2008), but the major source of nitrate in the region is from upwelled waters. The plume's role in mixing these upwelled waters is suggested to be more important than the plume's own nitrate content in influencing the nitrogen load of the surrounding coastal waters (Lohan and Bruland, 2006). Within the estuary, summer nitrate and silicic acid concentrations both behave conservatively, as biological activity is low and residence times are of a few days. Bruland et al. (2008) found that the relatively low concentration of nitrate in the summer plume is the limiting factor for phytoplankton growth. The plume also transports sediments predominantly to the north, which may allow adsorbed nutrients to become available to organisms in the euphotic zone during periods of upwelling (Hickey et al., 2010).

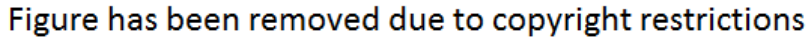

Figure 3.9: Three stages of a wave-generation event. (1) frontal growth at the plumes leading edge (panel a), (2) wave fission from the plume front (panels b, c), and (3) free propagation of a train of large-amplitude internal waves (panel d). Shown are density (left), acoustic backscatter (middle) and cross-front component of horizontal velocity (right) in a rotated reference frame aligned and moving with the front. Positive distances and velocities are approximately northward. Panels are shifted to align the plume front (as determined from sea surface salinity); vertical black lines represent the plume front (zero cross-front distance). Only cross-front velocity is shown for the freely propagating waves in d. Particle streamlines and velocity vectors (u,w) in a reference frame moving with the front (translating at speed ufas indicated) are contoured over the density plots. Also shown for pass 4 (panel a) are vertical profiles of density ahead of (red, ambient) and behind (blue, plume) the front. A schematic cartoon illustrating frontal growth in a reference frame moving with the plume front (at speed uf) is shown in upper left inset. Velocities of the near-surface fluid behind the plume front (up) and ambient water ahead of it (ua) are indicated.*from* Nash and Moum (2005)

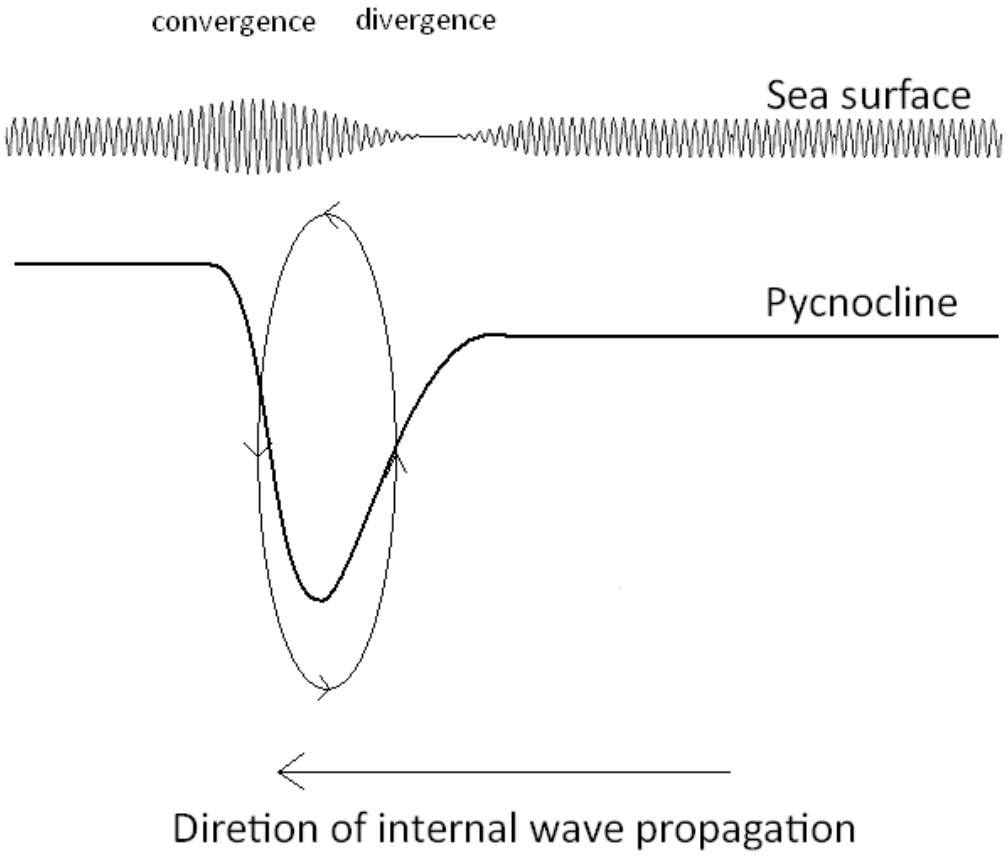

Figure 3.10: Schematic plot of streamlines associated with a linear internal wave propagating along a sharp pycnocline. The short-scale roughness is modulated by the surface current associated with the internal waves

Chapter 4

Methodology

This chapter systematically presents the set of equations and assumptions on which the Massachusetts Institute of Technology general circulation model (MITgcm) is based. The model set-up is described, including the forcing and boundary conditions used.

4.1 Equations

The plume is a stratified structure propagating in a sea of variable depth, which rotates with the Earth. Its motion is considered in a right-handed rectangular Cartesian system of coordinates, $0xyz$, with $0xy$ an undisturbed sea surface and the $0z$-axis directed vertically upwards, Figure 4.1. The equations of motion that govern an idealized oceanic flow on a rotating sphere are; the momentum equation,

$$\rho\frac{D\vec{u}}{Dt} + \rho 2\vec{\Omega} \times \vec{u} = -\nabla p + \rho\vec{g} + \mu\nabla^2\vec{u} \tag{4.1}$$

where, ρ=$\rho(x,y,z,t)$ is the density field, $\frac{D}{Dt} = \frac{\partial}{\partial t} + \vec{u}\cdot\vec{\nabla}$ is the material derivative, $\vec{u}(x,y,z,t)$=(u,v,w) is the velocity field, $\vec{\Omega}$=$(0,\Omega\cos\phi,\Omega\sin\phi)$ where Ω is the angular velocity of the Earth $\frac{2\pi}{24\times60\times60} \approx 10^-4\,rad\,s^-1$ and ϕ is latitude. The rate of change of velocity of a fluid particle is represented in the first term on the left hand side and the Coriolis force by the second term. On the right hand side $\nabla = \frac{\partial}{\partial x} + \frac{\partial}{\partial y} + \frac{\partial}{\partial z}$ is the vector gradient operator, p=$p(x,y,z,t)$ is the pressure field. Together, they give the vector field created by the gradient operator acting on the scalar pressure field, called the pressure gradient. $\vec{g} = (0, 0, -g)$ is the constant of gravitational acceleration and μ is the turbulent dynamic viscosity coefficient in the viscosity term that dissipates small-scale motions and ∇^2 is the Laplacian operator and equal to $\nabla\cdot\nabla$.

The continuity equation is,

$$\frac{1}{\rho}\frac{D\rho}{Dt} + \vec{\nabla} \cdot \vec{u} = 0 \tag{4.2}$$

which states the conservation of volume relative to mass. The energy equation is,

$$\frac{DT}{Dt} = \kappa_T \nabla^2 T \tag{4.3}$$

which states that heat is conserved and where $T{=}T(x,y,z,t)$ is the temperature field and κ_T is the spatially constant thermal diffusivity. Similarly, the salt equation that states salt is conserved is

$$\frac{DS}{Dt} = \kappa_S \nabla^2 S \tag{4.4}$$

where κ_S is the coefficient of salt diffusion and again spatially constant. Finally, the equation of state is,

$$\rho = \rho(T, S, p) \tag{4.5}$$

which shows that density is dependent on temperature, salinity and pressure.

4.2 Approximations

In order to study a small-scale phenomenon (small compared to the global oceans), such as river plumes, some assumptions can be made that simplify the equations of motion, improving computational efficiency whilst still producing an acceptable solution.

4.2.1 Incompressible fluid

For the ocean, it is common to make the assumption that flow is incompressible as even at the deepest parts of the ocean pressure has little effect on the volume of a water parcel. So by assuming that $\frac{1}{\rho}\frac{D\rho}{Dt} = 0$ density can be removed from Equation 4.2 and the continuity equation becomes

$$\vec{\nabla} \cdot \vec{u} = 0 \tag{4.6}$$

$$\tag{4.7}$$

4.2.2 f-plane approximation

The model uses the f-plane approximation, where the Coriolis parameter f is constant rather than varying with latitude as shown below,

$$f = 2\Omega sin\phi \tag{4.8}$$

where Ω is the Earth's rate of rotation and ϕ is latitude.

This approximation can be made as the area of investigation is small compared to the Earth's surface and at most spans less than two degrees of latitude ($\approx$ 45 to 47). In this way we can ignore the curvature of the earth and consider the model domain as a plane as in Figure 4.1.

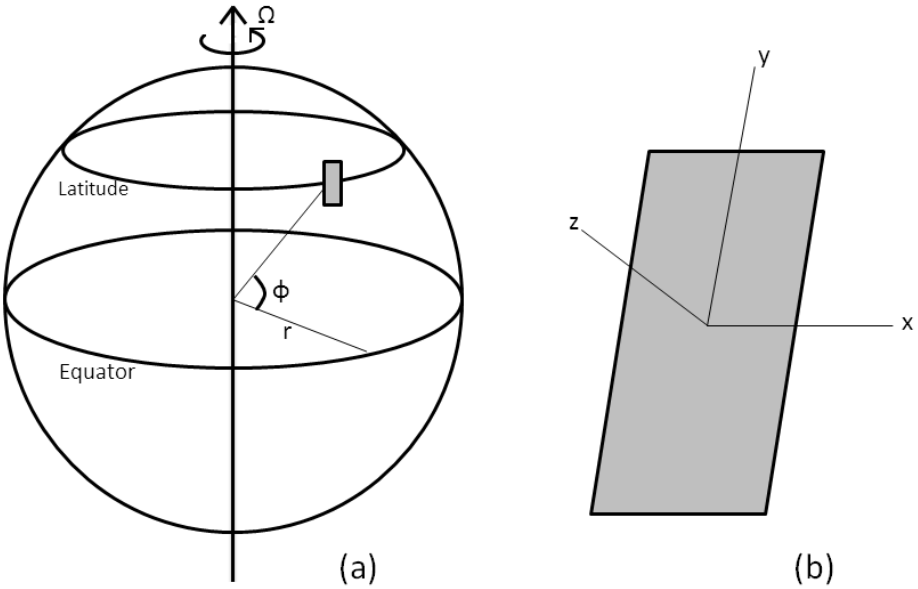

Figure 4.1: The coordinate system of the Earth (a) and the model (b)

4.2.3 Equation of state

In order to solve the momentum equations, the model must first calculate local density values. The equation of state (EOS) for sea water, equation 4.5 ρ=ρ(T,S,p) shows that

density ρ is dependent on temperature, T, salinity, S and pressure, p. The model has the option for both linear and non-linear EOS. For this investigation the linear EOS was used and is given below

$$\rho = \rho_0(S_\beta(S_{loc} - S_{ref}(k_{ref})) - T_\alpha(T_{loc} - T_{ref}(k_{ref})) + \partial\rho \tag{4.9}$$

where the coefficients S_β and T_α were set as 7.4×10^{-4} and 2×10^{-4} respectively. S_{ref} and T_{ref} are reference temperatures and salinities.

Here, density is only dependent on salinity and temperature but not on pressure. This is justifiable, as here we are primarily interested in surface phenomena where pressure does not significantly vary.

4.2.4 Hydrostatic approximation

Using the full Navier-Stokes equations in a numerical model is computationally expensive so it is common to simplify them to a hydrostatic form when vertical accelerations are small compared to the gravitational acceleration. The scale at which the hydrostatic approximation can be made is given by the non-hydrostatic parameter n (Marshall, Hill, Perelman and Adcroft, 1997),

$$n = \frac{\gamma^2}{R_i} << 1 \tag{4.10}$$

where γ=h/L, with h being the vertical length-scale of the flow and L the horizontal length-scale, and R_i, the Richardson number = N^2h^2/U^2. This means the non-hydrostatic effects are important for models which have small horizontal length scales (<1-10 km). If hydrostaticity is assumed at these scales, potentially important details of vertical structure and mixing may be lost.

When hydrostaticity is assumed only pressure and gravitational effects in the vertical are retained and the vertical momentum equation becomes,

$$\frac{\partial p}{\partial z} = -\rho g. \tag{4.11}$$

Despite the large areas covered by the Columbia River plume and thin nature of the feature, it is desirable to model the dynamics at a small scale, because there are fine-scale features that affect the distribution of the river water, such as the head of the flow. Due to the scaling mentioned above, a non-hydrostatic method was chosen for this investigation. There has been little use of non-hydrostatic models to investigate river plumes but, this study looked at several scales of plume evolution.

4.3 Ocean models

Today, there are many well developed numerical models used to model the dynamics of the oceans. Here the range of different features utilised within the most widely used models is presented.

The main community models currently can be categorized as one of the following types, depending on how they spatially discretise the primitive equations; finite difference, finite element and finite volume. Finite difference models are the earliest form of primitive equation models and impose a regular horizontal grid over a model domain and a Taylor series expansion is solved for each grid point, which can prove problematic when dealing with irregular coastlines. Similarly, finite volume models often use a regular grid but have the benefit that mass, momentum and energy are all conserved within the domain as the governing equations are integrated over the volume of a grid cell. Finite element models use unstructured grids that allow for a wide range in resolution and are often used in coastal engineering scenarios. Whilst they can yield good results, it is difficult to give physical significance to their algebraic terms.

Within these types different vertical coordinate systems are available. These are geopotential, isopycnic, sigma and hybrid coordinates. Geopotential or z coordinates are parallel to the sea surface. Isopynic coordinates follow isopycnals so layer thickness varies between water masses. Sigma coordinates are terrain following so layer thickness is thinner in shallow regions and are beneficial where steep topography is encountered

by flows. Hybrid coordinate systems exist that allow the beneficial features of more than one type of coordinate system to be used.

For the study of buoyant surface flows a z coordinate system is beneficial as the layer height at the surface can be controlled and maintained across a model domain, giving maximum resolution in the region of interest. Since there is little interaction of surface flows with topography, sigma coordinates are not required.

4.4 Method of solution: MITgcm

The model used in this investigation is MITgcm (the documentation for which can be found at www.mitgcm.org). This model was chosen because it is 3 dimensional and can be used in non-hydrostatic as well as hydrostatic mode. It also has the ability to add passive tracers, which can be used to track fluid movements, simulate nutrient dispersal and has been used in a number of successful studies at a range of scales. A detailed description of the model's numerical scheme and governing equations is provided in Marshall, Hill, Perelman and Adcroft (1997) and Marshall, Adcroft, Hill, Perelman and Heisey (1997).

MITgcm uses finite volume techniques and an Arakawa C grid configuration. The finite volume method employed allows grid cells to be shaved in order to conform more closely to non-uniform topography (Adcroft et al., 1997). For the purposes of this study a z coordinate system was used in the vertical in order to maintain high resolution in the surface layer. Time-stepping uses a second-order Adams-Bashforth scheme which reduces current divergence.

The non-hydrostatic momentum equations discretised in time are

$$\frac{1}{\Delta t}u^{n+1} + g\partial_x\eta^{n+1} + \partial_x\phi_{nh}^{n+1} = \frac{1}{\Delta t}u^n + G_u^{(n+1/2)} \tag{4.12}$$

$$\frac{1}{\Delta t}v^{n+1} + g\partial_y\eta^{n+1} + \partial_y\phi_{nh}^{n+1} = \frac{1}{\Delta t}v^n + G_v^{(n+1/2)} \tag{4.13}$$

$$\frac{1}{\Delta t}w^{n+1} + \partial_r\phi_{nh}^{n+1} = \frac{1}{\Delta t}w^n + G_w^{(n+1/2)} \tag{4.14}$$

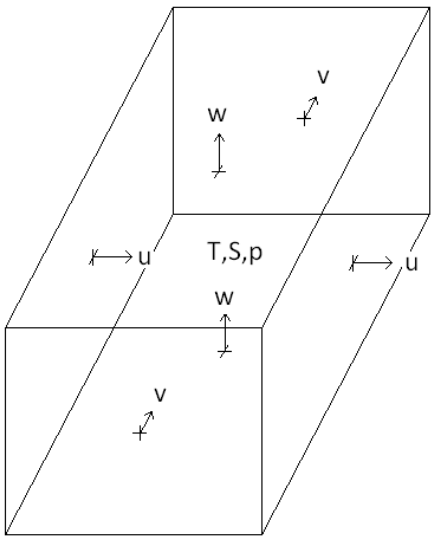

Figure 4.2: *T,S*and p are zone quantities whilst u,v and w are face quantities

where the vector G contains all terms in the momentum equation. η is the deviation of the horizontal pressure surface from its mean and ϕ is the non-hydrostatic (nh) pressure field. Spatially, the domain is divided into cells. Velocities are solved normal to the face of these cells whilst temperature, salinity and pressure are solved for the volume of the cell as shown in Figure 4.2

4.5 Parallel computing and data processing

The computational time required to carry out complex simulations, over large areas and at high resolution, is great and even on today's fastest processors, the time taken would be impractical. A solution to this problem is to use many processors working in parallel to distribute the computation. For parallelisation the model domain is broken down into tiles with each tile being assigned to a processor Figure 4.3. The tile size must allow for an overlap between tiles of 3 grid points. Between each time-step, information of the

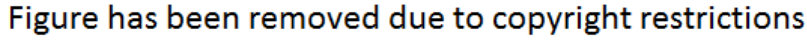

Figure 4.3: Diagram of a domain divided into tiles and distributed to individual processors *from* MITgcm User Manual Adcroft et al. (2011)

variables within these overlapping areas are communicated between tiles, Figure 4.4. A Poisson equation for the pressure field must be solved across the whole grid in order to prevent divergence and is a time consuming process. Since the generation of the pressure field is the most costly task, each tile is assigned to a processor containing the full ocean depth at that location so minimising communication times between processors (Marshall, Adcroft, Hill, Perelman and Heisey, 1997). The simulations were run on a multi-processor cluster utilising 64 to 128 cores with an openMPI scheme. Above 128 cores, even for the largest grid, there were no significant speed improvements and in some cases run times were increased due the additional time taken to communicate information between overlapping tiles. Grid resolutions were varied, but for the larger domain a typical horizontal resolution 500 m with fine scale runs having a horizontal resolution as fine as 12.5 m (although with a much smaller domain) . Vertical resolution was 1 m at the surface, but below the depth of the plume, cell thickness was increased towards the bottom.

Matlab was used to analyse and visualise the model output, which is generated in the form of 3 dimensional matrices of temperature, salinity, u, v and w velocities and any tracers used in the run.

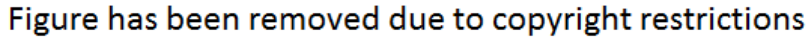

Figure 4.4: The figure shows four tiles. The curved arrows indicate exchange primitives which transfer data between the overlap regions at tile edges and interior regions for nearest-neighbour tiles. The straight arrows symbolize global sum operations which connect all tiles. *from* MITgcm User Manual Adcroft et al. (2011)

4.6 Advection schemes

In order to investigate the movement and interactions water bodies and dissolved nutrients, it is useful to use a system of passive tracer tracking. This involves introducing a representative concentration of tracer into a cell or cells and allowing it to move with the water between cells. Tracers can also be used as Lagrangian drifters by setting physical diffusion to 0 and tracking the location of the concentration maximum. Since these tracers are passive and have no effect on density, a method for their advection must be prescribed. MITgcm allows the user to choose from several advection schemes, linear and non-linear, listed in Table 4.1. Each of the schemes present have different benefits and have varying limitations. The default advection scheme is the linear centred 2^{nd} order scheme however it has been found that this scheme is not suitable for the experiments presented here. For the tracer experiments used in these investigations the 2^{nd} order Flux Limited scheme was used. This scheme is non-linear, multidimensional and utilises forward in time time-stepping rather than Adams-Bashforth time stepping and is suitable for use in models containing propagating fronts. Figures 4.5 and 4.6 show the differences between the default and the selected advection schemes. The tracer originated at grid-point x=700 y=600 and had an initial value of -100. Physical diffusion has been set to 0, so the spread of tracer is due to numerical diffusion, which

Table 4.1: Advection schemes available in MITgcm

Advection scheme	Properties
centred 2^{nd} order	linear
3^{rd} order upwind	linear/τ
centred 4^{th} order	linear
3^{rd} order Direct-Space-Time	linear/τ, non-linear/v
2^{nd} order Flux Limiters	non-linear
3^{rd} order Direct-Space-Time Flux Limiter	non-linear

occurs due to the discretisation in space and time of the governing equations. The high level of diffusion seen in Figure 4.5 and spurious positive values are a direct result of the default advection scheme for tracers for this grid set up.

4.7 Model set-up

4.7.1 Model domain and initial conditions

For near-field experimental runs the complicated shore line was simplified to be a straight shoreline with both realistic topography from hydro-graphic data as well as some simple sloping topographies being used. The ocean region of the model was filled with a uniformly stratified water with salinity S_o and temperature T_o, resulting in the density profile shown in Figure 4.7. The estuary was idealised into an area of approximately equal volume to the real estuary (Figure 4.8) and filled with less dense water in line with observed values of estuarine temperature, T_e, and salinity, S_e (the estuary water was not stratified). The density difference between the adjacent water masses results in a lock exchange like process when the model begins with the fresher water flowing out of the estuary during the ebb tide. On the flood tide saline water is pumped into the estuary. The velocity fields within the domain are all initialized as 0 so all flows are generated from either the boundaries or are buoyancy driven.

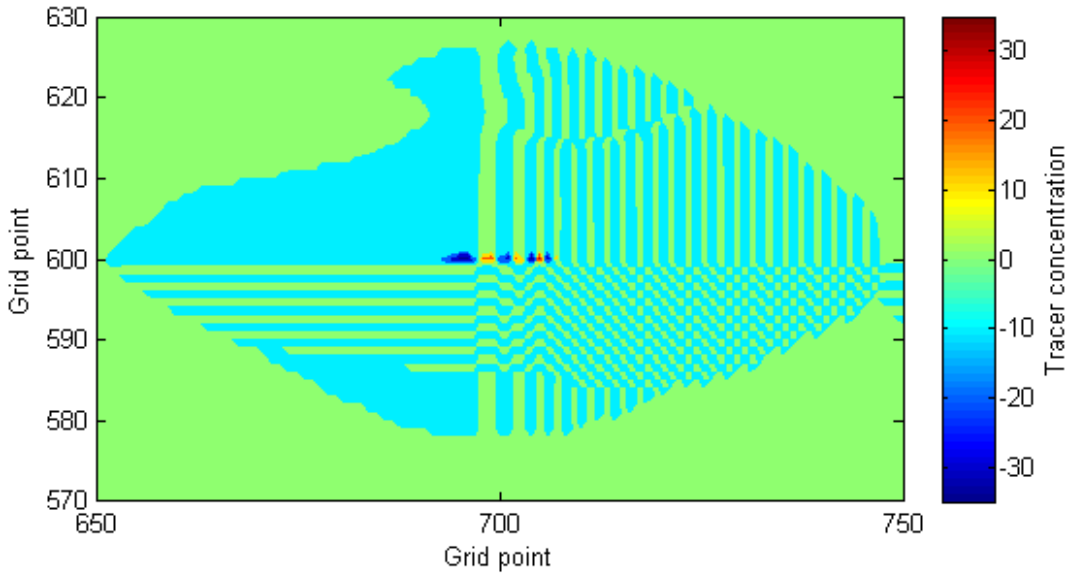

Figure 4.5: Advection of a tracer initially at a point after 1 hour using the default linear centred 2^{nd} order advection scheme

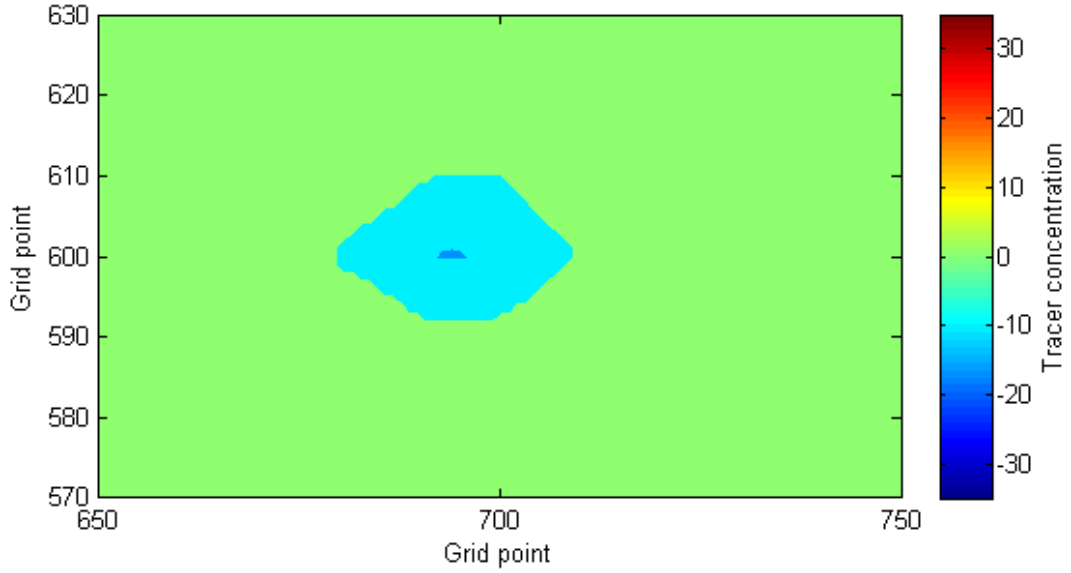

Figure 4.6: Advection of a tracer after 1 hour using the non-linear 2^{nd} order Flux Limited scheme

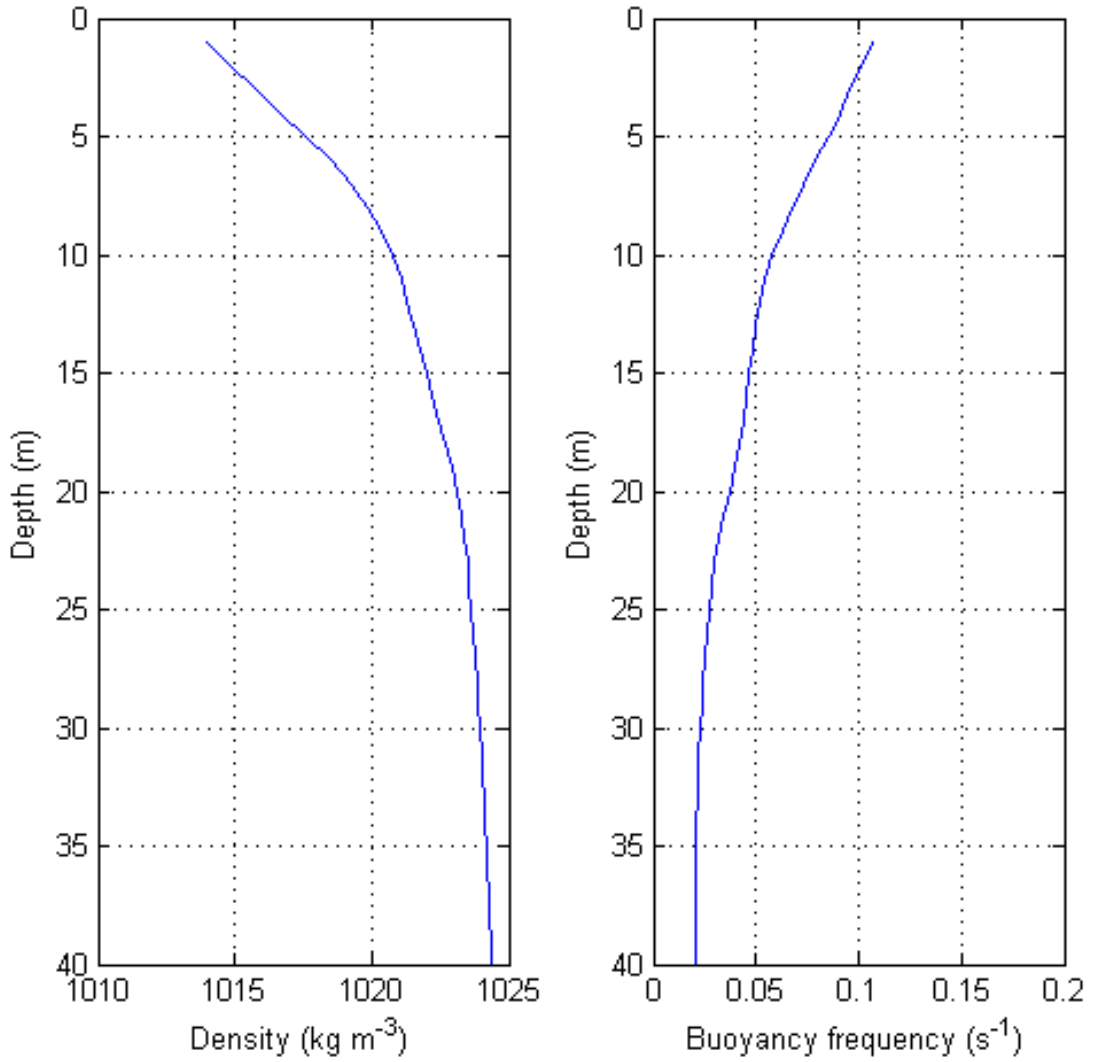

Figure 4.7: Smoothed density and buoyancy profiles used for the model shelf waters

4.7.2 Forcing

The plume propagation depends on the following forcing: river discharge, tide, density gradient between ocean and river, and wind.

River discharge measurements (Figure 3.3) and estuarine dimensions were used to calculate a representative flow that could be imposed at the eastern boundary. This was added to a representative tidal flow for the area calculated from measurements (Figure

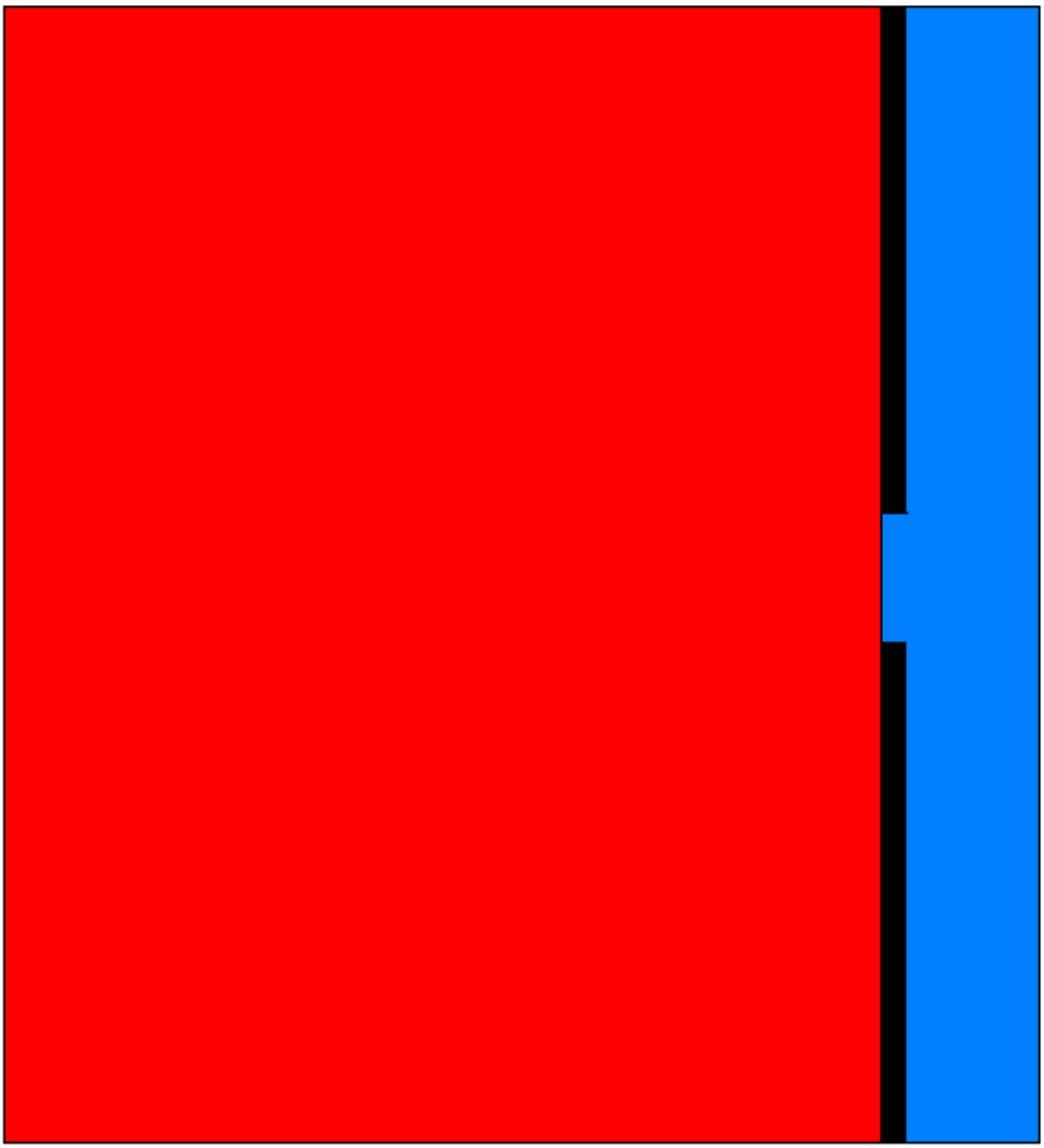

Figure 4.8: Schematic of near field model domain. Red area represents the ocean, blue area is the idealised estuary.

3.4). The density gradient was initialized as described in the previous section and was the same for all experiments. Wind stress can also be applied to the surface layer. For experiments representing realistic wind forcing, hourly measurements of wind speed near the mouth of the Columbia River were used to calculate the zonal and meridional

stresses, which were then used over the whole model domain. This is further described in section 6.3.1.

In this study, "near field" experiments with a small horizontal grid step and simplified forcing as well as "far field" experiments with a larger grid and realistic forcing will be considered.

4.7.3 Boundary conditions

The open boundaries used in the model are given a Sommerfield radiation condition as described by Orlanski (1976) to allow waves to propagate out of the domain rather than reflecting from the boundary and affecting the dynamics of the interior. The technique calculates the propagation speed, C, of each variable, ϕ from adjacent grid points:

$$C_\phi = \frac{-\phi_{j-1}^{\tau} - \phi_{j-1}^{\tau-2}}{\phi_{j-1}^{\tau} + \phi_{j-1}^{\tau-2} - \phi_{j-2}^{\tau-1} \times 2} \frac{\Delta x}{\Delta t} \tag{4.15}$$

where j is the boundary grid point and τ is the present time step. This is then used to calculate ϕ through the relation:

$$\phi_j^{\tau+1} = \frac{1 - \frac{\Delta t}{\Delta x} C_\phi}{1 + \frac{\Delta t}{\Delta x} C_\phi} \phi_j^{\tau-1} + \frac{\frac{2\Delta t C_\phi}{\Delta x}}{1 + \frac{\Delta t C_\phi}{\Delta x}} \phi_{j-1}^{\tau} \tag{4.16}$$

The limitation to this method is that only one wave velocity can be specified for each variable, in this case for the barotropic wave. Since this model also generates several modes of baroclinic waves, which cannot be released by the boundary, another solution to their reflection must be employed. By increasing the horizontal grid length towards the boundary, it is possible to increase the domain to a size which does not allow the baroclinic waves to reach the boundary.

4.7.4 Turbulence closure

It is impractical to resolve small-scale turbulent processes over a large model domain as the small-grid resolution required would become computationally uneconomical. There-

fore, an approximation of small-scale properties, such as eddy viscosity and diffusivity, must be made. Since these properties can vary significantly throughout the ocean, being larger in the surface mixed layer than below the thermocline, simply assigning them constant values is undesirable.

For a more realistic representation, a sub grid-scale turbulence closure scheme is required. MITgcm has several vertical mixing scheme options, these include schemes described by Pacanowski and Philander (1981)(PP81), Mellor and Yamada (1982)(MY82), Gaspar et al. (1990)(GGL90) as well as Large et al. (1994)(KPP).

The PP81 scheme is a first order, Richardson number dependent scheme which provides non-constant parametrisations of v, vertical eddy viscosity 4.17 and k eddy diffusivity 4.18,

$$v = \frac{v_0}{(1 + \alpha Ri)^n} + v_b, \tag{4.17}$$

$$k = \frac{v_0}{(1 + \alpha Ri)^n} + k_b \tag{4.18}$$

where v_b and k_b are background dissipation parameters and v_0, α and n are variable parameters. This scheme allows mixing to increase in areas where the Richardson number falls below 0.25, therefore increasing the total mixing taking place within the model compared to a fixed mixing scheme and so was used in these investigations.

MY82 is a second order Richardson based scheme that dissipates energy locally by enhancing viscosity above a background value (Klymak and Legg, 2010), whereas GGL90 is a simple eddy kinetic energy parametrisation. KPP combines several different processes into one scheme that describes mixing in the surface boundary layer and interior.

Chapter 5

Vertical structure and water mixing produced by a moving plume near a river mouth

In this chapter the model set up, theory and results of the investigation into the near-field plume are discussed. The focus is on the internal waves produced, the mixing processes and detailed circulation of the Columbia River plume.

5.1 Model set-up

The model domain represents an area 27.5 km in the north-south direction and 23.7 km in the west-east direction and used realistic bottom topography as presented in Figure 5.1 b. It contains 950×1100 grid points with horizontal step Δx=Δy=25 m (some sensitivity runs were conducted with Δx=Δy=12.5 m). An additional 50 grid points were added in the north, south and west directions with the grid-step increasing up to 4000 m. Such a method of grid telescoping helps to avoid reflection from the boundaries of the model.

The 25 m resolution looks small enough to resolve internal waves with wavelength at the level of about 200 m (observations by Nash and Moum (2005), Pan et al. (2007)). An additional sector 1×19.7 km^2, attached to the right of the model domain, is volumetrically equal to the Columbia River estuary, Figure 5.1 b. Two basins, the estuary and the ocean, are connected through the narrow gap initially closed by a lock. In the vertical direction the grid step varied from 1 m resolution near the surface to 10 m in bottom layers (Δz =1, 1, 1, 1, 1, 1, 1.5, 2, 2.5, 3, 5, 10, 10 m). In order to maintain stability according to CFL conditions, the time step was 1 second.

5. VERTICAL STRUCTURE AND WATER MIXING PRODUCED BY A MOVING PLUME NEAR A RIVER MOUTH

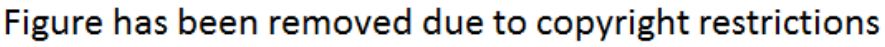

Figure 5.1: Near-field region model domain(a) The fragment of the near coastal zone showing the surface manifestations of IWs acquired by SAR Pan et al. (2007). The rectangle designates the model domain. (b) Zoom of the model domain. (c) The profiles of the background temperature and salinity on the shelf.

The model initialization is similar to that discussed in Stashchuk and Vlasenko (2009). The river outflow was treated as an opening lock gate, allowing water to flow from a basin of comparable volume to the Columbia River estuary, into the stratified sea. The eastern boundary of the estuary was forced with a river flow discharge of 5000 $m^3\ s^{-1}$ and a tidal velocity of 0.5 m s^{-1}.

At $t = 0$ the water inside the estuary was homogeneous with the salinity S_e =8 and the temperature T_e =20°C (observational values, see Stashchuk and Vlasenko (2009)) and density σ_{te} =1.92 kg m^{-3}. When the gate was open, the estuarine water started to move into the open sea as a surface gravity current, where the initial background stratification was taken as shown in Figure 5.1 c), with σ_t =14 kg m^{-3} at the surface and σ_t =24.4 kg m^{-3} at the bottom. The motion is produced by the action of three major forcings: the ebb tidal flow, river discharge and the horizontal pressure gradient caused by the density difference between the sea and the estuary.

Figure 5.2 shows how grid lengths can be expanded towards the boundary with exponential or power functions: red $\Delta y = exp(3.5 + 0.1(x - 1151)) - 9$; green $\Delta y = exp(3 + 0.1(x - 1151)) + 5$; blue $\Delta y = 0.25 \times 10^{-6} \times (1152 - x)^6 + 25$. This helps prevent reflections from the boundaries from interfering with the inner grid. For the runs presented here, the power function represented by the blue line was used.

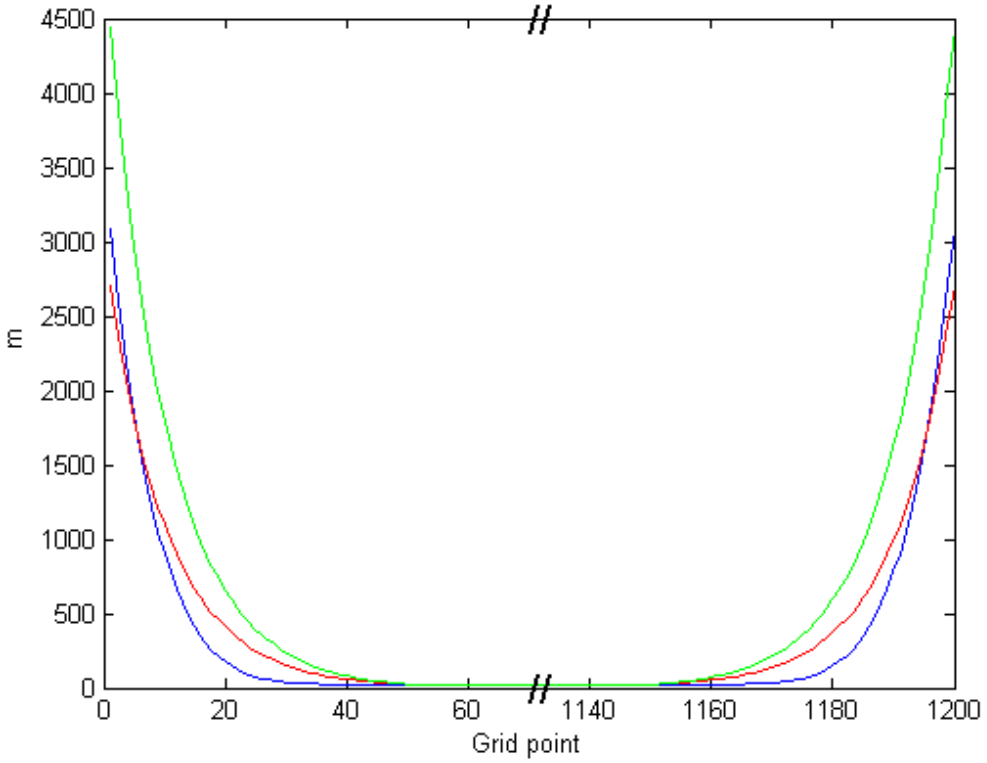

Figure 5.2: Telescoping grid cell length in 50 cells adjacent to the north and south boundaries. Red and green lines represent an exponential increase of the grid step length for two different telescopic grids. Blue line shows a power function.

There are many tunable parameters within MITgcm, this is a description of their set-up for this investigation. Implicit diffusion and viscosity is used so the horizontal and vertical coefficients must be defined. The horizontal Laplacian frictional dissipation coefficient (viscAh) was set to 0.5 m^2 s^{-1}. This value was chosen by considering the velocity scale and grid spacing in order to produce an appropriate Reynolds number, such that grid scale viscous effects may be resolved. Similarly the vertical dissipation coefficient (viscAz) was set to 0.001 m^2 s^{-1}. A no-slip condition is applied to tangential velocities, so u=0 at boundaries in y, v=0 at boundaries in x and u=v=0 at z=-H. These conditions were chosen over slip boundaries as they are realistic for viscous flows. Horizontal diffusion coefficient for temperature (diffKhT) and salt (diffKhS) were set

to 0.5 m^2 s^{-1}, due to the small time step with the boundary condition of zero fluxes across the boundaries. The vertical diffusion coefficients for temperature (diffKzT) and salt (diffKzS) were set to 1×10^{-5} m^2 s^{-1} since vertical motion is small compared to horizontal motion and has the boundary condition $\frac{\partial}{\partial z} = 0$. The Coriolis parameter was calculated using Equation 4.8 and set to 1.053×10^{-4}. A free surface is used rather than a rigid lid as the time step is small enough for fast waves.

Stashchuk and Vlasenko (2009) also found that, despite the plume being a surface phenomenon, the bottom topography plays an important role in shaping the plume and internal waves. Therefore, a realistic topography to a depth of 40m was used as shown in Figure 5.3.

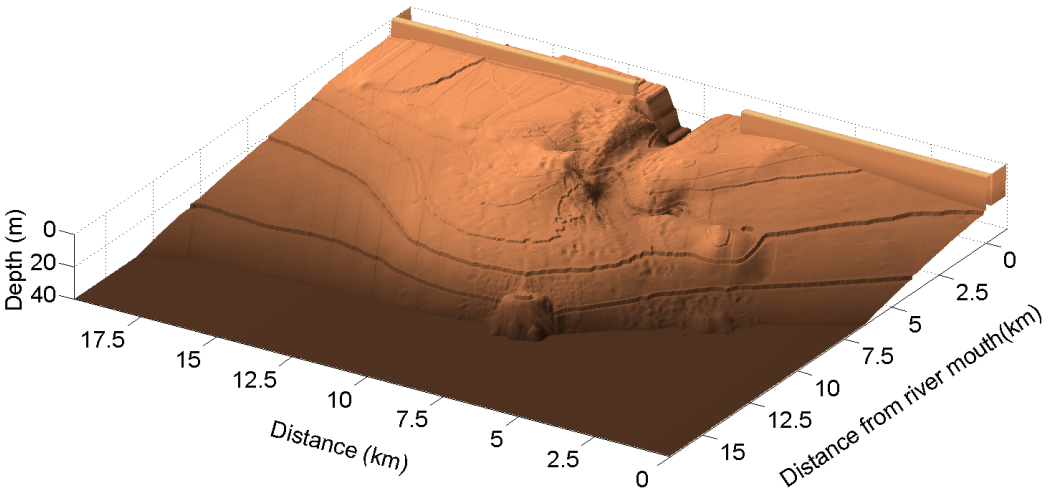

Figure 5.3: Detailed topography of model domain showing the central channel, which appears to steer the central jet.

An initial model run was produced with uniform mixing in order to confirm that sub-grid scale processes should not be neglected. The Richardson number values were calculated for a cross-section through the plume and are presented in Figure 5.4 (with density contours in black). This Figure clearly shows that for considerable areas within the plume having sub-critical Richardson numbers (<0.25), indicating that sheer in-

duced mixing should be taking place which is not being represented due to the relative grid coarseness compared to the small-scale turbulent processes. As a result, use of the PP81 mixing scheme, as described in section 4.7.4 was used with the following values, ν_b=10^{-3} m^2 s^{-1} and κ_b=10^{-5} m^2 s^{-1}, ν_0=1.5·10^{-2} m^2 s^{-1}, α=5 and n=1. Such a parametrisation for the vertical turbulent viscosity ν and diffusivity κ increases their values in the areas where the Richardson number is small.

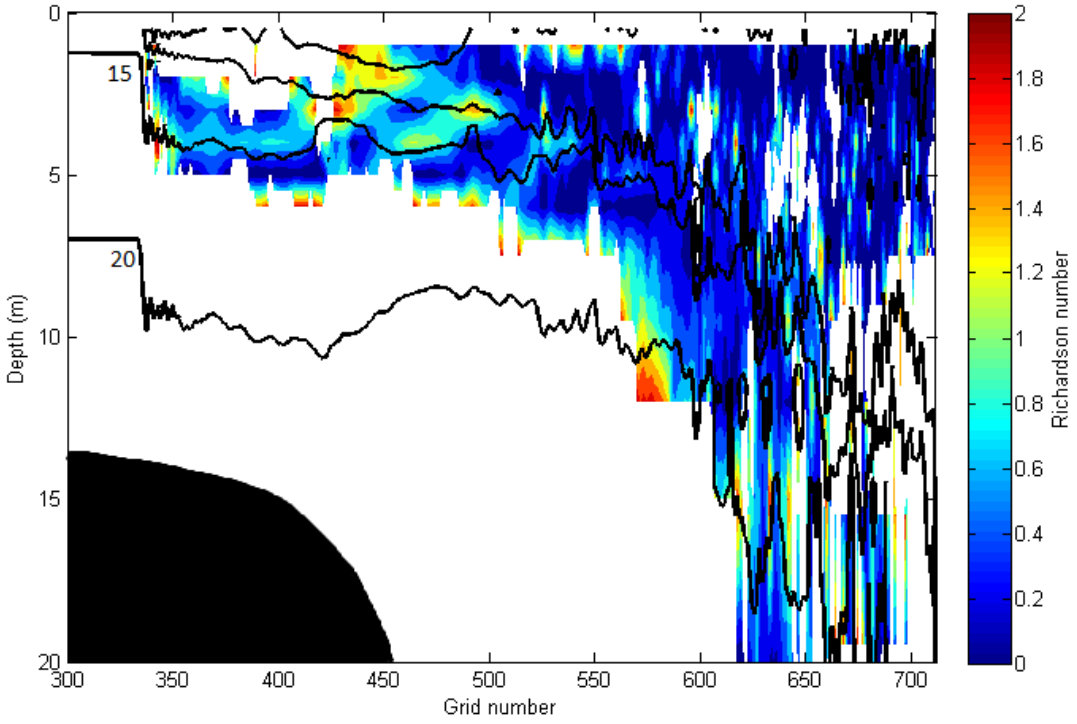

Figure 5.4: Cross-section through the modelled Columbia River plume front and river mouth of Richardson number overlaid with density contours (black lines)

5.2 Dynamic processes controlling the interaction of the Columbia River Plume with sea waters near the river mouth: Radiated internal waves

Modelling of the Columbia River Plume dynamics using the MITgcm as reported in Stashchuk and Vlasenko (2009) allowed the authors to investigate the conditions of

generation of a packet of first mode internal waves radiated from the plume. The comparison of the model wave parameters (amplitude and wave length), with the observational data of Pan et al. (2007), showed a good agreement. The generated wave packets were reproduced successfully thanks to the non-hydrostatic dispersion included in the model, which is normally ignored in a number of oceanic models that exploit the hydrostatic approximation. Another important condition that made a successful model validation against the observational data possible, was the fine model resolution used in Stashchuk and Vlasenko (2009) that allowed the numerical viscosity and dispersion to be reduced to a level where they did not affect the generated waves.

Some more details on the model results are discussed below, but here the basic findings from the paper by Stashchuk and Vlasenko (2009), which are relevant to the present study are summarised. It was found that in the beginning of the ebb phase that the tidal flow, river discharge and horizontal density gradient acting together moved fresh river water from the mouth. This water collided with the stagnant shelf waters and sank at the leading edge of the plume forming a head of the gravity current. At the first stage of the ebb phase (first 3 hours) the current from the mouth was strong enough to arrest a system of internal waves that was generated inside the plume. These waves are released from the plume and propagated independently as a rank-ordered packet of internal solitary waves when the plume decelerated due to the radial spreading and weakening of the tidal current.

The mechanism described above is illustrated in Figure 5.5. Here, the free surface zonal velocity taken across the front of the moving plume is shown for different moments of the plume development. For a comparison, the dashed line shows the instant velocity of the plume propagation. It is clear that at the first stage of the plume spreading (Figure 5.5 a) the radial velocity inside the plume exceeds the velocity of the plume expansion, so that the effect of overtaking velocity discussed in Luketina and Imberger (1987) is reproduced by the model quite clearly. Note also that the leading edge of the

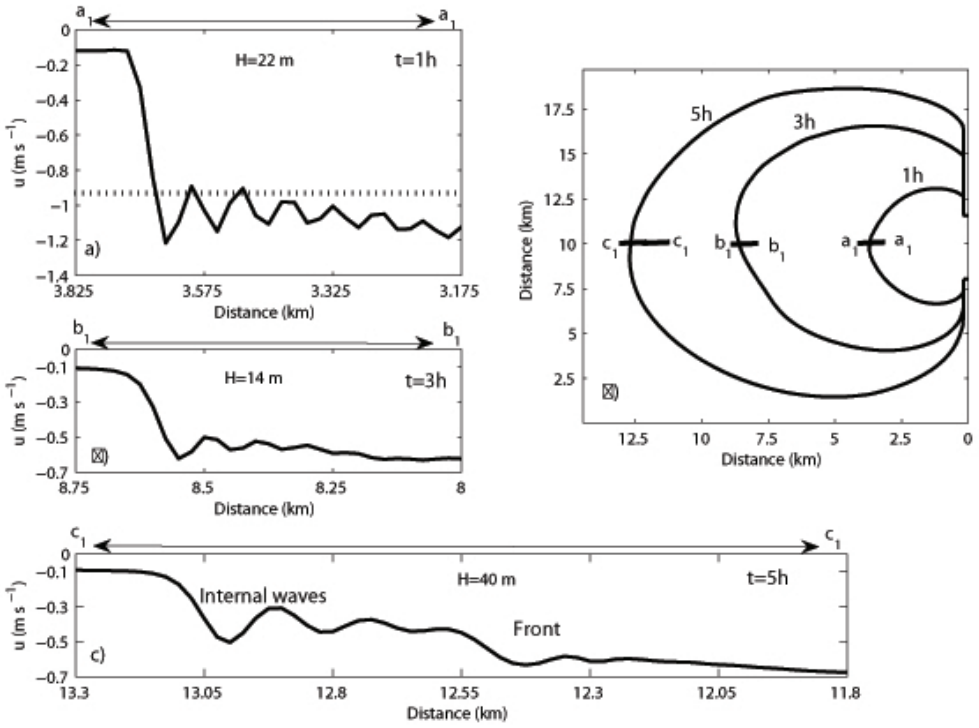

Figure 5.5: Free surface zonal velocity taken across the propagating plume front at $t = 1\,\mathrm{h}$ (panel a), $3\,\mathrm{h}$ (panel b) and $5\,\mathrm{h}$ (panel c) after the beginning of the ebb phase. The corresponding sections across the outer boundary of the plume for the appropriate moments of time are shown in panel d. The dashed line depicts an instant velocity of the plume propagation.

plume is not smoothed, but eroded by a short-scale wave structure with a horizontal wave length of about 90 m. With progressing time, the overtaking velocity drops almost to the level of the plume spreading speed (see Figure 5.5 b), however the wave system is still arrested within the plume near its outer boundary. The analysis of the wave radiation conditions are discussed below, but here just the fact of their location near the head of the gravity current, as well as their reduced amplitude (in comparison with panel a) is stated.

The stage of the wave release is shown in Figure 5.5 c. The radiated waves left

the moving front behind and propagated freely as an undulating bore that gradually transforms into a packet of internal solitary waves. One can notice that the spatial scale of the radiated waves has changed. The leading waves have a wavelength of about 200 m, which is well resolved with the grid resolution of 25 m taken in the main series of calculations. Note that some runs were conducted with a grid twice as fine (Δx=Δy=12.5 m) in order to investigate the sensitivity of the model to the horizontal resolution. The result of this analysis is reported in Stashchuk and Vlasenko (2009) (see their Figure 12) with the conclusion that the taken resolution is good enough to reproduce the radiated waves. In fact, the problem of the numerical dispersion that can develop in numerical schemes with large leptic ratio (the ratio of the grid resolution to the total depth) is quite a serious issue that has been investigated recently in a series of papers (see, for instance, Scotti and Mitran (2008); Vitousek and Fringer (2011)). In application to this particular study, some evidence of numerical dispersion can be found in Figure 5.5 a, where the leptic ratio is of order 1. However, with the propagation from the mouth seaward, the contribution of numerical dispersion decreases, and the physical dispersion predominates, far away from the mouth in the deep part of the ocean where the leptic ration is less than 0.5. The confirmation of this fact is the good agreement between observed and numerical parameters of the radiated waves.

A more detailed spatial structure of the plume (vertical and horizontal) developed by $t = 6$ h, as well as the radiated wave system are shown in Figure 5.6. Here, a surface density overlaid with the horizontal velocity gradient (panel a) represent a plan view of the developing plume. It is clear that, by the end of the ebb phase ($t = 6$ h), the wave fronts are completely detached from the whole body of the plume and propagate independently as radiated waves. The vertical structure of these waves (for the cross section $a - a$ shown in panel a) is seen in Figure 5.6 b. It can be treated as a first-mode rank-ordered internal wave packet. A zoom of this wave fragment (a dashed rectangle depicted in Figure 5.6 b) is presented in Figure 5.7.

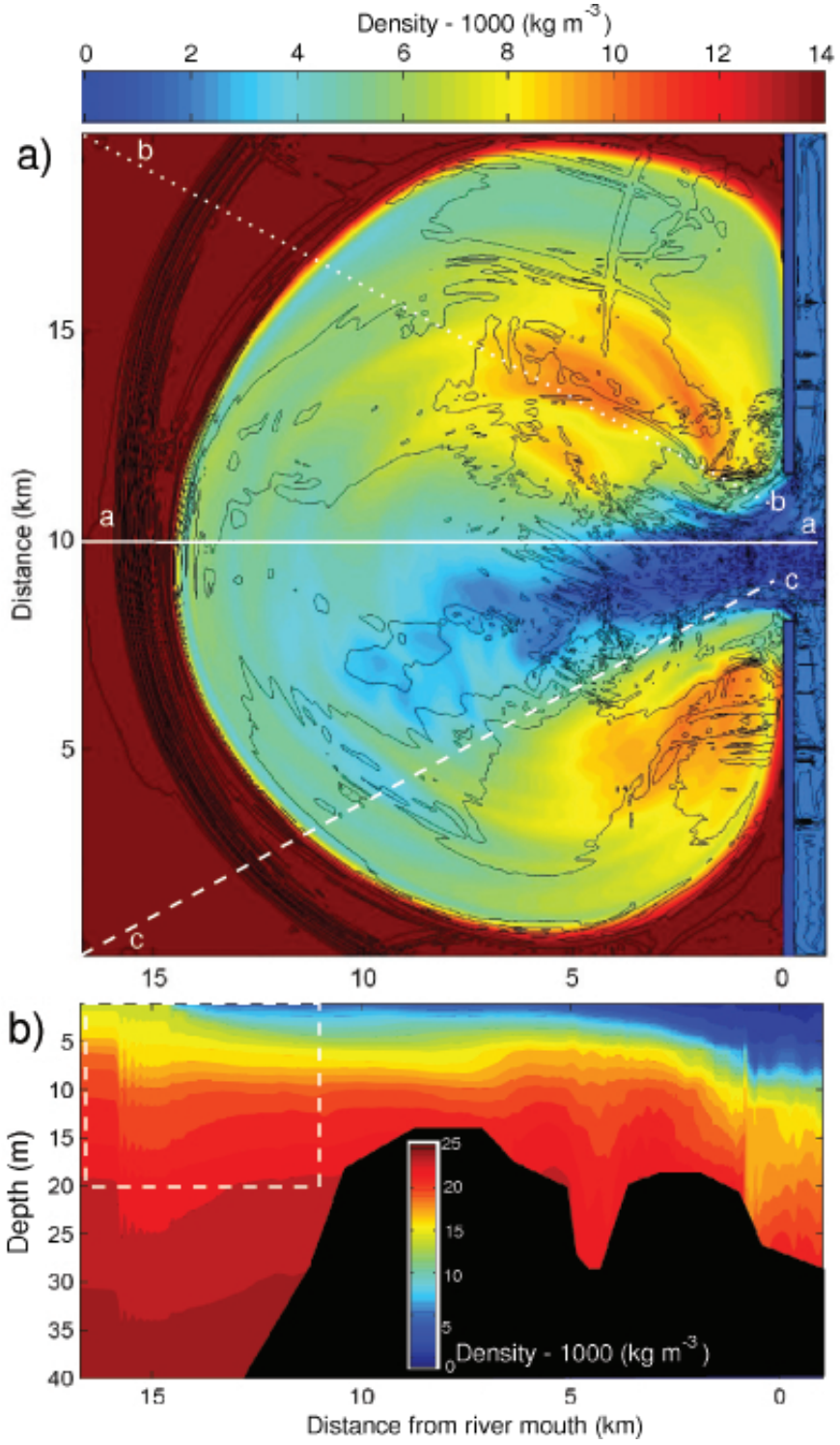

Figure 5.6: (a) Surface density overlaid with the gradient of horizontal velocity at $t = 6$ h. (b) Vertical density section taken in the middle of the plume (cross section a-a in panel a).

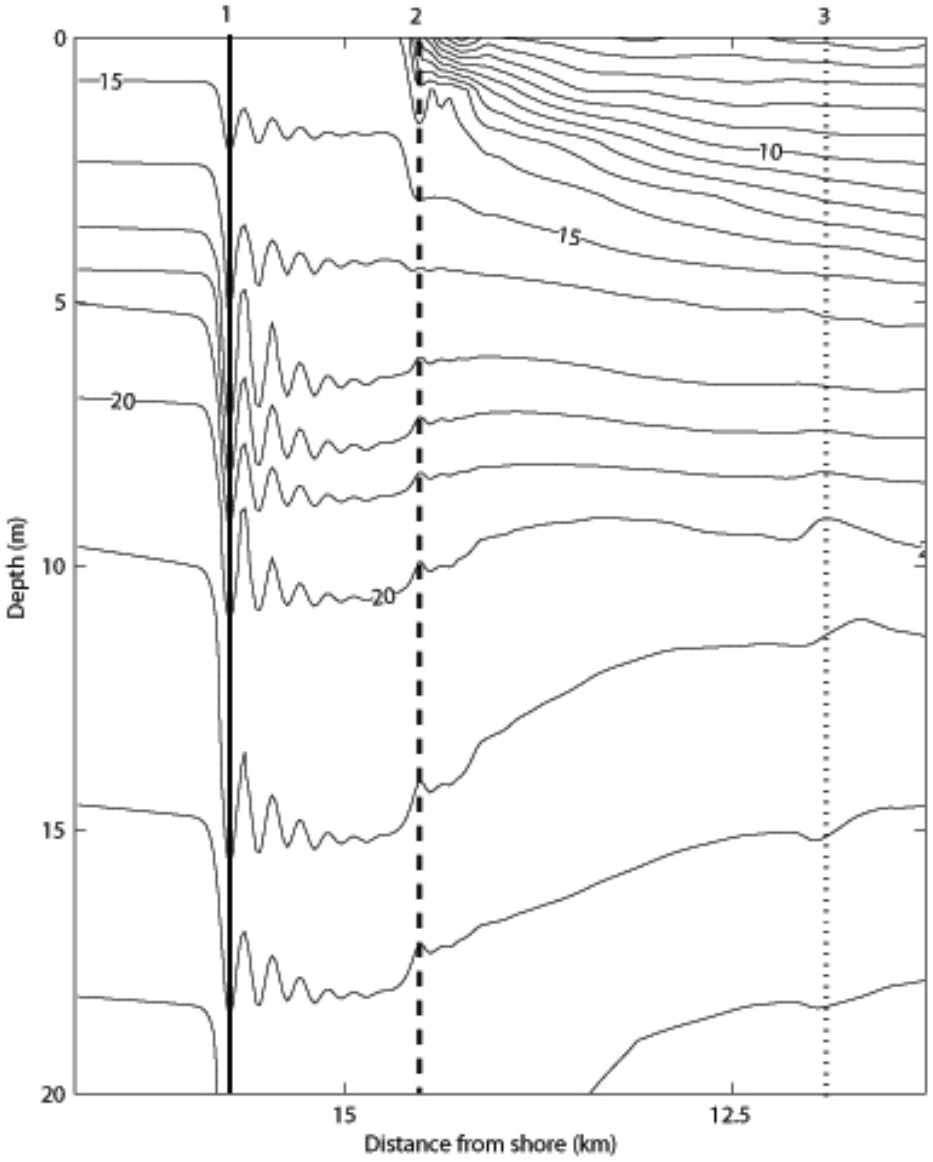

Figure 5.7: Zoom of the fragment of the density field depicted in Figure 5.6 b by a dashed rectangle. The first-mode internal wave packet is marked by a solid line, the second-mode waves is shown by a dashed line and third mode by a dotted line.

It is clear that by $t = 6$ h the leading wave system has completely detached from the head of the buoyant flow. It resembles a propagating first-mode solibore on its initial stage of disintegration into a rank ordered packet of internal solitary waves. The detailed analysis of their spatial characteristics conducted in Stashchuk and Vlasenko (2009) has shown that these waves are close to those observed from space on SAR images by Jay et al. (2010), Pan et al. (2007), Pan and Jay (2009*b*) and measured in-situ Nash and Moum (2005).

After $t = 6$ h, the plume front still propagates seaward, but with substantially slower velocity. Its dependence on time calculated for the section a-a, b-b and c-c depicted in Figure 5.6 a is shown in Figure 5.8. An interesting feature of the gravity current at this stage is that it still contains some wave forms at its leading edge, which have not yet escaped from the plume with the first-mode wave packet. Analysis of the isopycnal structure reveals counter phase displacements in surface and bottom layers, which is particular to the second baroclinic mode (find dashed line in Figure 5.7). Moreover, 2.5 km behind the second mode, the third mode wave can be identified (dotted line in Figure 5.7). If so, these waves should have a much smaller speed of propagation which can explain why they are still arrested by the plume. Figure 5.8 b shows the solution of the following boundary value problem,

$$\begin{aligned} w_{zz} + \frac{N^2(z)}{C_i^2} w = 0, \\ w(0) = 0, \quad w(-H) = 0, \end{aligned} \tag{5.1}$$

calculated for the first, second and third baroclinic modes over the depth range of the model domain. Here, w is vertical velocity, C_i is the phase velocity of the i-th baroclinic mode (i =1,2,3,...).

It is clear, that for separation to take place the phase speed must exceed the plume propagation velocity. By the end of the six hour run, the plume was still propagating to the west with a speed of about 0.5 m s^{-1}, see Figure 5.8 a (comparable with the values reported in Pan et al. (2007)). Since the maximum depth of the domain was

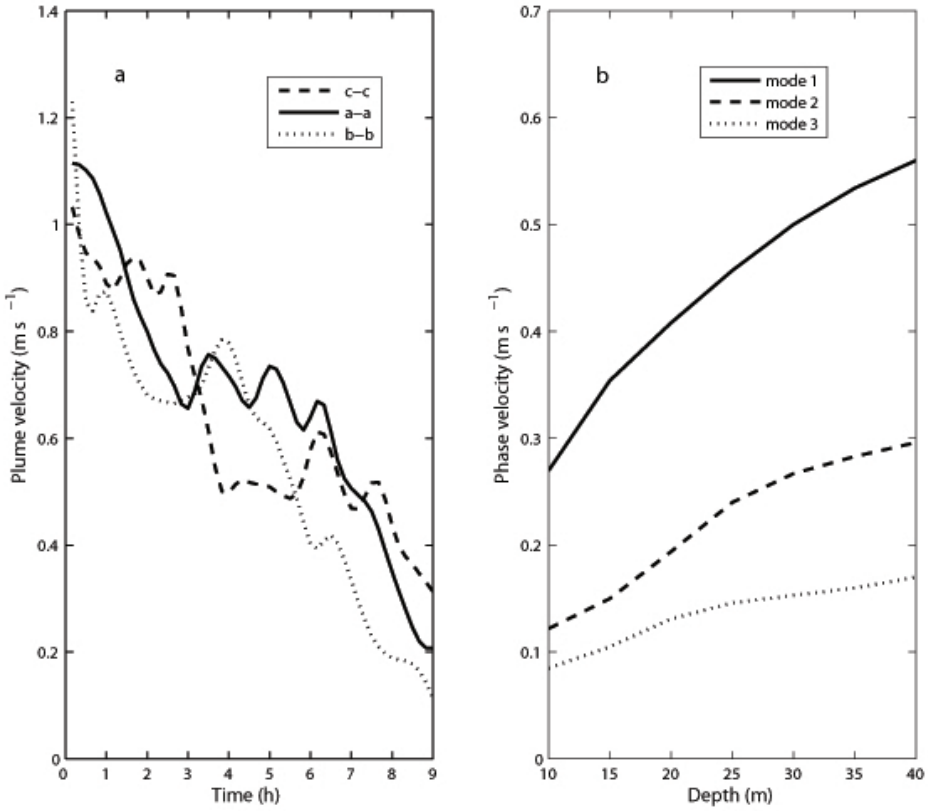

Figure 5.8: (a) The velocity of the plume expansion along cross section a-a, b-b, and c-c shown in Figure 5.6 a. (b) Phase velocities at varying depths for three first internal modes produced as a result of solving boundary value problem (5.1).

40 m, only first mode waves can separate from the plume. It is expected, however, that with the increasing depth and further deceleration of the plume due to radial spreading, the second mode will ultimately separate from the plume and propagate freely when the second-mode Froude number drops below 1. Figure 5.9 clearly illustrates this statement. It shows a density field, taken at $t = 8$ h, of the cross-section b-b depicted in Figure 5.6 a.

At least three wave systems can be identified here. First of all, a well developed first mode internal wave packet is clearly seen at a distance of $24 - 25$ km from the mouth. The second wave fragment with the characteristics of a second baroclinic mode looks detached from the plume at a distance of $19.5 - 20$ km from the mouth (find vertical section 2 in Figure 5.9). Its amplitude is comparable with the first-mode waves which can lead to similar effects on water mixing. Note that the horizontal scale of the second mode wave is larger (the wavelength is nearly $\frac{1}{2}$ km) which can affect the internal mixing of a larger area (discussed in the next section). Finally, a third mode wave fragment is still arrested at the edge of the plume (section 3 in Figure 5.9). For this wave, the propagation speed of the plume is still supercritical (see Figures 5.8), however sooner or later it will inevitably detach from the gravity current when it decelerates below 0.15 m s^{-1}.

Note that the mechanism described above, that is the successive radiation of the first, second, third etc. modes, is not completely the same in all directions of the spreading plume. In fact, the plume is a three-dimensional object whose spatial structure is sensitive to local characteristics of the marine environment (the depth, first of all). As an illustration of this fact, Figures 5.10 shows three independent first-mode wave packets located at 27.5, 26.5 and 24.5 km (evidence of a multi-frontal nature of the plume as discussed below), whereas a second mode wave located at 23 km from the mouth are still arrested in the head of the gravity current, although the structure of the latter shows that these waves are very close to their detachment.

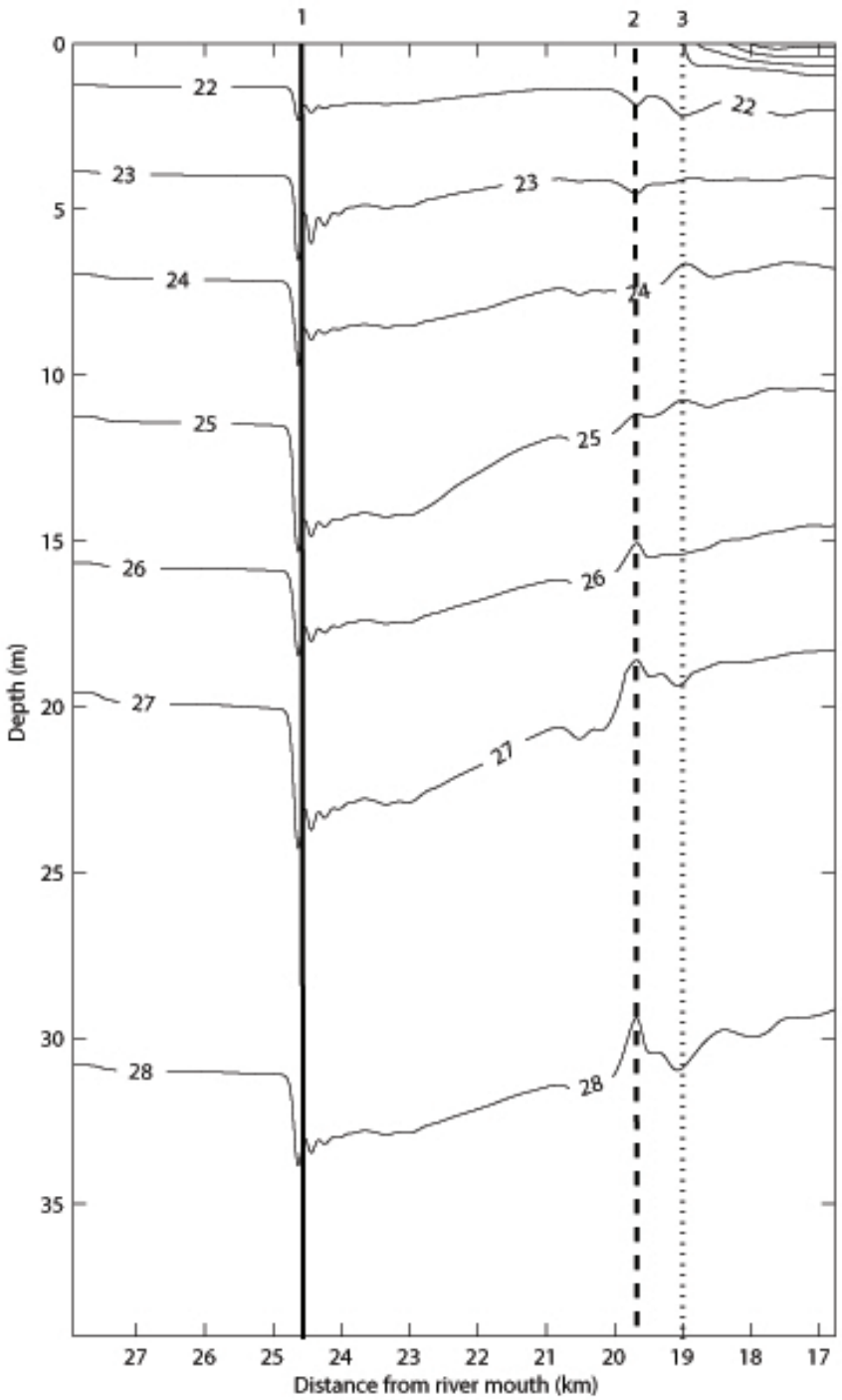

Figure 5.9: Vertical density cross section taken at $t = 8$ h along the line b-b depicted in Figures 5.6 a.

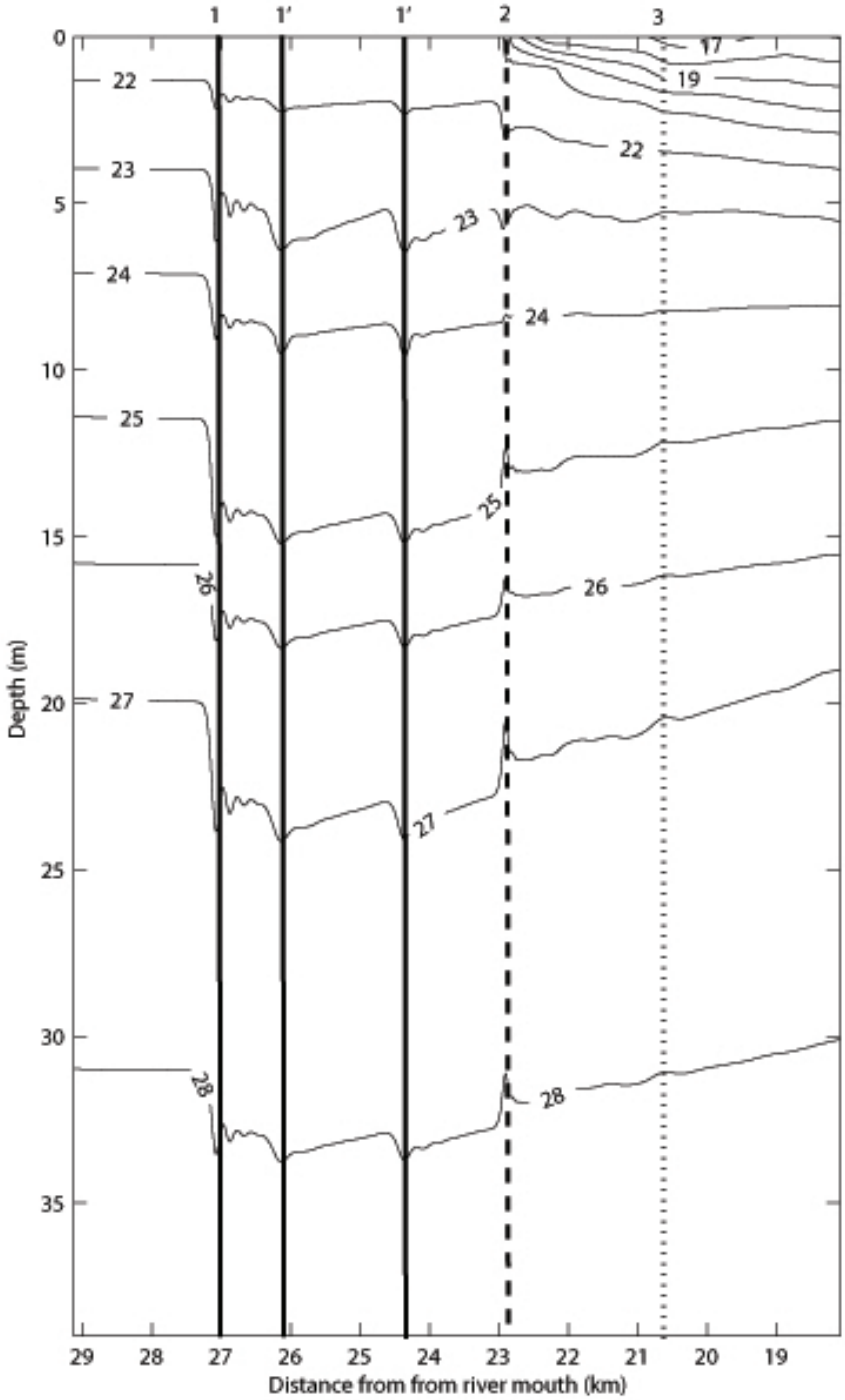

Figure 5.10: Vertical density cross-section taken along the line c-c shown in Figure 5.6 a.

5.3 Non-hydrostatic effects in plume-sea interaction

The non-linear evolution of internal waves is a non-hydrostatic process, and so to try to model their generation with a hydrostatic model will result in errors. Whilst these inaccuracies may not be large enough to significantly affect large-scale model results, neglecting non-hydrostaticity will favour the non-linear process of wave steepening (Hodges et al., 2006). As making the hydrostatic approximation can reduce computing time by over 40% compared to the non-hydrostatic mode, and as long as many existing models still use this approximation, it is of interest to make a comparison between hydro-static and non-hydrostatic outputs for the considered case.

Several runs have been conducted, of which the typical results are given here. The sharp interface between the density of the plume and the surrounding waters allows the plume evolution to be tracked. Figures 5.11 and 5.12 show the propagation of the plume front at a depth of 1 m at each hour of the model run for both the hydrostatic and non-hydrostatic cases. It can be seen that a jet steered by topography initially directs the plume towards the south, counter to the effects of rotation. As the plume spreads and thins, the effects of Coriolis push the plume to the north increasing its contact with the coast in this direction. When compared the two cases show little difference in the extent to which the plume spreads over time however slight differences can be seen around the central jet region.

The qualitative conclusion of a weak sensitivity of the plume characteristics (spatial distribution and vertical structure) to the non-hydrostatic pressure contribution can be made for the range of model input parameters considered here. However, this is not the case for internal waves generated at the leading edge of the plume. The non-hydrostatic effects are highly important for the accurate predictions of their parameters. Some details of this analysis will now be presented.

A comparison of horizontal velocity gradient in Figure 5.13, shows that the non-

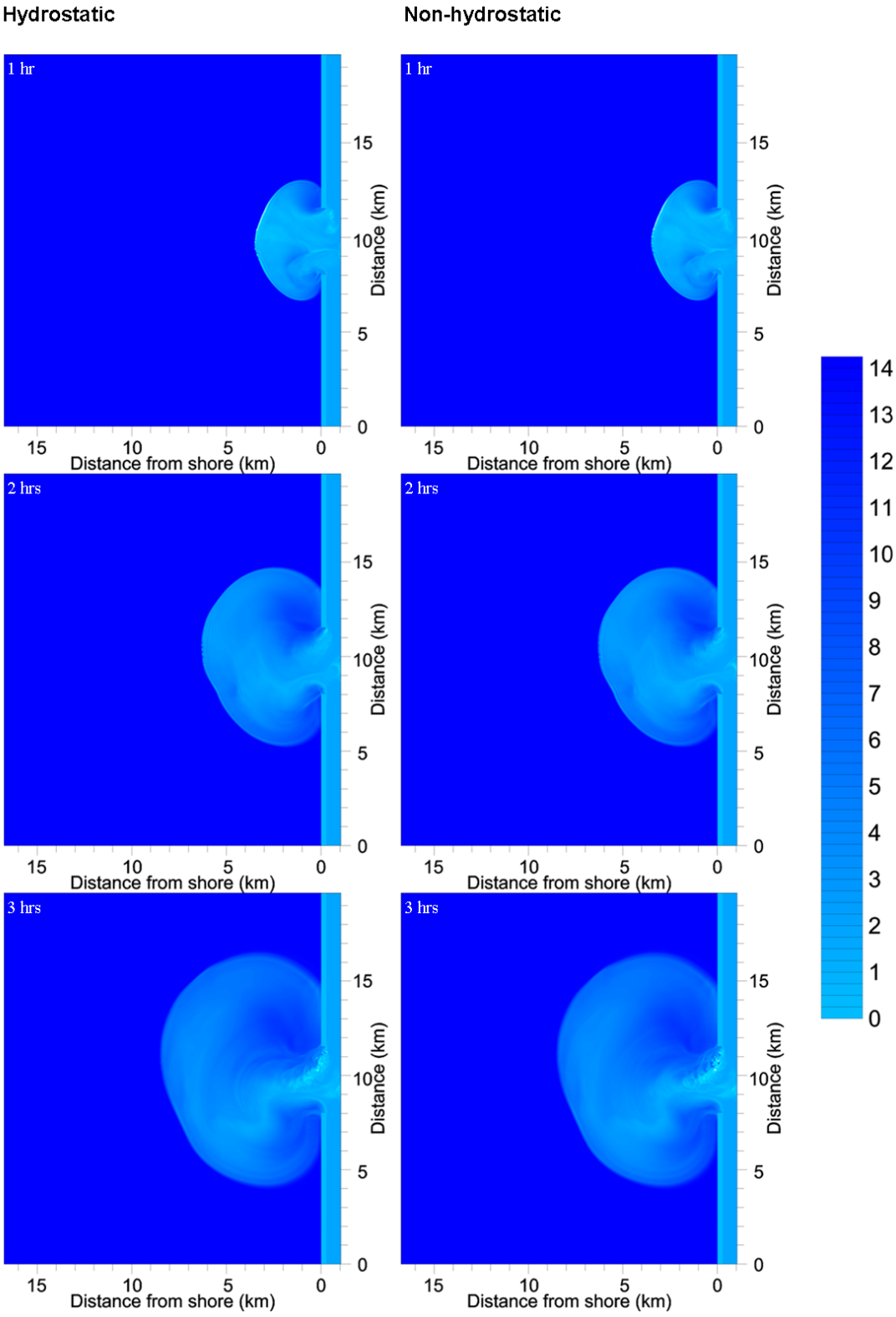

Figure 5.11: Model predictions of density-1000 kg m^{-3} at 1 m depth for hours 1, 2 and 3 of the model run. Left column shows hydrostatic results, right column shows non-hydrostatic.

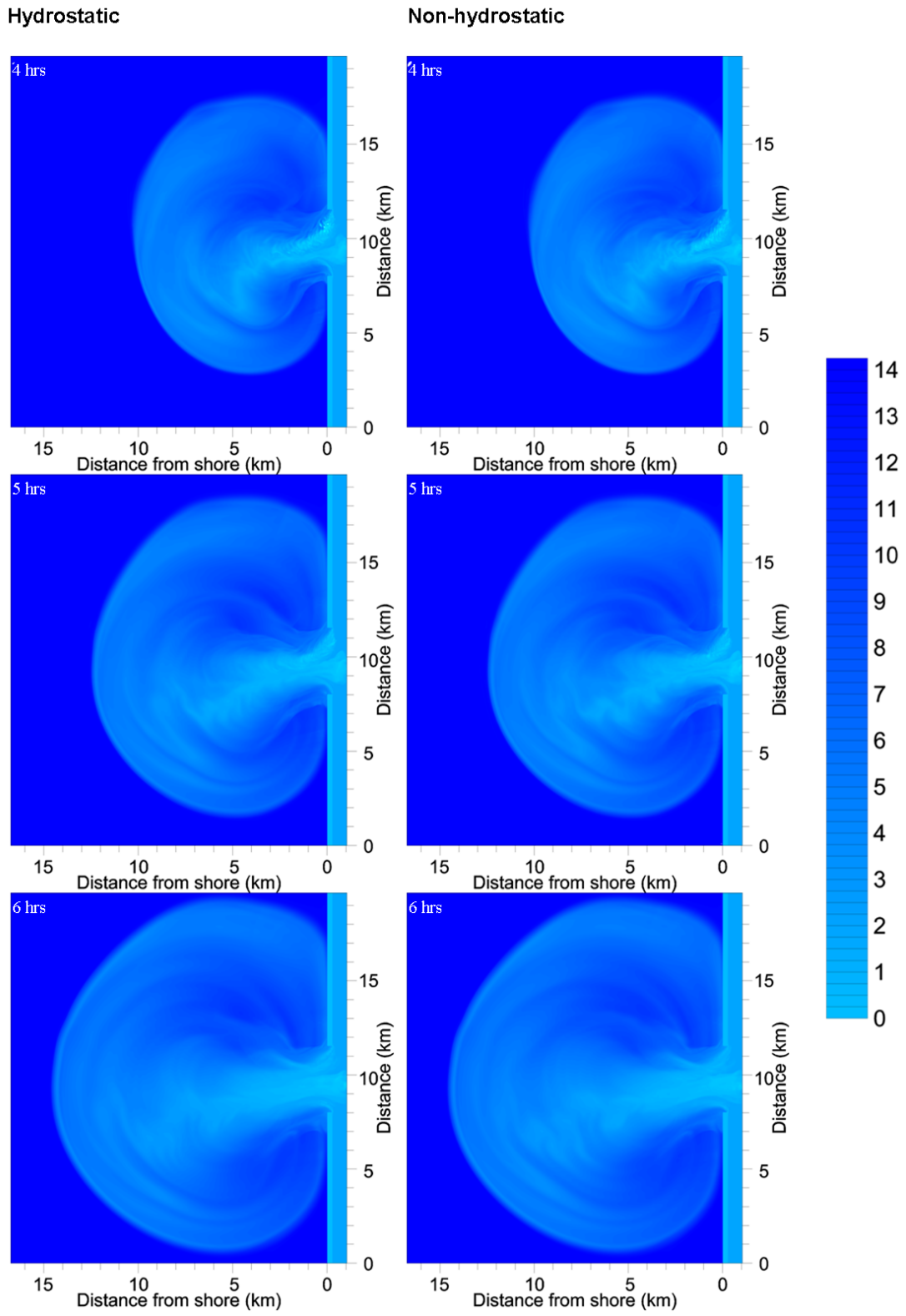

Figure 5.12: Model predictions of density-1000 kg m^{-3} at 1 m depth for hours 4, 5 and 6 of the model run. Left column shows hydrostatic results, right column shows non-hydrostatic.

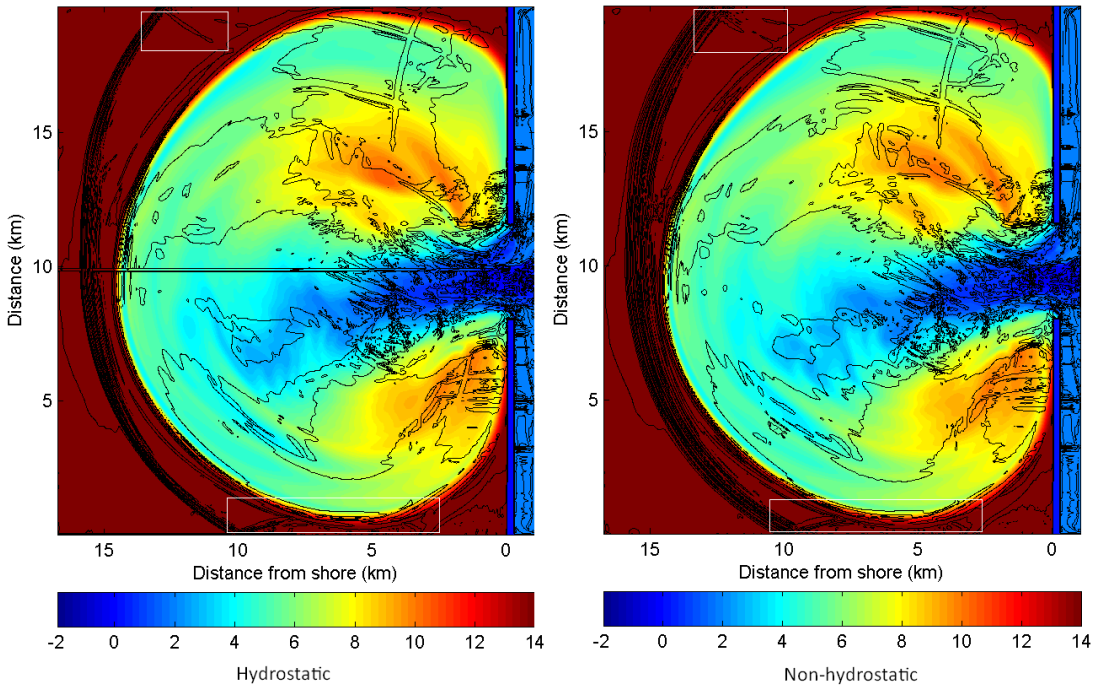

Figure 5.13: Density from the first model layer with horizontal velocity gradient (black lines) showing internal wave locations

hydrostatic generates a larger band of internal waves. By taking cross-sections through the model domain perpendicular to the coast and passing through the most westerly point of the plume shows the internal waves generated by the plume. Figure 5.14 shows the differences in the first mode internal wave generated under non-hydrostatic and hydrostatic conditions respectively, yet, the representation of the plume waters appear to be similar. For the non-hydrostatic case the generated first mode waves are larger than in the hydrostatic case, as vertical momentum is conserved. Closer inspection of the density profiles (Figure 5.15) shows a clearly separated first mode internal wave packet. The scale of variation between the first mode internal waves in the two plots is quite significant, but both show good agreement in the shape and size of the head of the plume, where the second mode wave is located.

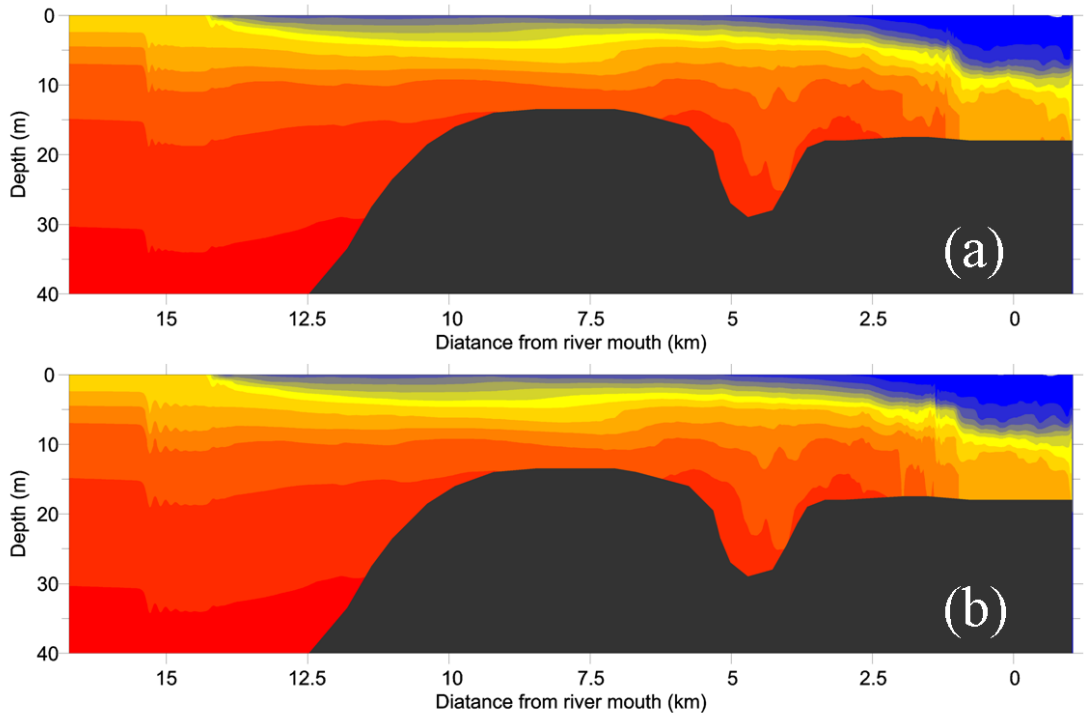

Figure 5.14: Density profiles at hour six of the (a) hydrostatic and (b) non-hydrostatic model runs.

5.4 Mixing processes at the boundary of the moving front

One of the most powerful sources of internal mixing is oceanic internal waves developing and breaking in the interior. A specific feature of this source is that the maximum vertical velocity shear is usually located in a layer of density jump, where mixing producing inertial forces are compensated by buoyancy forces. Normally, only large-amplitude internal waves can overcome this stability producing vertical mixing during their break-down. In the area of the Columbia River plume, some extra external velocity shear can be produced by wind stresses. As it was shown in Pan and Jay (2009*b*), such externally induced shear can modify the vertical structure function of internal waves in such a way that the maximum amplitude is shifted from the interface, 5 m deeper, which can lead to a situation where the Richardson number drops below the critical

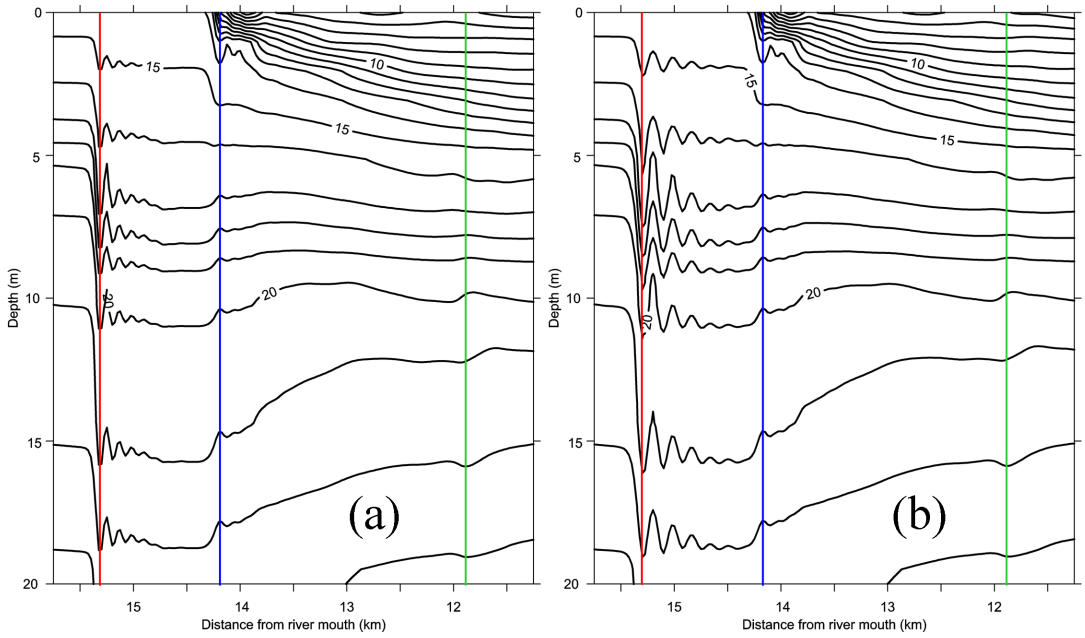

Figure 5.15: Density profile showing internal waves and the head of the buoyant flow at hour six of the hydrostatic (a) and non-hydrostatic (b) model runs. Coloured lines show mode 1 (red), mode 2 (blue) and mode 3 (green) internal waves.

value ($Ri = 0.25$).

Note, however, there is also another possible scenario of further intensification of vertical mixing in a moving front. It relates to the new systems of second and third mode internal waves found in this study. As it is clear from Figures 5.16, where the first three eigen functions of the boundary value problem (5.1) are shown, the strongest shear of the vertical velocity of second and third modes are located not in the pycnocline but are shifted to the layers with smaller buoyancy frequency (see Figures 5.16 d). As a result, this can reduce the Richardson number there, which facilitates water mixing.

Direct calculations of the vertical shear $\sqrt{(\partial u/\partial z)^2 + (\partial v/\partial z)^2}$ for the leading first and second mode waves shown in Figures 5.9 and 5.10 illustrate the fact that the second mode waves can produce an even stronger effect on vertical mixing taking into account that they provide stronger shear. They have longer wavelengths, so they cover larger areas for mixing as it is seen from Figure 5.9.

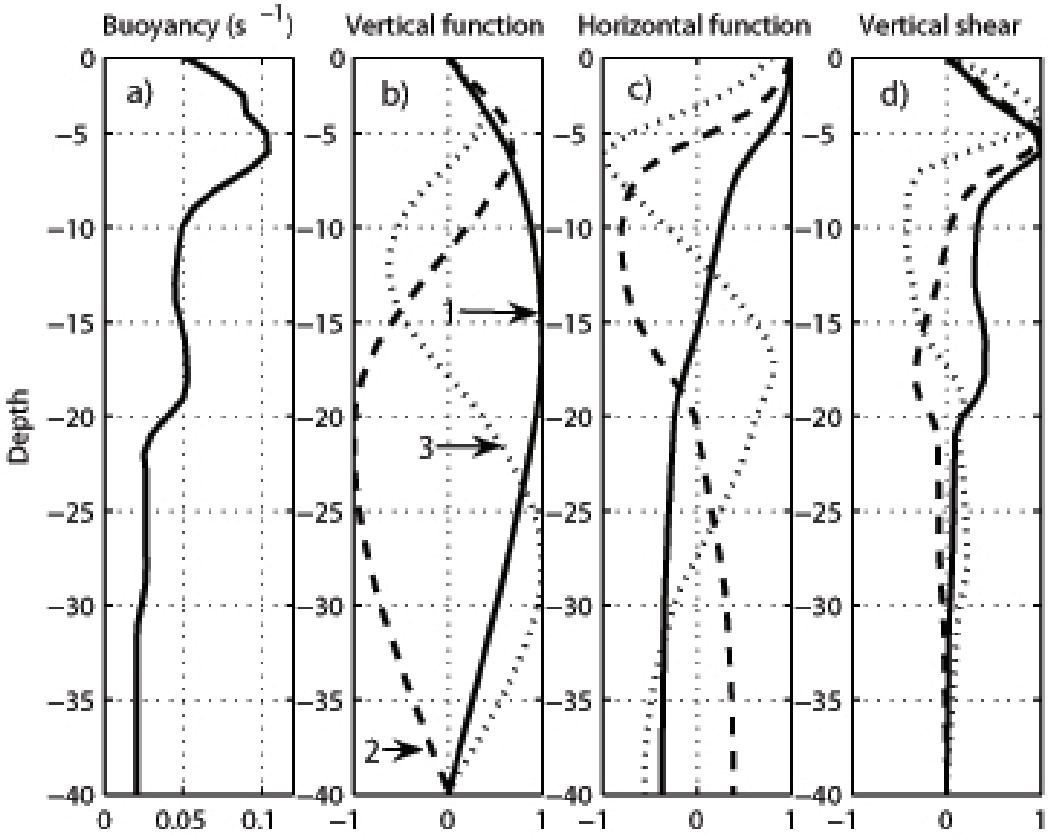

Figure 5.16: The buoyancy frequency profile (a), normalized vertical displacement (b), horizontal velocity (c), and vertical shear of horizontal velocity (d) calculated from the boundary value problem (5.1).

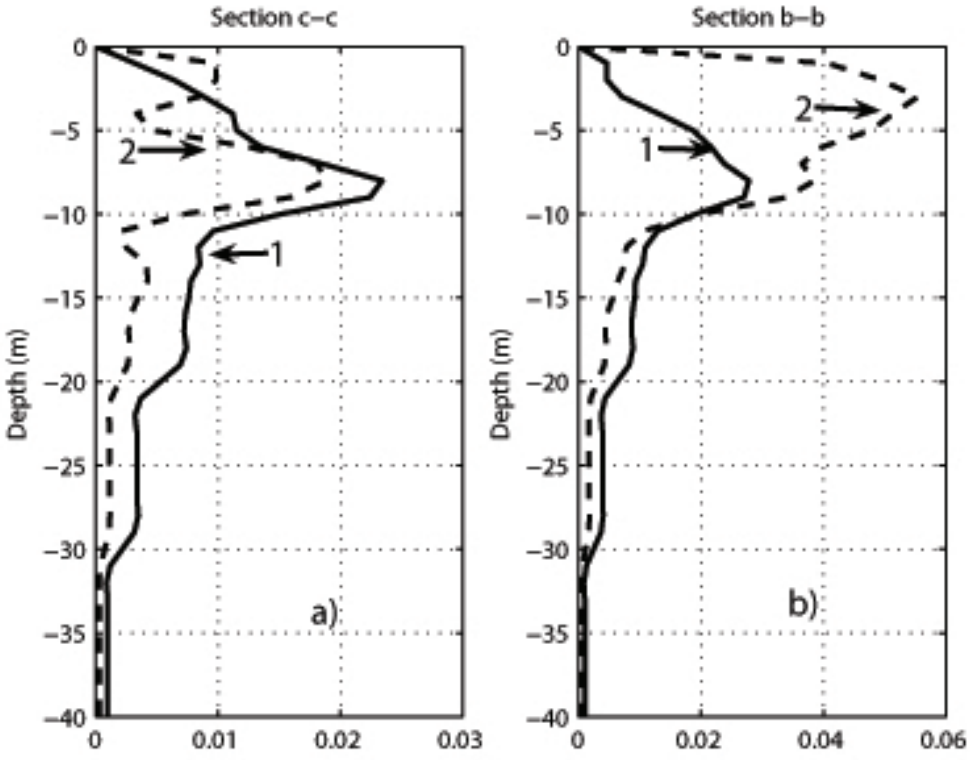

Figure 5.17: Vertical shear $\sqrt{(\partial u/\partial z)^2 + (\partial v/\partial z)^2}$ calculated for the leading first mode and second mode waves shown in Figures 5.9 (panel a) and 5.10 (panel b). Here u and v are two components of horizontal velocity.

5.4.1 Mixing processes within the plume

It is clear generally, that the plume thickness is controlled by two basic competing processes: the plume's expansion which leads to its thinning, and the river discharge, which supplies water making it thicker. A third factor that can also affect the plume structure (and its thickness) are the mixing processes developing at the interface between the plume and underlying sea waters. Depending on what process predominates, upward or downward salt flux, one can distinguish situations of entrainment or detrainment. In fact, this is one of the basic ecological questions on the mechanism of river water dispersion, which determines the ultimate impact of the river discharge on the sea environment. With respect to the Columbia River Plume, it was found in McCabe et al. (2008), on the basis of the observational data (drifter tracks), that entrainment predominates well beyond the lift-off zone (close proximity to the river mouth). This was later confirmed by the application of a numerical model in McCabe et al. (2009).

Note, however, that the numerical modelling in McCabe et al. (2009) was conducted using the hydrostatic model ROMS, which under predicts non-linear internal waves and thus water mixing. In addition, the modelling was conducted on a relatively coarse grid (400 m horizontal resolution), which does not reproduce the smaller sub-grid processes, which can be quite substantial (the effect of short internal waves, for instance, whose wavelengths according to observations Pan et al. (2007) are about 200 m). In this section a salt balance analysis for the Columbia River Plume is conducted with the aim to identify the regime of the water mixing on the lower boundary of the plume, i.e. entrainment or detrainment, taking into account the short-scale processes developed there.

To rectify the mixing conditions occurring on the lower boundary of the plume, one extra transport equation for the passive tracer was introduced into the model. The initial concentration of the passive tracer was set as $C = 1.0$ in the estuary, and as $C = 0$ outside it. It is clear that, as long as the tracer is passive and does not participate

in the dynamics of the plume, its spatial distribution and temporal evolution can show how two water masses mix. Figures 5.18 a and b represent the topography of the plume at two different moments of its development. The concentration $C = 0.1$ was taken as a plume lower boundary. In both panels the lift-off zone near the mouth can be clearly identified. With the increase in distance from the mouth, the thickness of the plume decreases in a radial direction. The quantitative characteristics on the plume thickness can be found in the bottom "projections" (Figure 5.18b). The plume occupies almost the whole water column in the lift-off area, gradually thinning to the outer boundary.

The qualitative information on the predominance of entrainment or detrainment at the boundary between river and sea waters can be obtained from the analysis of vertical fluxes. The vertical velocity values were found at the depth where the tracer isoline C reaches a value of 0.1 and is presented in Figures 5.18 c and d for 5 and 3 hours of plume propagation. Here, the red colour corresponds to the positive velocities directed upward and blue presents the motions directed downward. It is seen that the red colour predominates in Figures 5.18 c and d, suggesting entrainment. There are some blue areas denoting descending water, however, they are mostly related to internal waves developing inside the plume (to be discussed below). Quantification of the entrainment process obtained by the model at the level of $0.001\,\mathrm{m\,s^{-1}}$ vertical velocities coincides with the estimations of McCabe et al. (2009) obtained on the basis of the analysis of the trajectories of surface drifters.

A more convincing picture on the predominance of the entrainment processes is shown in Figures 5.19 a. Here, the vertical structure of the plume (passive tracer) overlaid with the vertical velocity patterns at time moment $t = 5$ h is shown. To separate plume water from the underlying sea waters, the density isopycnal $\sigma_t = 14$ kg $\mathrm{m^{-3}}$ was used (it is shown in magenta colour).

Figure 5.19 a shows that, apart from the lift-off area near the mouth where the whole water body is in red, only the leading edge of the plume presents the alternation

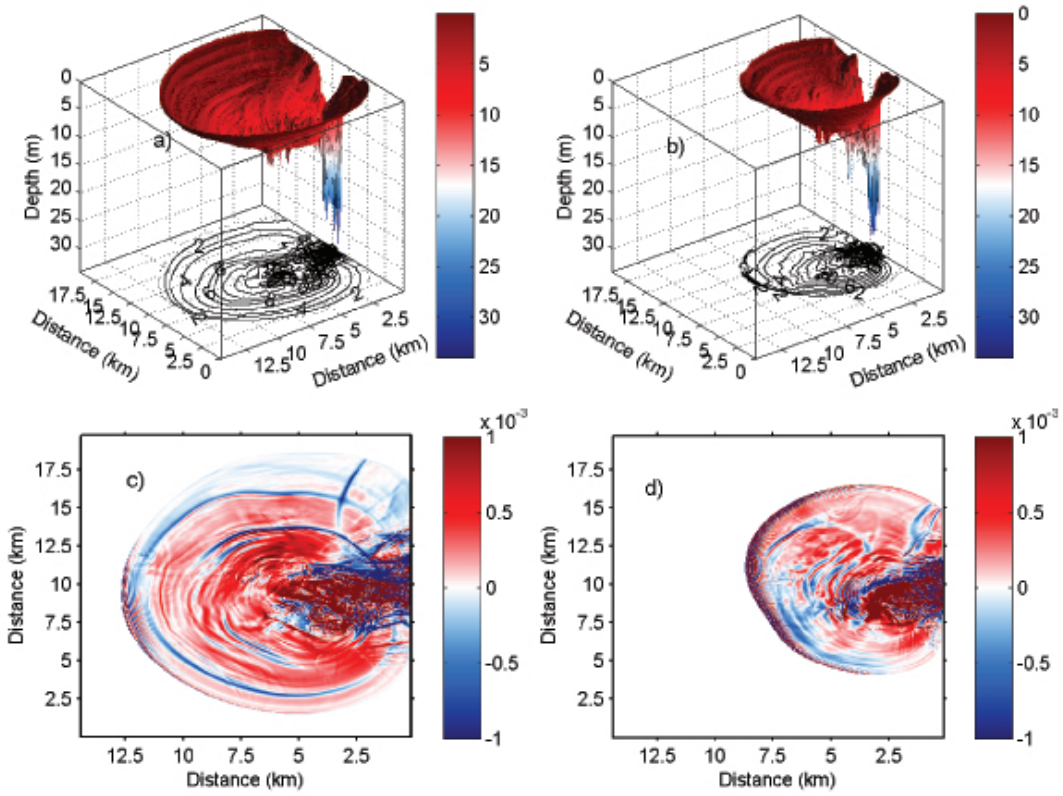

Figure 5.18: The topography of 0.1 isoline of a passive tracer at $t = 5$ h (panel a) and $t = 3$ h (panel b) discharged from the mouth with the river water. Initial concentration of the tracer in the estuary was set to 1. The black isolines in these panels depict the thickness of plume in m calculated on 0.1 tracer isoline. Vertical velocity at the lower boundary of the plume (on the surface 0.1 passive tracer isoline) at $t = 5$ h (panel c) and at $t = 3$ h (panel d).

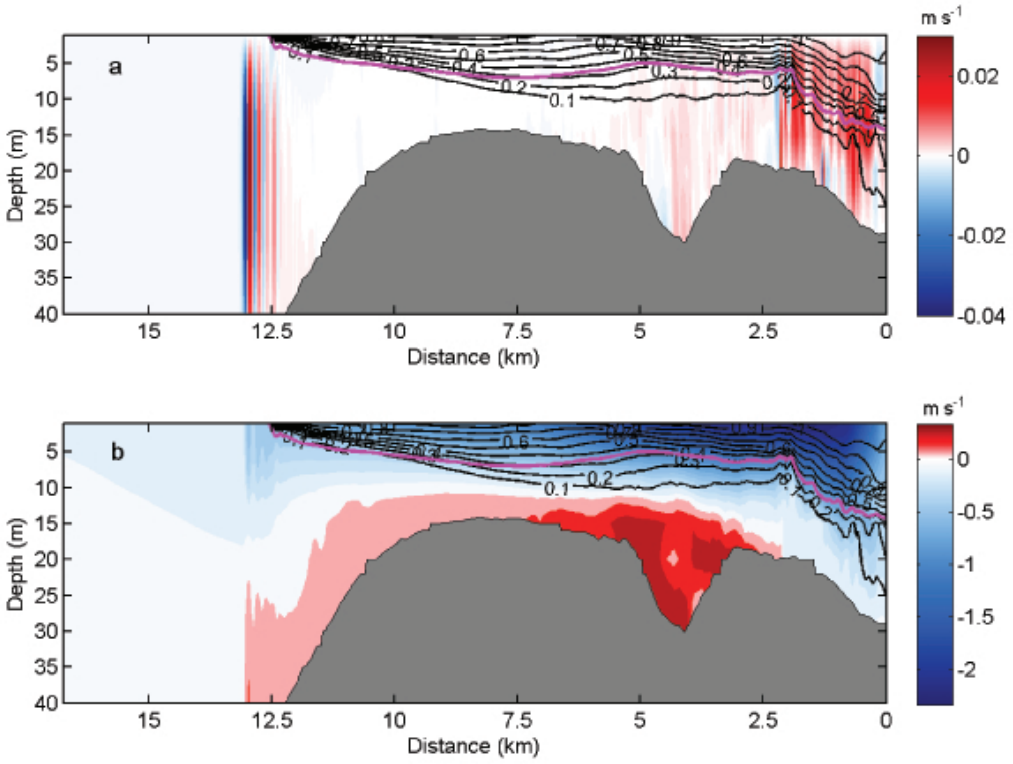

Figure 5.19: Vertical cross section of horizontal (panel a) and vertical (panel b) velocities through the centre of the plume (section a-a in Figures 5.6) (coloured) overlaid with the passive tracer field shown as black solid isolines. Red solid lines in both panels shows the position of isopycnal of density $\sigma_t = 14$ kg m^{-3}.

of blue and red colours, and thus it confirms the presence of internal waves here. The large distance between the $C = 0.1$ tracer isoline and the isopycnal $\sigma_t = 14$ kg m^{-3} in the middle of the plume testifies to great vertical salt fluxes from the sea water penetrating into the plume, which suggests entrainment is taking place.

The entrainment tendency of water mixing found in a qualitative analysis can be quantified. Figure 5.20 shows the water volume discharged from the mouth (dashed line) and the volume of the plume calculated on the boundary of $C = 0.1$ of the passive tracer concentration (solid line). These two lines show that the volume of the plume is more than twice as large as the volume discharged from the mouth at all moments of time. That means that the mixing at the interface in the deep provides strong vertical fluxes of salty water, which makes the plume thicker. It is interesting that, by the end of the ebb phase, the rate of change of the total discharged volume is provided only by the river, which is weaker than the tidal forcing (so that the derivative of the dashed line is quite small) whereas the solid line by $t = 6$ h is as steep as during the whole flood phase. In other words, the entrainment is proceeding with the same rate at all stages.

Another curious result from the fine-resolution modelling is the confirmation of the generation of secondary fronts inside the plume predicted by Garvine (1984). It was assumed there that the internal waves generated at the interface between two layers of the river and sea waters should propagate from the lift-off area toward the plume boundary. As soon as these waves reached the front they are reflected back into the interior of the plume, where they are reflected back again. It was further assumed that the waves arrested inside the plume can produce multiple fronts. To justify this idea several patterns of a radially symmetric river plumes were presented in Garvine (1984) and also some other laboratory and field observations were acknowledged. The possibility of generation of secondary fronts within the plume in the Koombana Bay based on the observational data was reported in Luketina and Imberger (1987).

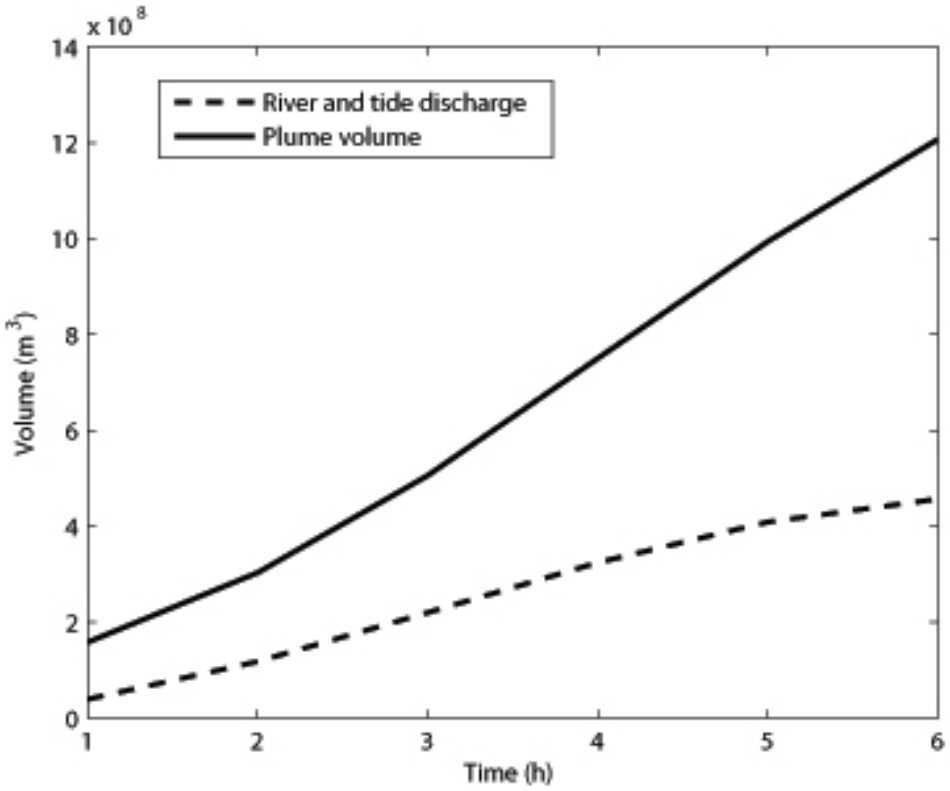

Figure 5.20: The dependencies of the volume discharged from the mouth on time (dashed line) and the volume of the plume calculated on the boundary of 0.1 concentration of the passive tracer (solid line).

Scrutiny of panels c) and d) of Figures 5.18 shows evidence of secondary internal waves generated inside the plume and propagated to the boundary. The propagation of two secondary internal waves from the plume is seen in Figure 5.10. They are marked by 1' solid vertical lines. The reason for their generation is an oscillatory nature of the river discharge, as it was assumed in Luketina and Imberger (1987).

5.5 Horizontal circulation in the plume area

Apart from vertical velocity, Figure 5.19 shows a cross-section of horizontal velocity through the central part of the plume. The red colour in Figure 5.19 b corresponds to the velocity directed into the mouth, and the motions from the mouth are shown in blue. This Figure shows a bi-directional water discharge in one particular section at one particular moment of time, however it does not characterize the whole spatial picture in three dimensions.

Horizontal circulation in the moving Columbia River Plume was analysed in McCabe et al. (2008) using the data on the drifter tracks released near the mouth at the time of the maximum ebb current. The summary of this analysis is given in Figure 5.21, where the trajectories of five drifters during a half of tidal cycle are shown. It is clear that the circulation pattern during the ebb phase resembles characteristics of a radial spreading during the time span $t = 0 - 2$ h (time moment $t = 0$ h in Figure 5.21 corresponds to $t = 3$ h of the model runs). When the ebb flow weakens and is replaced by the flooding flow the drifters start to bend from their initially straight trajectories. After making a U-turn to the right, three northern drifters propagate shoreward. Two other southern drifters reveal similar behaviour, but with an opposite U-turn to the left. Figure 5.21 shows that the major part of the plume water turned to the north due to the Coriolis effect.

Note that the Lagrange drifters released on the free surface can not reproduce a complex three-dimensional circulation, in particular to answer the question how saline

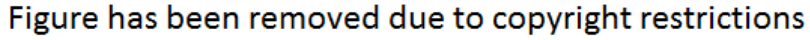

Figure 5.21: Drifter tracks released on the greater ebb near the mouth of the Columbia River (taken from McCabe et al. (2008)). White lines show time contours after the drifter release.

ocean water enters the estuary. To investigate the water circulation in more detail, a cluster of drifters was implemented into the model. Technically, the drifters were initialized in the MITgcm using an extra passive tracer transport equation with the delta-function distributions of the tracer in the appropriate locations at $t = 0$ h. It is clear that the tracer concentration changes over time due to advection and diffusion. The new position of the drifter was calculated as the coordinates of the maximum concentration of the tracer patch. With low values for horizontal and vertical diffusion coefficients used in the tracer transport equation, it was possible to accurately detect the drifter positions every ten minutes for eight hours.

Thus, the methodology of the drifter experiment here was somewhat different to that used in McCabe et al. (2008). In order to achieve a larger coverage, the number of drifters was increased from 5 to 27. Their initial positions were arranged in the nodes of a rectangular grid as shown in Figure 5.22. Nine drifters were released in the surface layer, 9 drifters at the depth of 5 m, and 9 drifters were located in the layer at 8 m depth.

A good agreement between the model predicted trajectories of the surface drifter shown in Figure 5.22 a with the observational drifter tracks presented in Figure 5.21 is clearly seen. After travelling quite a long way offshore, all centrally located drifters ultimately turned to the right due to the Coriolis force. At the latest stages of the

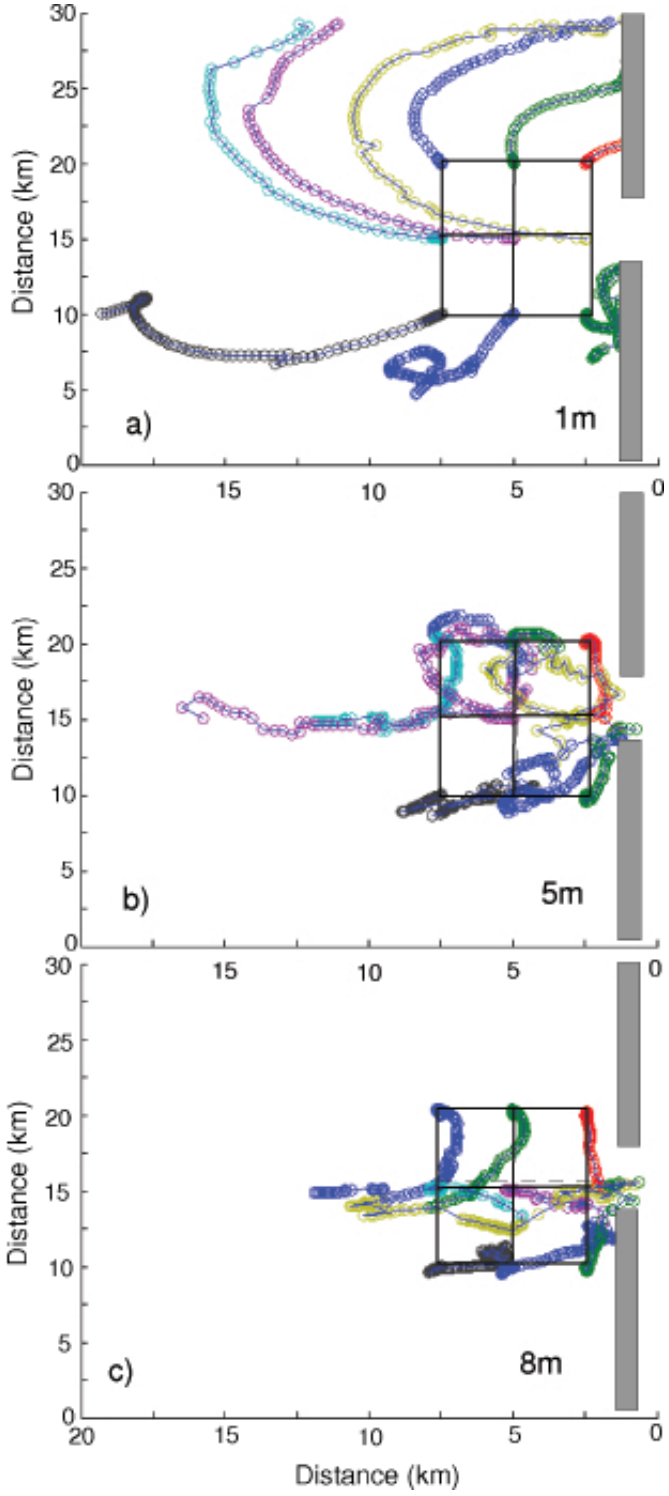

Figure 5.22: Model predicted tracks of drifters released on the beginning of the ebb tidal phase in 9 points near the mouth at 1 m (a), 5 m (b), and 8 m (c) depths. The position of the drifters were marked at 10 minute time intervals.

experiment, when the ebb flow reversed to the flood, the drifters propagated shoreward in the north-eastern direction. Three northernmost drifters were initially located at the periphery of ebb current, Figure 5.22 a. As a result, they were not advected offshore, but moved mainly to the north and north-east approaching the shore line. Two southern drifters travelled similarly to in-situ drifters, especially at the first stage of motion, radially moving away from the mouth in the south-western direction. At the latest stage of tidal phase, they almost stopped and completed a small-scale circulation when the tidal flow in the mouth reversed. Similar drifter behaviour can be found for one of the southern drifters released in the field experiment (see Figure 5.21). The drifter that was initially closest to the mouth (green circles) migrated near the point where it was released being trapped by the near-shore eddy.

The field experiment with the drifters reported in McCabe et al. (2008) allowed one to describe the surface circulation in the progressing river plume. As it is clear from the comparison analysis here, the model reproduces these dynamics quite accurately. If so, one can expect that two other clusters of drifters released in the model at 5 m and at 8 m depth, can also reconstruct the patterns of real circulation. Figure 5.22 b shows the tracks of the drifters released at the depth of 5 m. It is clear that, at this depth, horizontal motions are weaker than in the surface layer. Only two central drifters, the most remote from the mouth, were strongly advected offshore, whereas all others rotated locally slowly migrating to the mouth.

The deepest drifter trajectories (depth 8 m) are shown in Figure 5.22 c. Here, two northern remote drifters and one central drifter were arrested and propagated with the offshore directed jet far from the mouth. On the contrary, all other drifters, migrated to the mouth. One should mention that drifter trajectories were not smoothed but eroded by chaotic pulsations within the plume jet.

Figure 5.23 summarizes the horizontal circulation around the moving plume found with the help of the drifter experiment. This schematic diagram shows a mostly offshore

water transport in the surface layer with a predominant tendency to follow the northern route. At the lower boundary a return current replaces the waters being moved offshore.

5.6 Summary remarks on the near-field dynamics

The mechanism of generation of internal waves by the moving Columbia River plume in its transition from supercritical to sub-critical regimes of propagation (previously reported in observations Nash and Moum (2005), and reproduced numerically in Stashchuk and Vlasenko (2009)), was investigated for a longer time period and in a larger model domain. It was found that not only first-mode, but also second and third mode internal wave packets can be radiated from the plume, when the velocity of the front propagation drops below the phase speed of an appropriate internal baroclinic mode. In other words, the mechanism of internal wave radiation discussed previously in Nash and Moum (2005) and Stashchuk and Vlasenko (2009) for only first-mode wave packets, is realised here for higher baroclinic modes.

In terms of possible impact on the marine environment (internal mixing, for instance) these high mode waves can have an effect comparable with the first-mode counterparts. The reason for that is their specific vertical structure, which suggests strongest shear of horizontal velocities beyond the pycnocline layer. In fact, strong stratification in the layer of density interface stabilizes vertical velocity shear induced by the first-mode waves. However, as it was shown by Pan and Jay (2009*b*), any kind of perturbation of vertical structure of internal waves which lead to a displacement of the eigen function extremums from the pycnocline layer can greatly facilitate mixing processes. The model output shows that the amplitude of these high mode waves are of the same order as the leading first-mode waves, which in combination with the upward shear shift creates favourable conditions for the generation of shear instability.

Thanks to the choice of a fine-resolution grid the details of the internal structure of the Columbia River plume were reproduced by the model accurately. This structure

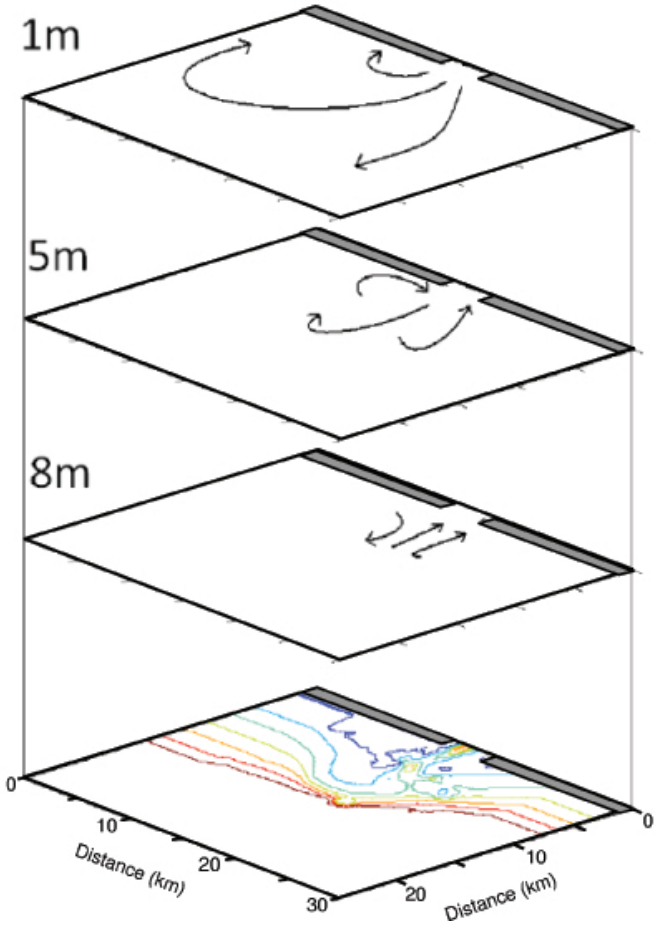

Figure 5.23: Schematic diagram showing the horizontal circulation in the moving plume based on the drifter tracks analysis.

shows evidence of secondary fronts inside the Columbia River plume, which were not captured by other models. The systems of secondary internal waves propagated radially from the lift-off area to the outer boundary, were they are arrested, are also clearly seen. The possibility of the existence of such a fine structure within the moving plume was pointed out in the theoretical paper Garvine (1984), and this fact was confirmed later in the observational paper Luketina and Imberger (1987)for the Koombana Bay.

Another outcome from the present study is that the MITgcm allowed for the quantification of the mixing processes within the propagating Columbia River plume and to confirm the predominance of the entrainment mechanism developing on the lower boundary between the plume's body and surrounding waters. This conclusion was made on the basis of the drifter data reported in McCabe et al. (2009), and here on the basis of model output.

Previous modelling investigations into the Columbia River plume have largely used coarser resolution grids and hydrostatic models. The use of MITgcm with a hydrostatic assumption as well as the fully non-hydrostatic mode allowed a comparison to be made, which identified the use of fully non-hydrostatic equations as crucial to accurately reproducing the generation and structure of internal waves by the plume. It is also shown, however, that when considering the near-field spreading of the plume, there is little difference between the two cases and that the hydrostatic assumption is acceptable for investigations that do not aim to reproduce the internal waves but only the general plume structure.

The drifter methodology was applied in the present study in order to reproduce the horizontal circulation within the moving Columbia River plume. In doing so, 27 Lagrangian drifters were released in the model at depths 1, 5 and 8 m near the mouth which allowed the drifter tracks to be drawn and to picture the horizontal circulation in different parts of the Columbia River plume. It showed mostly offshore water transport in the surface layer in the near-field (close to the mouth) with predominantly northward

water transport in the far field due to the Coriolis force. In the deeper layers of the plume, at the levels close to its lower boundary, the water transport in the central part is mostly from the mouth with some return currents at the plume's periphery.

5. VERTICAL STRUCTURE AND WATER MIXING PRODUCED BY A MOVING PLUME NEAR A RIVER MOUTH

Chapter 6

Large-scale dynamics of the Columbia River plume under the action of long-term wind forcing

This chapter describes the investigations into the far-field plume. The effect of wind forcing on the plume is explained and how this affects nutrient distribution in the region.

6.1 Introduction: Wind-driven motions

In the previous chapter, the near-field evolution of the Columbia River plume because of river inflow, tides and density gradient between the estuary and sea was considered. Another important forcing that influences the propagation of plume waters is wind. Wind movements at the ocean atmosphere interface imparts energy and momentum to the upper ocean generating waves and ocean currents (Pond and Pickard, 1983). Wind stress is the dominant forcing to much of the surface ocean, increasing mixing and breaking down stratification. It is therefore important to include wind forcing when modelling surface processes, such as buoyant plume dispersion. In this chapter results of experimental runs with idealised and realistic wind forcing are presented.

6.1.1 Wind-driven circulation in an infinite basin

When considering wind driven motions, it is important to include an analysis of Ekman transport, which describes the movement of water due to the transfer of momentum from the wind in a simplified system. Ekman assumed a basin that has no lateral boundaries and that is infinitely deep so water movements are not constrained and

bottom friction is neglected. To further simplify the situation, eddy viscosity, A_z, is assumed to be constant with depth. Ekman also assumed a steady wind, which has been blowing for a long time, barotropic conditions so that there is no geostrophic flow and the f-plane approximation was made. These assumptions in the horizontal momentum equations give rise to the Ekman equations,

$$fv_E + A_z \frac{\partial^2 u_E}{\partial z^2} = 0 \tag{6.1}$$

$$-fu_E + A_z \frac{\partial^2 v_E}{\partial z^2} = 0 \tag{6.2}$$

showing that Coriolis is balanced by friction. By considering a wind blowing in the y direction, the Ekman transport in the u and v direction becomes,

$$u_E = \pm V_0 \cos\left(\frac{\pi}{4} + \frac{\pi}{D_E} z\right) \exp\left(\frac{\pi}{D_E} z\right) \tag{6.3}$$

$$v_E = V_0 \sin\left(\frac{\pi}{4} + \frac{\pi}{D_E} z\right) \exp\left(\frac{\pi}{D_E} z\right) \tag{6.4}$$

+ in the northern hemisphere, - in southern hemisphere, and where the total Ekman surface current is,

$$V_0 = \frac{(2\pi\tau_{y\eta})^{1/2}}{D_E \rho |f|} \tag{6.5}$$

and $\tau_{y\eta}$ is the wind stress at the sea surface, and the Ekman depth is,

$$D_E = \pi \left(\frac{2A_z}{|f|}\right)^{1/2} \tag{6.6}$$

Solving 6.4 at the sea surface (z=0) we obtain,

$$u = \pm V_0 \cos 45^o, v = V_0 \sin 45^o \tag{6.7}$$

so for the northern hemisphere the current is offset by 45^o to the wind direction. As depth increases, current speed reduces and the offset angle increases giving rise to the Ekman spiral (Figure 6.1) and the net Ekman transport is 90^o to the right of the wind direction (in northern hemisphere).

Figure has been removed due to copyright restrictions

Figure 6.1: An illustration of the changing current direction and strength as depth increases forming the Ekman spiral, from Garrison (1993)

6.1.2 Wind-driven circulation near the coast

The effect of the wind in an infinite basin with simplifications as described above shows a net movement of water in the Ekman layer to be 90^o to the right of wind direction in the northern hemisphere. The displaced waters in that case are replaced by surface waters to the left of the wind direction. When a coastline prevents adjacent surface waters from replacing those advected by wind forcing, water from depth is upwelled to the surface (Figure 3.7). In the case where the coast prevents the advected waters from moving away horizontally, waters are down-welled.

6.1.3 Wind effect on buoyant surface plumes

In the absence of any wind and the currents that they produce, a buoyant surface plume may form an expanding bulge near the mouth and a thin coastal current travelling along the coast to the right in the Northern hemisphere (Fong and Geyer, 2002). This scenario is not often observed in nature and seems to be a feature produced in simplified models and experiments (Yankovsky, 2000). Wind forcing can have a great impact on the large-scale dynamics of river plumes as momentum is trapped within the thin plume due to a strong density gradient with the ambient water. As a result, buoyant plumes can be significantly influenced by moderate winds (Lentz, 2012). Alongshore winds advect the plume front offshore or onshore due to Ekman dynamics as theorised by Csanady (1978) and observed by Fiedler and Laurs (1990) and Munchow and Garvine

(1993). Previous modelling studies including those by Chao (1988) and Kourafalou et al. (1996*a*) have reproduced these effects. As well as directly advecting the plume waters, the effect of upwelling favourable winds is to thin the plume (Figure 6.2 a) and increase mixing (Masse and Murthy, 1992; Souza and Simpson, 1997; Fong and Geyer, 2001). Downwelling winds also increase mixing because of increased shear and advect the plume away from the river mouth. The plume waters are transported onshore during downwelling winds and transport alongshore is greatly increased. The stratification at the plume front is reduced as the front steepens and the plume thickens (Figure 6.2 b). The task addressed in this chapter is to use MITgcm to recreate a large-scale wind forced plume and induce upwelling and downwelling within the model and to improve upon the previous findings of Garcia Berdeal et al. (2002), by including realistic topography and providing stratification to the coastal ocean. A higher resolution grid will also be used compared to their 1.5 km $\times$ 2 km grid.

6.1.4 Wind of the Columbia river plume region

Seasonal wind-driven processes govern the water properties of the Columbia River plume. This seasonal cycle is causes by alternating atmospheric pressure systems over the North Pacific. In summer, the winds are generally moderate and blow steadily from the north because of the the North Pacific High. In winter, winds are predominantly from the south due to the Aleutian low (Barnes et al., 1972; Hickey, 1989). Additional to these seasonal means, $2-10$ day fluctuations in wind strength are observed (Hickey, 1989), typically in the direction of the seasonal mean (winter - downwelling favourable, summer - upwelling favourable) and with magnitudes from 0.5 dyne cm^{-2} up to 5 dyne cm^{-2} during severe storms. The summer fluctuations in either direction tend to be $\approx$0.5 dyne cm^{-2} in strength with the majority of storms being during winter months (Hickey, 1989). The position of the Columbia River plume is also seasonal, as seen in both satellite data (Fiedler and Laurs, 1990) and in-situ data (Hickey et al., 1998).

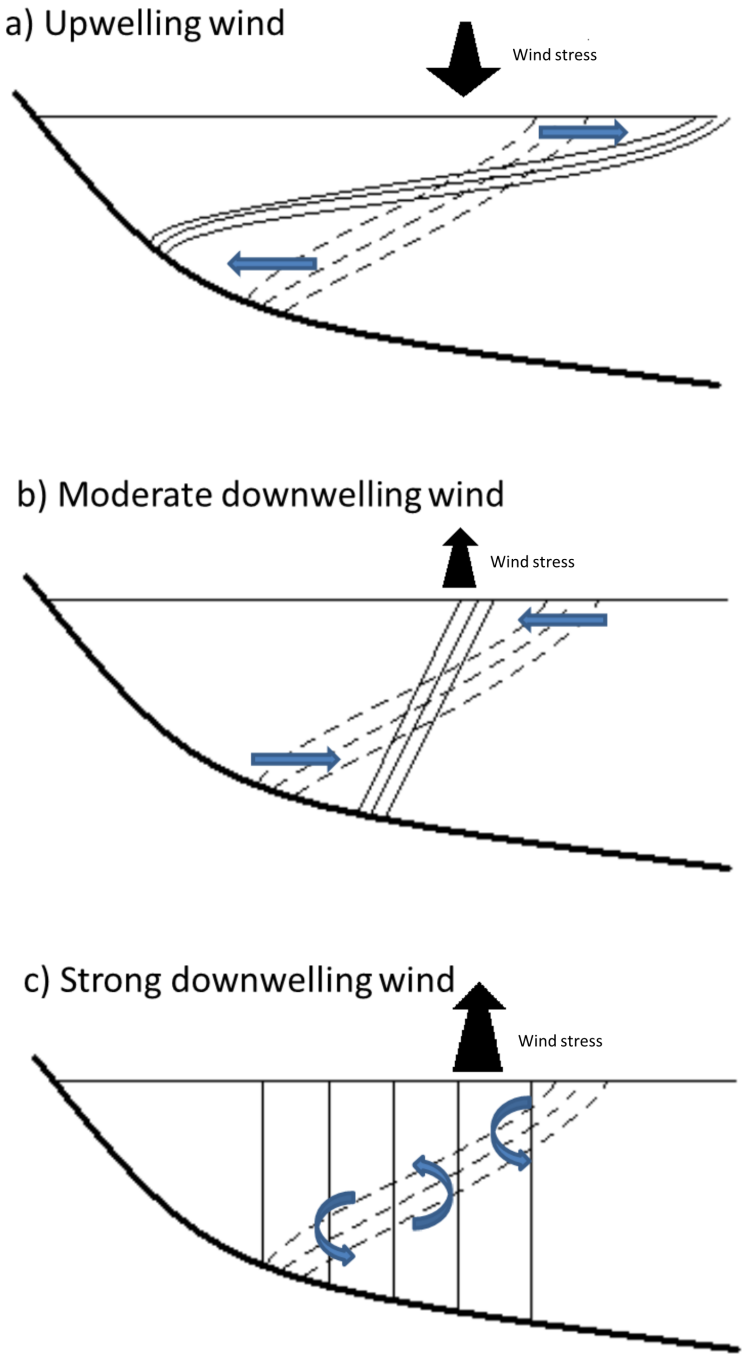

Figure 6.2: Schematic of buoyant plume response to different along shelf wind forcing. a) Upwelling winds flatten the plume front, causing the plume to thicken and widen. b) Moderate downwelling winds steepen the front, causing the plume to thicken and narrow. c)Strong downwelling winds force vertical mixing that widens the plume front but causes little change in the plume width. *After* Lentz (2012)

During summer months the prevailing southward wind results in a plume located to the south-west of the river mouth. After the transition to northward winter winds, the plume is observed to be north of the river mouth.

6.2 River Influences on Shelf Ecosystem (RISE) program

It is clear that water mass properties, nutrients, biomass and currents are strongly influenced by wind-driven processes. The River Influences on Shelf Ecosystem (RISE) program was a 5 year interdisciplinary study, including observations and modelling studies. It focused on the influence of the Columbia River plume on the regional productivity of coastal waters off Oregon (to the south of the Columbia River) and Washington (to the north), Figure 6.3.

One of the goals of the program was to explain the observation that phytoplankton biomass is generally higher off Washington than Oregon. This situation is counter-intuitive as upwelling favourable wind stress increases towards Oregon and the south (Banas et al., 2009).

6.2.1 RISE field studies

The RISE field program consisted of 5 cruises in July 2004, June 2005, August 2005 and June 2006. Each cruise was undertaken by two vessels, the RV Sur (plume surveys, mixing processes and zooplankton dynamics) and the RV Wecoma (biological and chemical studies), Figure 6.3. A pre-RISE cruise took place from 27^{th} June to 2^{nd} July 2004 by the RV Point Sur. Both vessels then undertook the cruises RISE-1 from 8^{th} to 28^{th} July 2004, RISE-2 from 29^{th} May to 21^{st} June 2005, RISE-3 from 4^{th} to 26^{th} August 2005 and RISE-4 from 21^{st} May to 13^{th} June 2006 (Bruland et al., 2008). The data collected during the RISE-3 cruise are considered in this chapter as it took place during a period of relativley stable wind conditions.

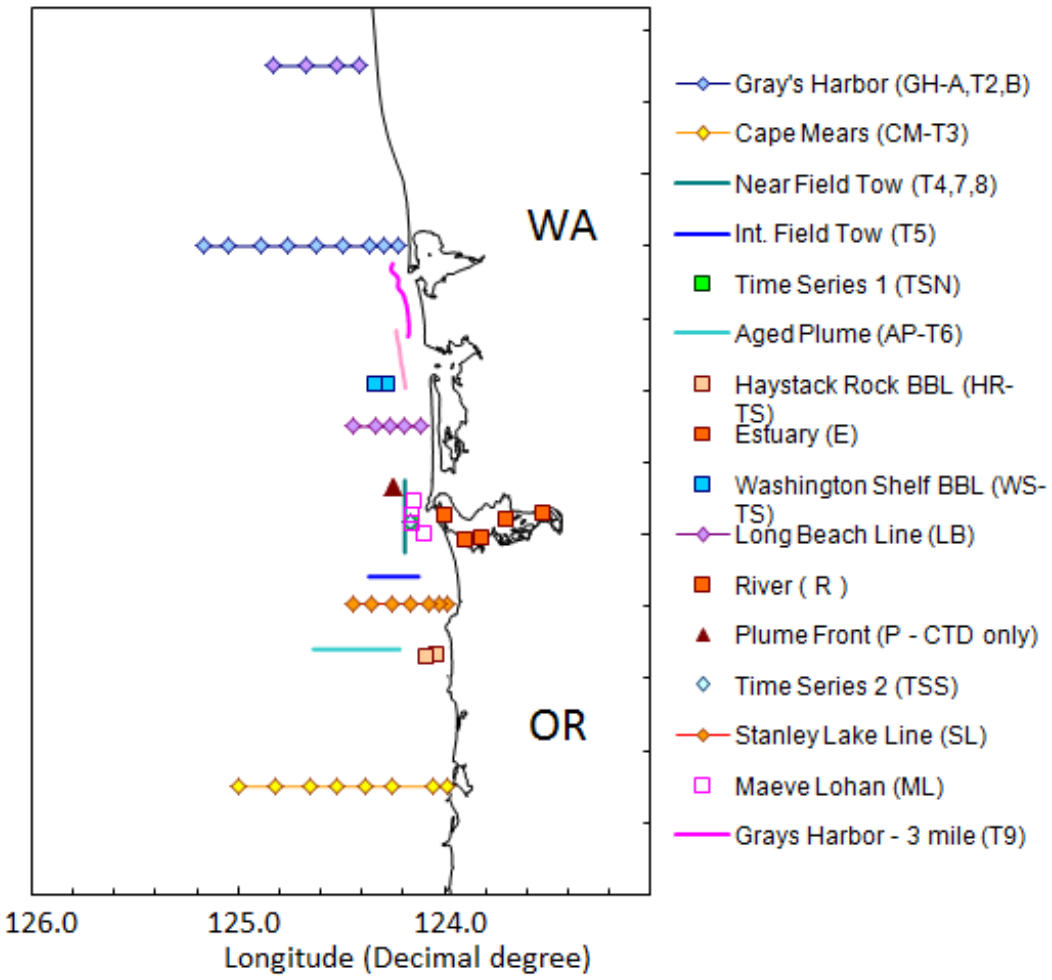

Figure 6.3: Location of data collection sites during the August 2005 cruise

6.2.2 RISE modelling studies

As part of the RISE project, two modelling strategies were used to plan sampling strategy and analyse in situ data. The models used were the Regional Ocean Modelling System (ROMS) (as described in Shchepetkin and McWilliams (2003) and Shchepetkin and McWilliams (2005)) and the CORIE/SATURN modelling system. The CORIE/SATURN system is comprised of the Semi-implicit Eulerian-Lagrangian Finite Element (SELFE) model (Zhang and Baptista, 2008) and Eulerian-Lagrangian CIRCulation (ELCIRC) model (Zhang et al., 2004). The widely used ROMS model is a terrain following, free surface, hydrostatic, primitive equation model. The investigations used a horizontal resolution of 400 m in the near-field and up to 7 km near the boundaries. SELFE is a finite element model with an unstructured horizontal grid and a hybrid SZ vertical grid. ELCIRC also uses an unstructured horizontal grid with a finite volume/finite difference Eulerian-Lagrangian algorithm. SELFE/ELCIRC was used for modelling near plume processes and had horizontal resolutions of 150 m in the estuary increasing to 1 km in the near plume area and up to 20 km at the boundaries. These investigations produced varying results, that were unable to completely reproduce an accurate plume structure (Hickey et al., 2010). In an attempt to build on the RISE modelling results, a series of large scale modelling investigations are developed here.

6.3 Idealised experiment

The observations that were obtained during the August 2005 RISE cruise are used for this analysis. Wind directions and velocities at a buoy located just offshore of the Columbia River mouth are shown in Figure 6.4. The negative direction on the plot corresponds to equatorward, upwelling favourable winds, while the winds in the positive direction are poleward,downwelling favourable. It was found that the mean velocity of

wind events is 6 m s^{-1}. In order to develop a reliable model that utilises realistic wind forcing, it is first necessary to make some preliminary investigations. The large-scale models response to wind forcing is first tested in a series of model runs with a simplified constant surface wind speed (6 m s^{-1}). Initially, an investigation into the effect of a constant alongshore wind on plume distribution was undertaken. It was expected that there would be great differences in plume distribution with a constant northerly and southerly wind in line with the findings of a modelling study by Chao (1988), in which downwelling favourable winds would enhance the transport of plume water along the coastal jet, whereas upwelling favourable winds that oppose the jet would act to move the plume further off-shore as seen in Figure 6.2. This effect of upwelling winds has also been observed in the Gulf on Maine by Fong et al. (1997) and for the Columbia River plume in Hickey et al. (1998) .

6.3.1 Model set up for idealised experiment

The large scale model domain corresponds to an area which was sampled during the RISE project data collection phase. The model domain was varied depending on wind conditions used, but a horizontal grid spacing of 500 m was maintained. Realistic bathymetry was used along with a simplified estuary in order to recreate estuarine re-circulation. Vertical resolution was 1 m for the first 6 surface levels then 1.5, 2, 2.5, 3, 5, 10, 10, 20, 20, 20, 50, 50 m. Since MITgcm uses a z vertical coordinate system, this high surface resolution was maintained over the entire domain. The topography was limited to 200 m, because below this depth, conditions remain similar and also few measurements were taken below this depth. The time-step used to maintain stability was 1 minute and typical runs simulated a one month period. The shelf waters were initiated with a uniform stratification throughout the domain based on measurements taken during the RISE cruise of August 2005. MITgcm allows wind forcing to be prescribed in the form of 2-dimensional zonal and meridional wind stress files, which

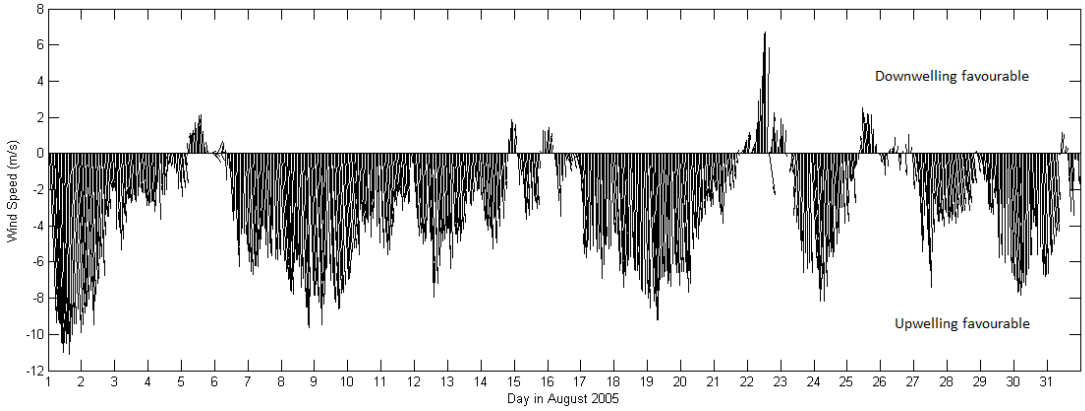

Figure 6.4: Wind velocity measurements for August 2005 taken at Buoy 46029, in the region of the Columbia River plume

were set every hour. A spatially uniform wind field is justified because weather systems in the region are often of a similar scale to the model domain.

6.3.2 Northerly wind (upwelling favourable)

For the case of northerly wind, a constant stress of 0.05 N m^2 equivalent to a 6.1 m s^{-1} wind blowing from north to south was applied to the domain from the first time step. It was expected that there would be an initial period, in which inertial oscillations dominate. This can be seen in Figure 6.5. The top plot shows the model domain with the point where the velocities were taken. The bottom two plots show horizontal velocities at a range of depths for the first 400 hours of the northerly wind run. There were initially large oscillations which have a period close to the inertial period of the region given by $T_{sd}/(2\sin\phi) \approx 16.6$ hours, where $T_{sd} \approx 24$ hours and $\phi \approx 46.2$ degrees. There is a relaxation period of approximately 5 days, during which the amplitude of these inertial oscillations decrease and after 10 days a steady M2 tidal oscillation has established with a period of approximately 12.5 hours and the inertial oscillations were no longer detectable. These results show that after an initial 10 day period the effect of wind stress can be considered reliable and that future runs should include a period

of spin-up to account for this.

An analysis of vertical velocity structure shows that, in the case of the constant northerly wind, a clear Ekman spiral is present (Figure 6.5 b) with surface water travelling in a south-westerly direction. The net transport of water is then expected to be in an offshore direction, which, according to theory should induce upwelling. This has the effect of drawing the plume waters offshore and with each tidal period a lens of plume water is advected away from the coast. This process is shown in Figure 6.6, a series of plots over a tidal period that show and initial plume bulge being formed on an ebb tide and spreading southwards. There are still waters near the river mouth that turn to the north due to Coriolis but they are restricted to a small bulge of the main plume. These figures also show increased salinity at the coast due to the upwelling of more saline deep water. Figure 6.7 shows the evolution of this plume emergence in cross-section where the presence of upwelled saline water can be clearly seen. It is also shown that the plume has formed a thin lens that stretches far from the shore in line with the theory as described by Lentz (2012).

6.3.3 Southerly wind (downwelling favourable)

For this experiment the model domain was altered to include a larger area to the north (Figure 6.8 a) of the river mouth and wind stress was a constant 0.05 Nm^2 representative of a 6.1 ms^{-1} wind from the south applied to the model immediately. Tidal and discharge forcing remained the same. Similarly to the first experiment as the wind forcing is initiated immediately inertial oscillations are generated (Figure 6.8 c & d) and again the oscillations reduce over time until after approximately 10 days tidal oscillations dominate.

The evolution of the plume is very different compared to the previous experiment. Figure 6.9 shows the plume emerges on the ebb tide and turns immediately to the right becoming a coastally trapped plume. When viewed in cross-section (Figure 6.10) it can

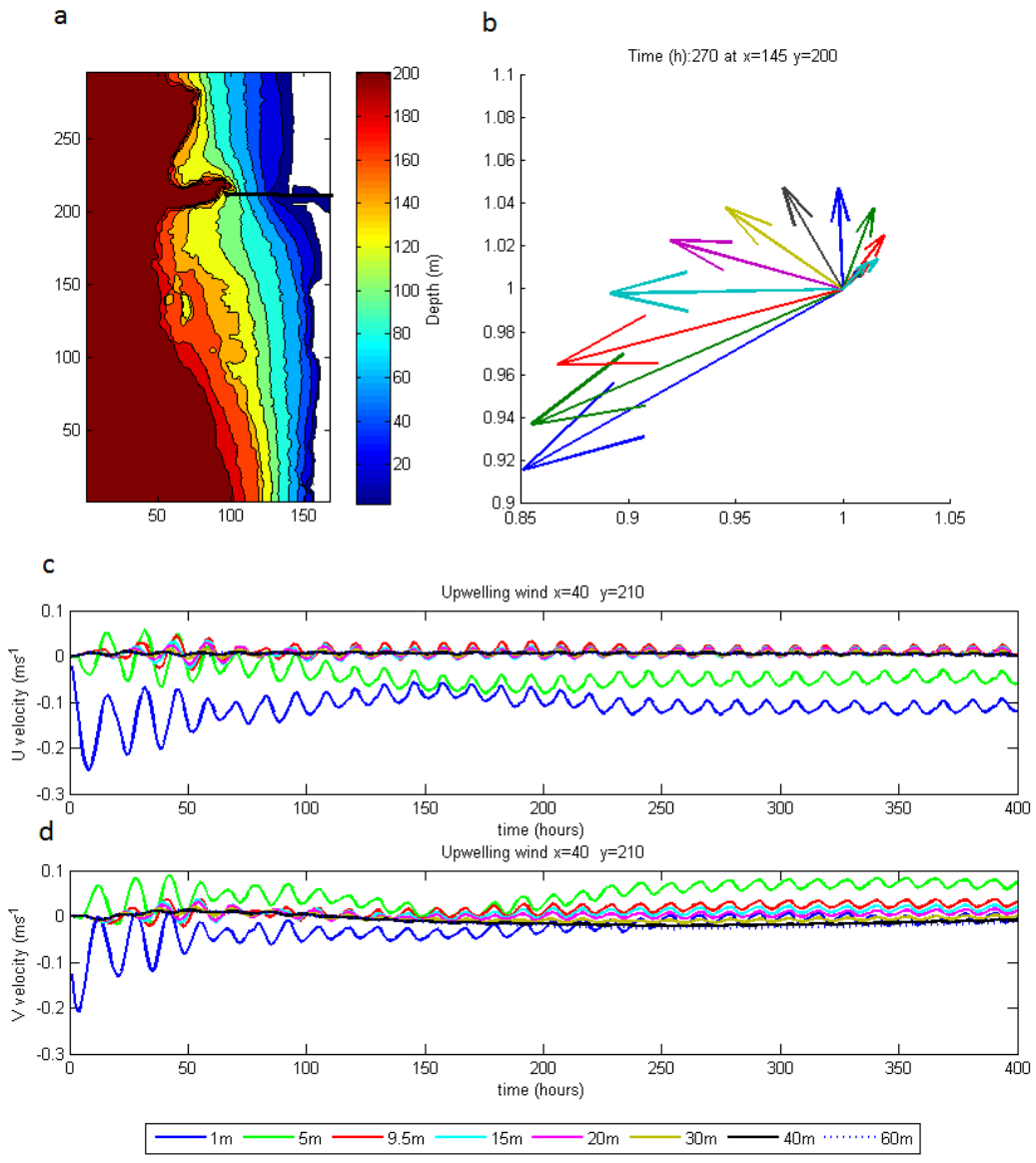

Figure 6.5: Northerly wind domain (a), Ekman transport at point x=145 y=200 (b), inertial oscillations at point x=40 y=210 (c & d)

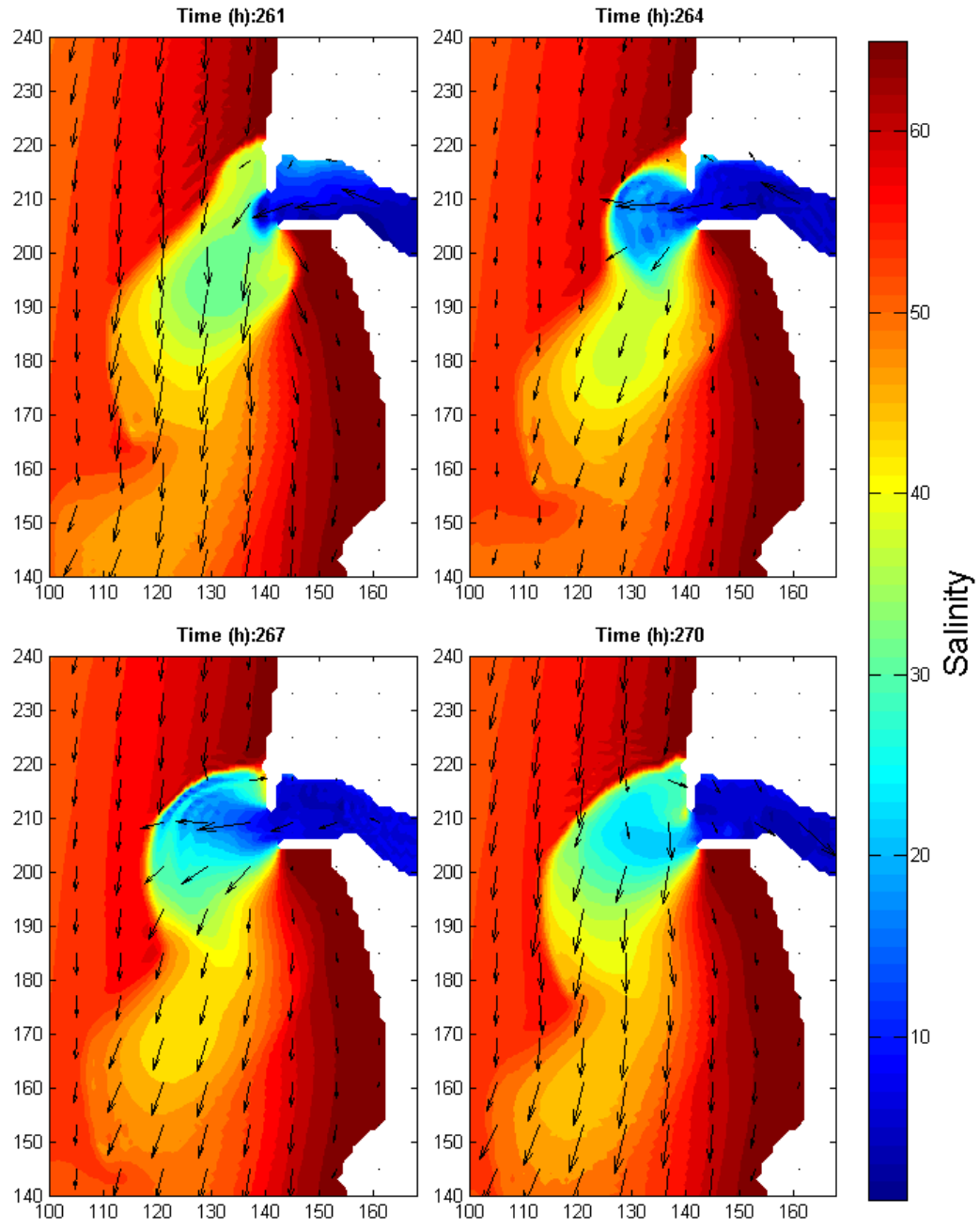

Figure 6.6: Surface salinity plots showing the evolution of the plume under constant northerly wind stress of 0.05 Nm^2 through a tidal cycle. Arrows represent surface velocity vectors

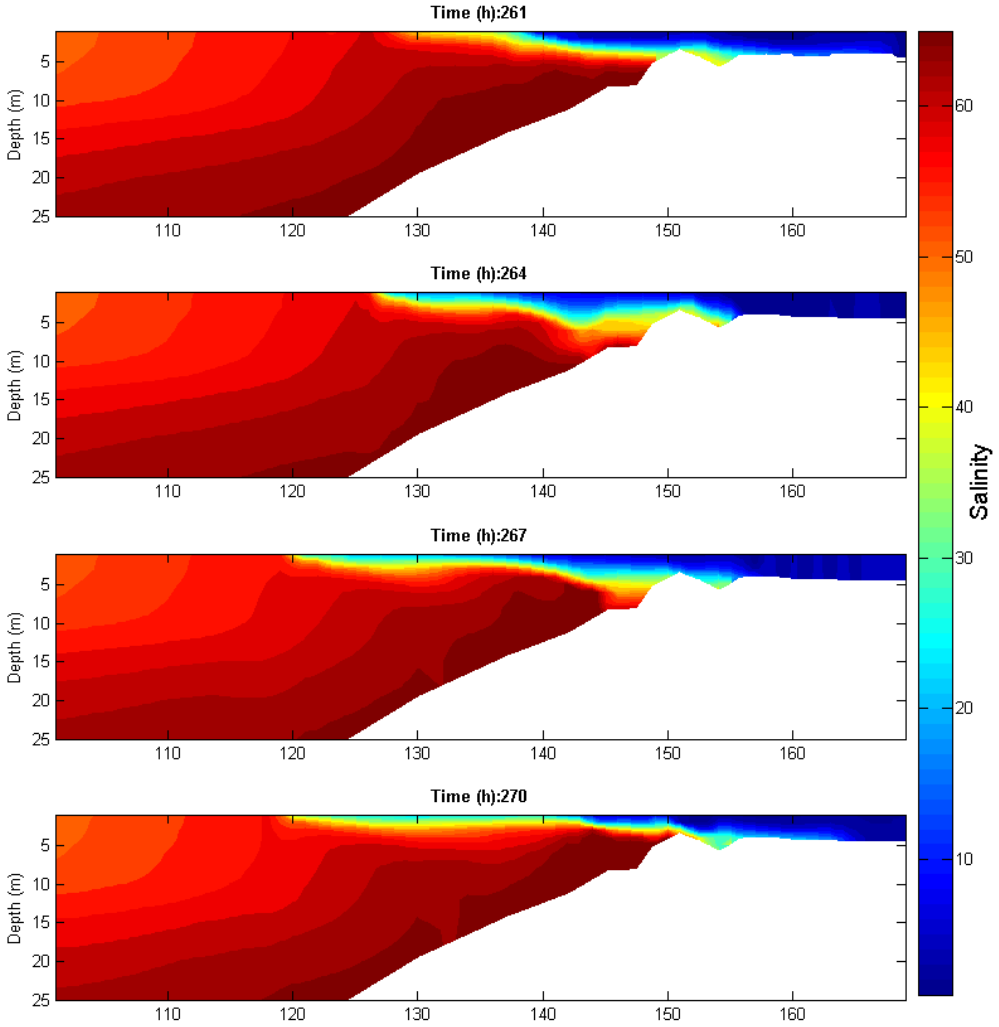

Figure 6.7: Salinity cross-section showing a thin plume being advected away from the coast over time

bee seen that the plume has thickened and isohalines have been displaced downwards as a result of downwelling. It is interesting to note that, when velocities over depth are analysed (Figure 6.8 b), the transport appears to be in a constant north-easterly direction throughout the water column. This is a result of interaction with local topography and the plume thickening in the region.

6.3.4 Differences in plume structure for northerly and southerly winds

According to the results presented in Chapter 5, the river plume that flows in a rotating system without applied winds forms a non-linear "bulge region" where the plume turns to the right (in the northern hemisphere). Thus the Columbia River plume first generates a slowly expanding bulge near the mouth of the estuary, and then the fresh water in the outer part of the bulge flows southward, forced by the upwelling current, resulting in a widening and thinning buoyant plume over the shelf. During the downwelling favourable wind, the plume turns to the north and forms a deep flow along the shoreline.

6.4 Realistic wind scenario

The above cases are a simplifications of the naturally variable winds of the region. In this section, investigations into the response of the plume to realistic wind are analysed.

Whilst the results from the investigations presented so far are in line with theory, to validate the model fully, this section presents a number of comparisons with in-situ data collected during the RISE cruise during August 2005 and with the work of other authors. The RISE cruise of August 2005 consisted of a number of transects along which CTD deployments were made and water samples taken. Figure 6.11 shows the four CTD sampling lines and long term CTD station ML that fall within the model domain and period which are compared to model results. The longitude, latitude and

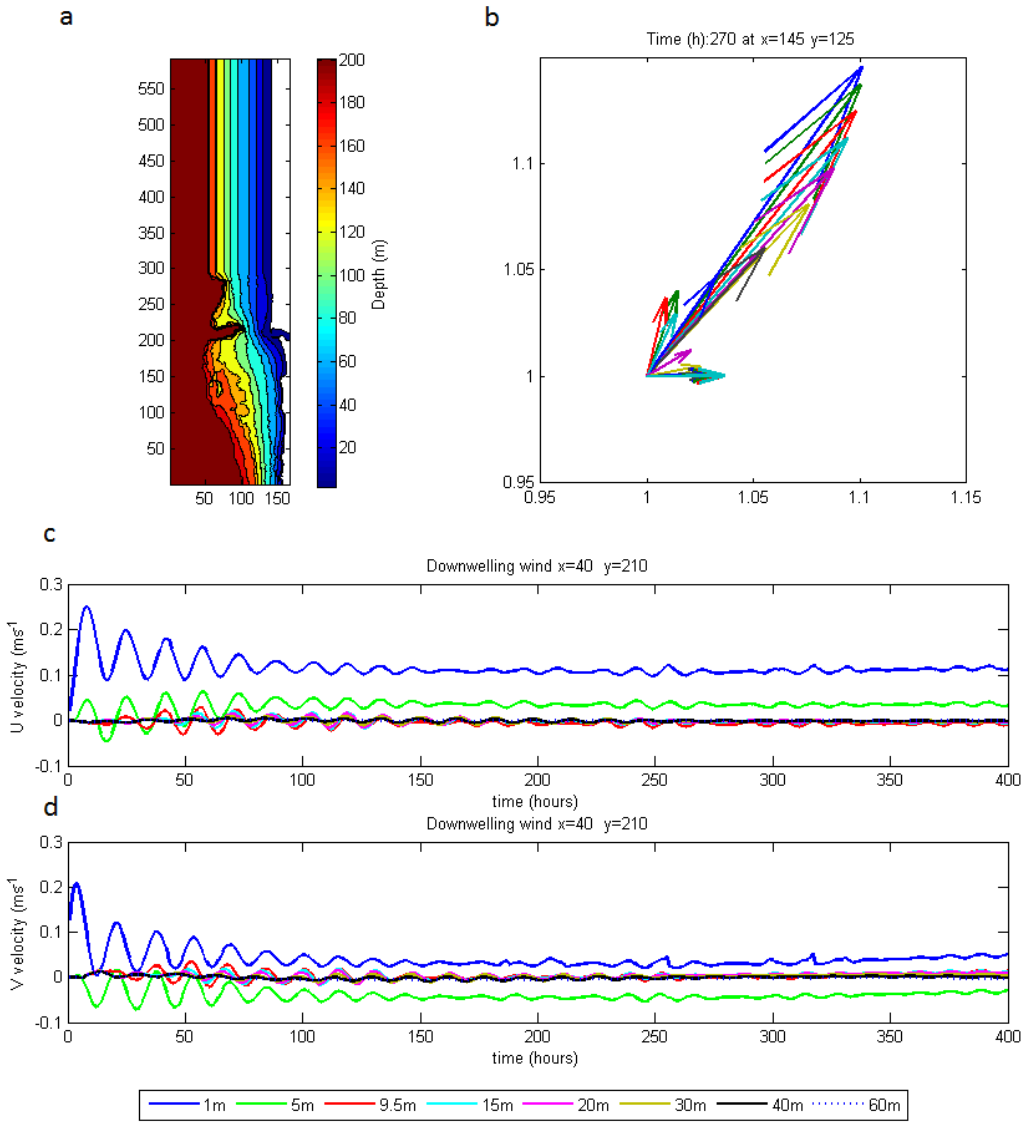

Figure 6.8: Southerly wind domain (a), Ekman transport at point x=145 y=125 (b), inertial oscillations at point x=40 y=210 (c & d)

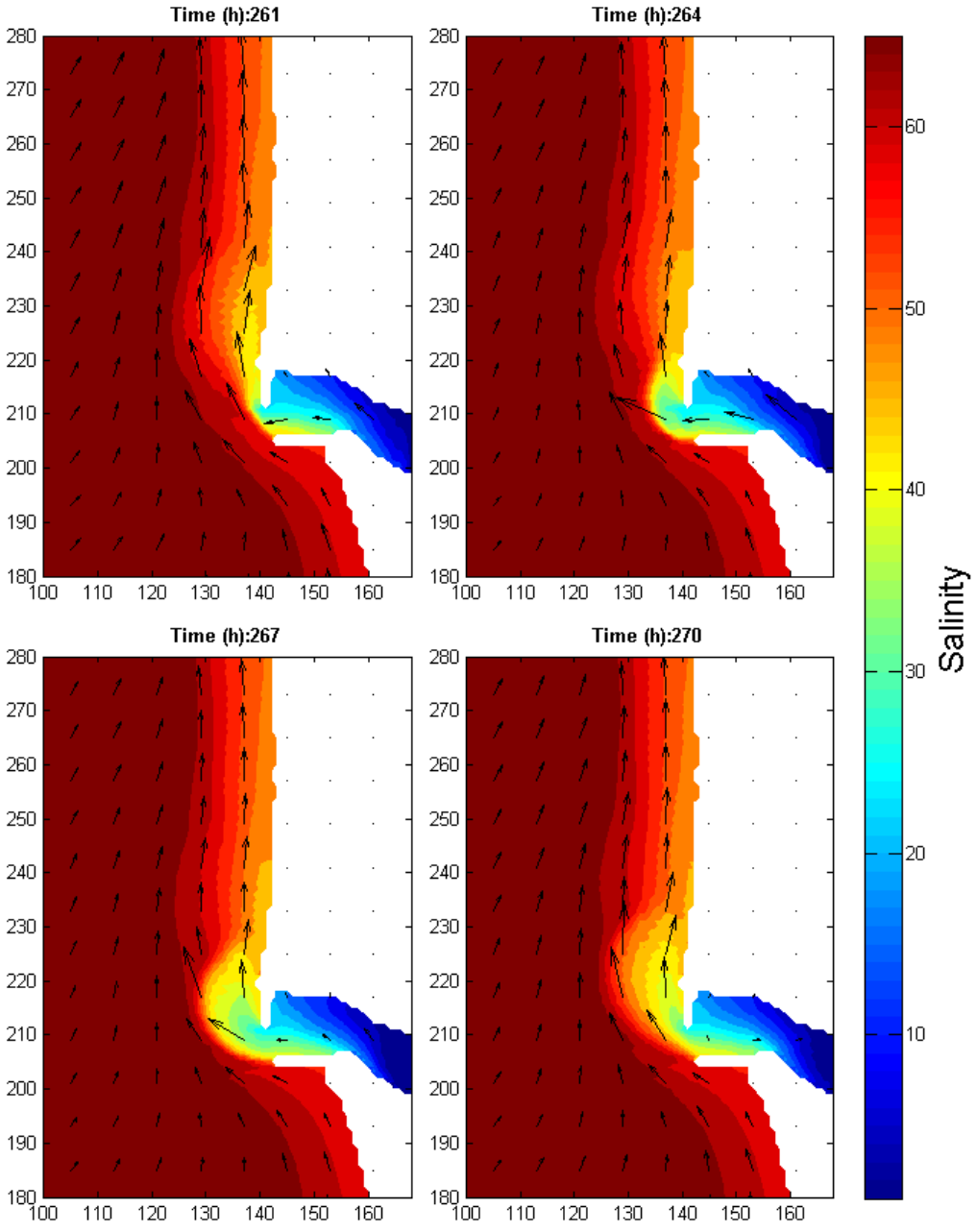

Figure 6.9: Surface salinity plots showing the evolution of the plume under constant southerly wind stress of 0.05 Nm^2 through a tidal cycle. Arrows represent surface velocity vectors

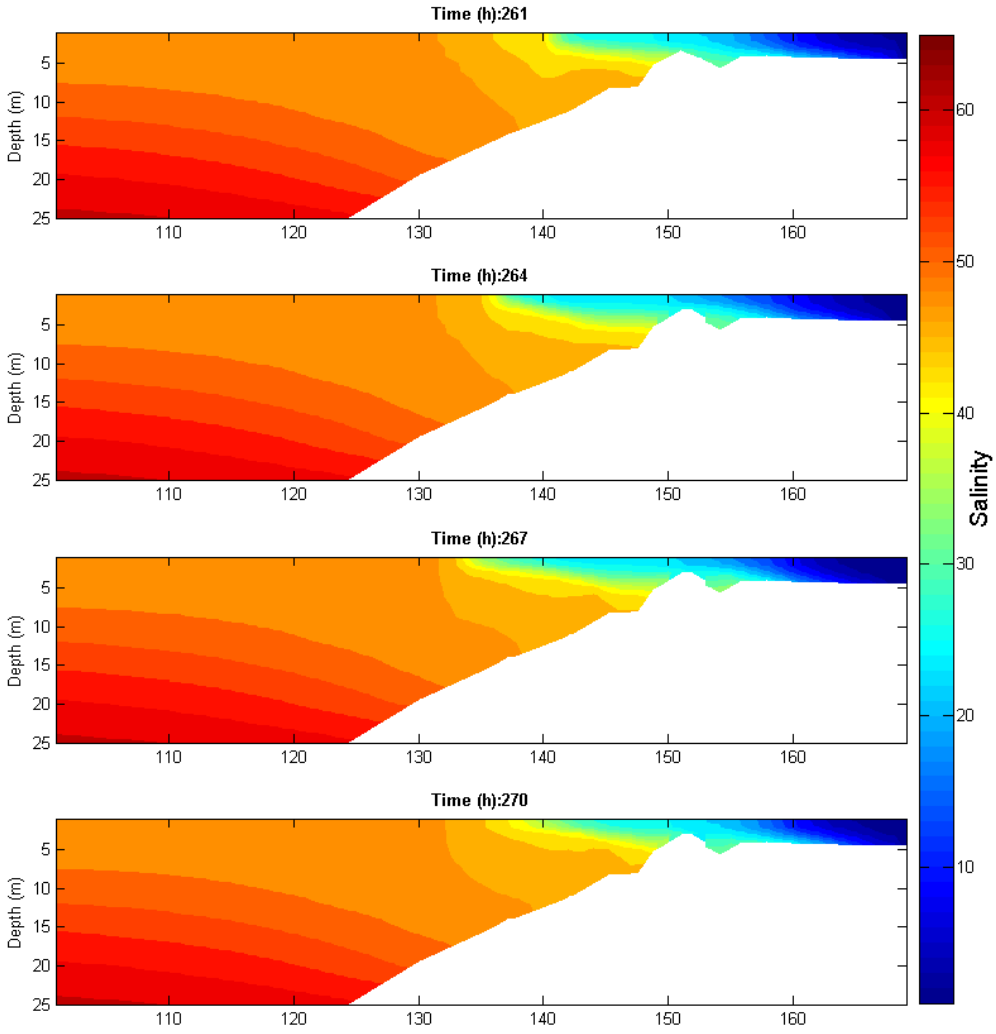

Figure 6.10: Salinity cross-section showing a thick, narrow plume

dates for the sampling lines and point ML are presented in Table 6.1. The lines coincide with the wind events shown by the grey bars in Figure 6.12.

Table 6.1: Locations and timings of RISE CTD lines and station ML

Name	Latitude	Longitude	Date
Line 1	45.50	123.98 to 124.82	7th to 8th
Line 2	46.50	124.27 to 124.44	16th
Line 3	46.00	123.98 to 124.54	21st to 22nd
Line 4	45.50	123.99 to 124.82	25th
ML	46.23	124.17	10th to 11th, 20th to 21st

6.4.1 Model set up for a realistic wind scenario

Hourly in-situ wind speed measurements taken from Buoy 46029, adjacent to the Columbia river mouth, during August 2005 were used to calculate a realistic time varying wind-stress to force the model. The wind direction during this period was predominantly from the north and varied in strength, but did not exceed 10 m s^{-1} as shown in Figure 6.12 a.

To calculate the wind drag coefficient, *Cd*, from the wind speed *U*, the relationship by Yelland and Taylor (1996) was used, which is given as,

$$1000C_{D10m} = 0.29 + \frac{3.1}{U_{10m}} + \frac{7.7}{U_{10m}^2} \tag{6.8}$$

when U is less than 6 m s^{-1} and for U greater than 6 m s^{-1}

$$1000C_{D10m} = 0.6 + 0.007U_{10m} \tag{6.9}$$

From this, the zonal and meridional wind shear stress components are calculated as,

$$\tau_x = C_D \rho u (u^2 + v^2)^{0.5} \tag{6.10}$$

$$\tau_y = C_D \rho v (u^2 + v^2)^{0.5} \tag{6.11}$$

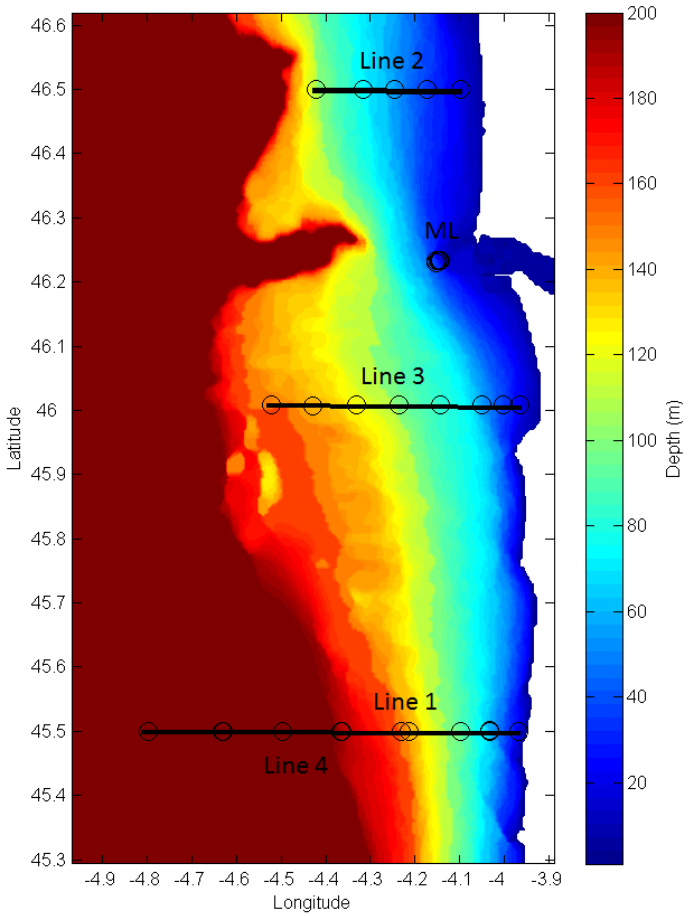

Figure 6.11: Model domain and bathymetry, lines represent RISE transects with stations marked as circles.

where ρ is the density of 15^{o}C air at sea level (1.29 kg m^3) and u and v are the horizontal components of wind speed. For these runs, the model domain was located predominantly to the south of the river mouth as this is where the plume waters are expected to be advected to as a result of the predominantly northerly winds. The bathymetry was limited to 200 m with 18 depth levels similar to the previous experiments shown in Figure 6.11. The plume was forced from the estuarine boundary with time varying velocity representing realistic tidal and discharge velocities with tidal elevations being generated by the TPXO7.2 model from which tidal velocities were then calculated, Figure 6.12 b. A velocity representing river discharge, as measured at the Beaver Army Terminal, was also applied to the eastern boundary, Figure 6.12 c.

6.4.2 Salinity and temperature patterns

To illustrate the variation of surface fields in response to wind forcing for the dates when CTD sections along Lines 1,2,3 and 4 were taken, Table (6.1), the average model surface fields of salinity and temperature are examined for similar dates, Figure 6.13. Both salinity (upper row) and temperature (lower row) surface present averaged fields taken over several hours with surface currents superimposed, representing periods of differing wind, tidal and discharge velocities. The grey areas in Figure 6.12 mark the corresponding dates. It is seen that Line 1 was taken during a period of upwelling favourable wind, Line 2 was taken after a 2 days of "calmer" weather, and Lines 3 and 4 at the onset of downwelling favourable winds. There are differences between tidal velocities and river discharge conditions for Lines 3 and 4. Line 3 took place during a period of much smaller tides than Line 4 and river discharge was slightly greater.

The wind plot in Figure 6.12 a, shows that the measurements were started during moderately strong northerly wind that was followed by a weak downwelling favourable wind. Upwelling favourable winds then became re-established as Line 1 measurements began. As was shown in section 6.3.2, the Columbia River plume is directed south-

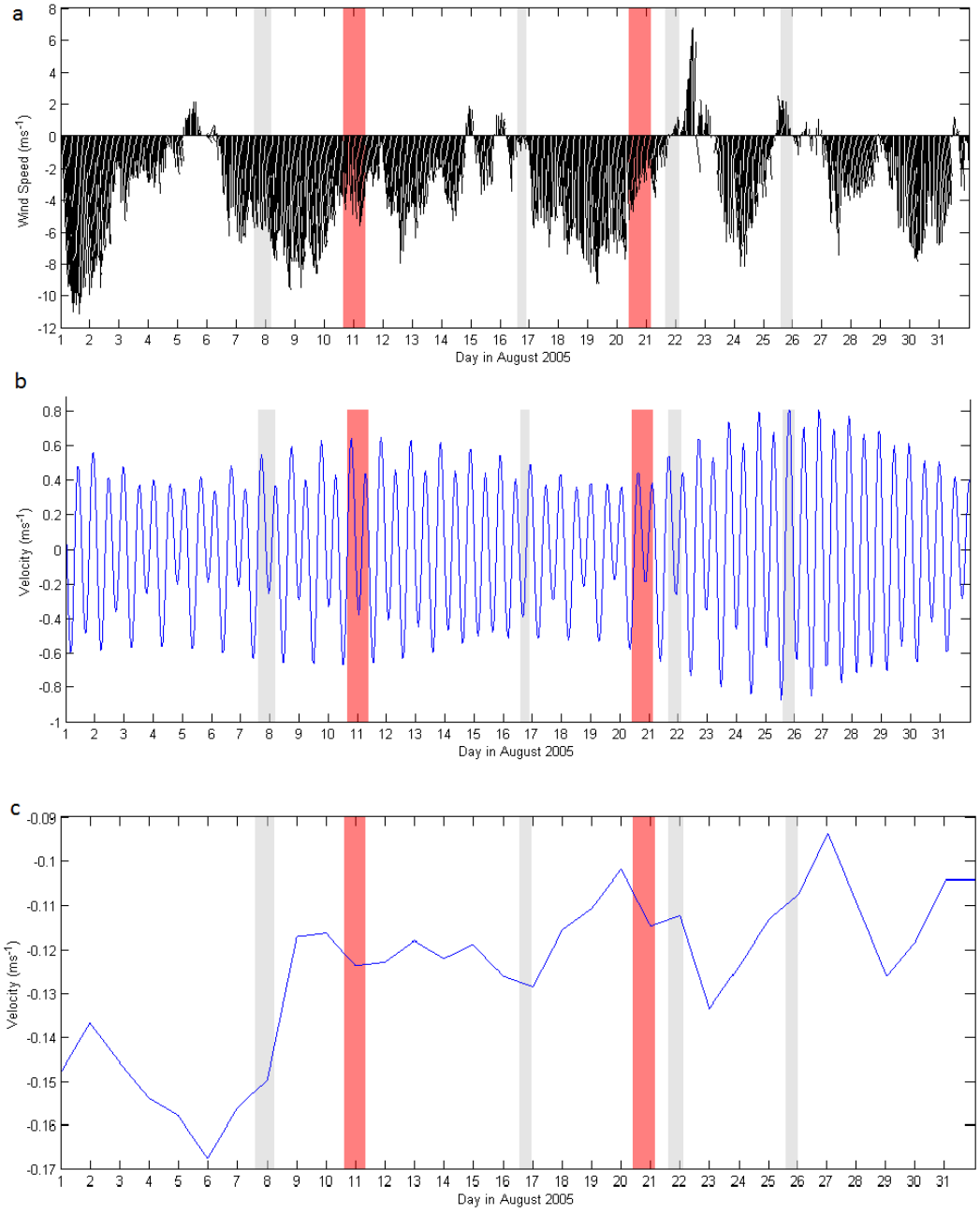

Figure 6.12: Wind, tide and river discharge velocities for August 2005

westward for upewlling winds and northwards when the wind changes direction. For the time Line 1 was taken, the plume is unidirectional to the south and Line 1 crosses a lens that was created earlier in the upwelling event.

After the "calm" period before Line 2 measurements began (Figure 6.12 a) the Columbia River plume returns to it's bi-directional form when fresher water leaving the estuary turns right. The large amount of fresh water to the south is the consequence of the residual currents that were produced during the previous upwelling period. Line 2 intersects the northern branch of the plume.

The development of downwelling favourable patterns can be traced to the dates 21^{st} and 25^{th} when Line 3 and 4 were taken. According to results presented in section 6.3.3, the plume under the action of a southerly wind starts to move north. The main difference between these two cases is the tidal phase. Line 3 was taken during the neaptide and slightly larger discharge compared to the spring tide and smaller discharge during Line 4, Figure 6.12 b and c. Thus, the southern part of the plume is much more pronounced during the time of Line 4 than for Line 3.

Comparison between salinity and temperature fields obtained for the same time-span are presented in Figure 6.13 and show that salinity fields are much more informative than temperature fields and thus further analysis can be restricted to considering only salinity fields. Due to the spatial and temporal sparsity of the observational data it is appropriate to compare cross-sections along the sampling lines rather than the whole domain. In order to do this, model output corresponding with the period of individual CTD casts was combined to produce single cross-sections from data spanning a time range (Figure 6.14). A limitation of the observational data is that it lacks measurements in the top 2 m. Salinity cross-sections show a good general agreement in the location of the plume although the model shows a much fresher lens than was observed. This is likely due to initial estuarine waters being too fresh and not mixing sufficiently within the estuary.

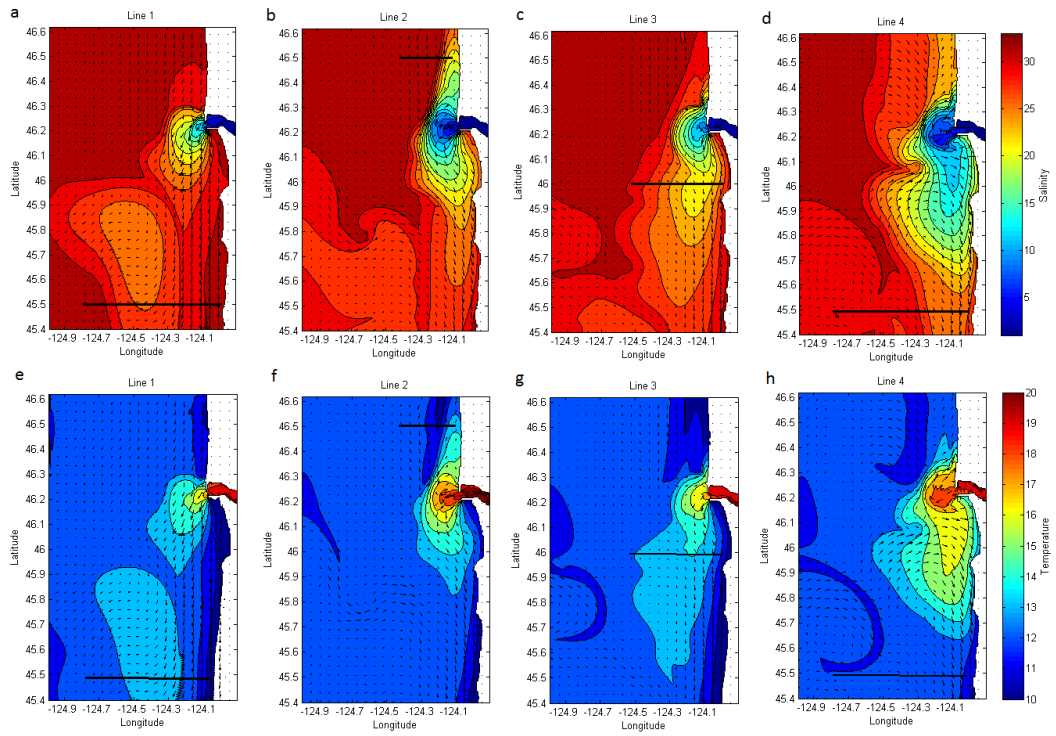

Figure 6.13: Average surface salinity (a to d) and surface temperature (e to h) for the periods of the sampling lines shown by the black lines.

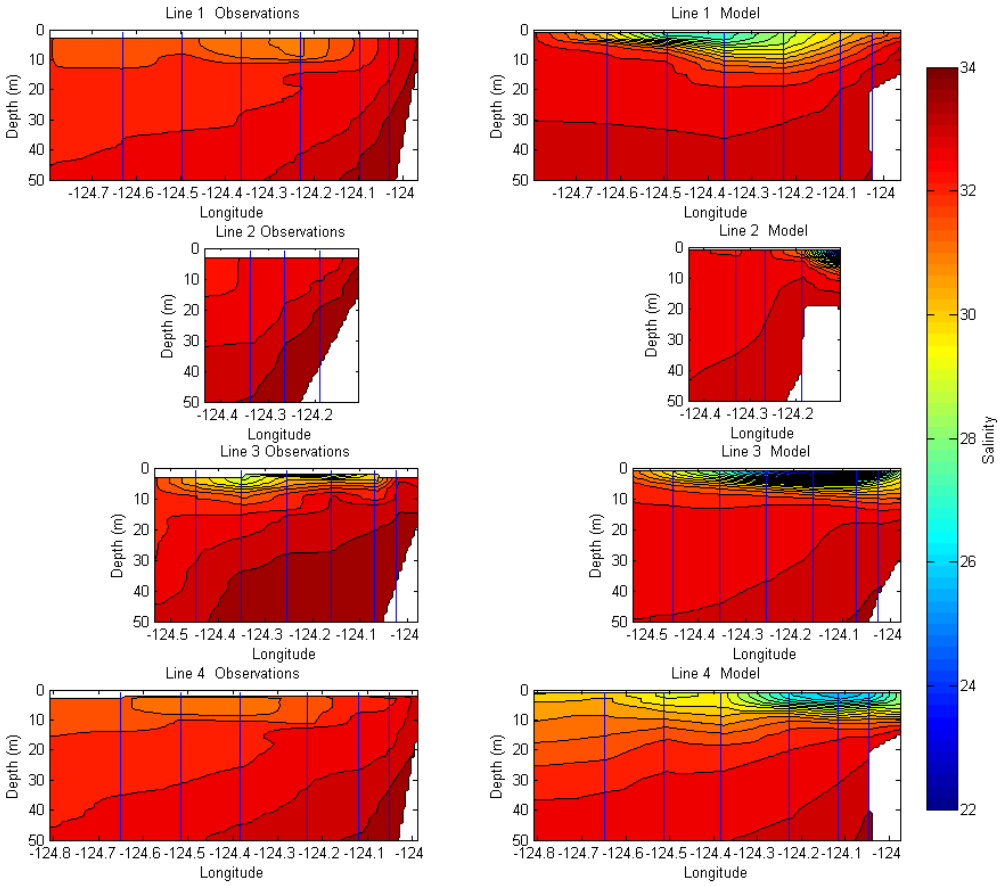

Figure 6.14: Cross-sections of observations (left) and model (right) showing salinity. Blue lines represent the location of CTD casts from which the section is constructed

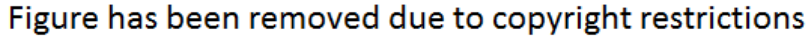

Figure 6.15: Model Salinity field comparison for a)ROMS, b)SELFE from Hickey et al. (2010) and c)MITgcm.

6.4.3 Comparison between models

The two RISE circulation modelling systems ROMS (MacCready et al., 2009) and SELFE (Burla et al., 2010) were used to simulate a realistic circulation of the Columbia River plume in the coastal ocean. MITgcm was used in this study to investigate the behaviour of the plume under conditions seen during the August 2005 cruise. Surface salinity from 3 models for 8th August 2005 are shown at the top of Figure 6.15. The salinity cross sections from the models taken during a 5 hour period are underneath each models surface plot. The bottom row in Figure 6.15 presents the data from CTD observations for this cross section.

The side-by-side comparison highlights some qualitative differences between models. The most dramatic difference is that SELFE salinity structure has much less lateral and vertical structure than ROMS and MITgcm; this may be due to lower order numeric interpolations associated with the semi-Lagrangian time stepping in SELFE.

The ROMS and MITgcm plumes in Figure 6.15 are fresher than the SELFE plume. All three models showed the lens of fresh water that was developed due to the strong upwelling event before the August 5^{th}, Figure 6.4. The position of the lens in ROMS and MITgcm had a similar latitude , however, ROMS and SELFE show an agreement in the longitude of the lens position. A comparison of the vertical sections of salinity through the lens, obtained from all three model runs and observational data, showed better

agreement for the MITgcm salinity section. ROMS has much more upwelling at the coast than SELFE and MITgcm, which does not agree with the observational salinity. ROMS was able to produce similar isohaline inclination to those in the observational data. The failure of MITgcm to generate strong upwelling, for this section, can be explained by the restricted depth of 200 m that was used for these runs.

6.5 Chemistry

The plume of the Columbia River, entering the Pacific Ocean, is the site of numerous oceanographic processes. The plume, being largely comprised of the fresh Columbia River outflow, is easily identified by its low salinity compared to surrounding waters (Stefansson and Richards, 1963). The RISE project in the plume region studied various oceanographic processes, including 1) the physical aspects of sea and river water mixing and the fate of these mixtures, 2) the biological processes which differ between plume and ambient seawater because of the addition of nutrients from the river.

The amount of many soluble nutrients found in the river water differs from the amount found in seawater. Nitrate and silicate concentrations, for example, are much higher in the river water than in the surface ocean water, largely due to biological depletion. The concentration of phosphate, however, is of a similar value. It can be seen in Figure 6.16 from Stefansson and Richards (1963) that during winter, when biological activity is at a low and downwelling conditions are predominant, surface ocean waters have low concentrations of nitrate, silicate and phosphate. Through the halocline these concentrations increase rapidly with depth. Phosphate and nitrate reach a maxima at ≈ 800 m then slightly decrease with depth whilst silicate continues to increase in concentration to the sea floor. Figure 6.16 b shows how the waters of the plume and surrounding waters differs in silicate and nitrate at the surface, yet phosphate concentrations are similar.

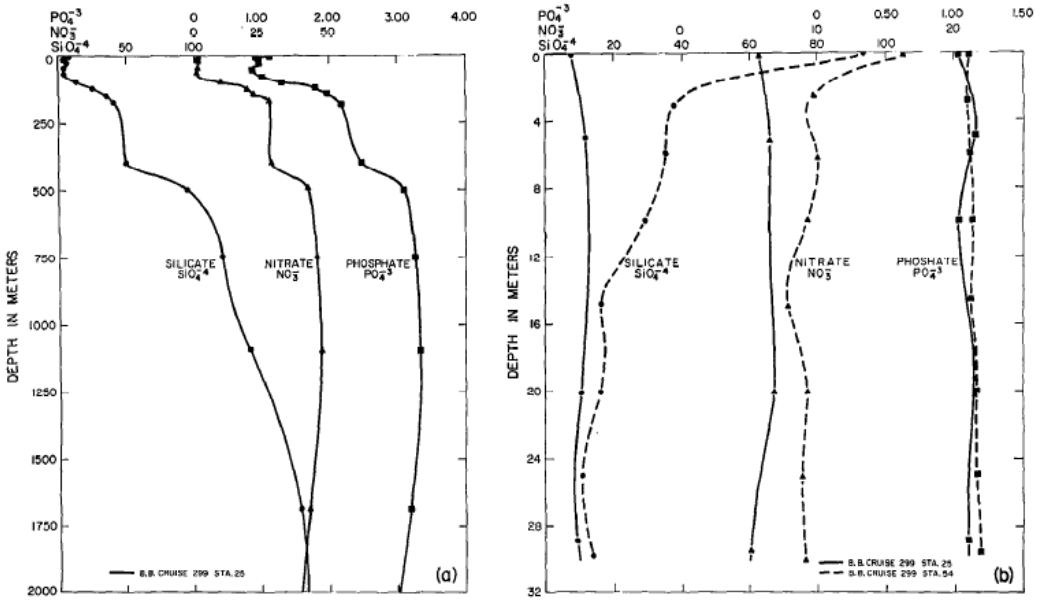

Figure 6.16: Vertical distribution of nutrients a) outside of the Columbia River plume (46°01'N, 126°40'W, 27^{th} January 1962) and b) near the river mouth (46°14'N, 124°10',2^{nd} February 1962), with the shallow water values from a) shown for comparison. All concentrations are in μM)

6.5.1 Comparison of silicate sections from the model and in-situ data

Silicate is the most distinctive of nutrients found in the plume and its distribution obtained during August 2005 has been compared with model results. The concentration of silicate was measured along Lines 1, 2, 3 and 4, where CTD sections were taken (Figure 6.11). The dates and coordinates for lines 1, 2, 3 and 4 are given in Table 6.1.

To set a silicate field into the code of MITgcm an additional equation was used:

$$\frac{\partial C}{\partial t} + u\frac{\partial C}{\partial x} + v\frac{\partial C}{\partial y} + w\frac{\partial C}{\partial z} = K^h\left(\frac{\partial^2 C}{\partial x^2} + \frac{\partial^2 C}{\partial y^2}\right) + K^z\frac{\partial^2 C}{\partial z^2}, \tag{6.12}$$

where C is the silicate concentration.

The vertical distribution of silicate in the open ocean was found from measurements during the August 2005 campaign, Figure 6.17. The value of silicate concentration in the river mouth was 140 μM and was taken from measurements.

Figure 6.18 shows two groups of four vertical sections obtained from the model run (right column) and from observations (left column), along Lines 1, 2, 3 and 4. It should be noted here that some the measurements of silicate were started from a depth of 15 m and therefore the distribution of silicates that come from the river were missing in the surface layer.

The results shown along Line 1 were found during upwelling favourable winds. The coincidence between model results and observations along this line are poor. Line 2 shows a better correlation in spatial distribution, yet the values are still too low near the bottom. The concentration of silicates along Line 3 shows the best coincidence between model and observations. Line 4 shows a better coincidence than the similarly located Line 1 taken earlier in the cruise.

The failure of the model to correctly recreate the silicate distribution, especially along Line 1, can be explained by the initial silicate field not taking into account coastal upwelling. The initial field was horizontally homogeneous and the model response to

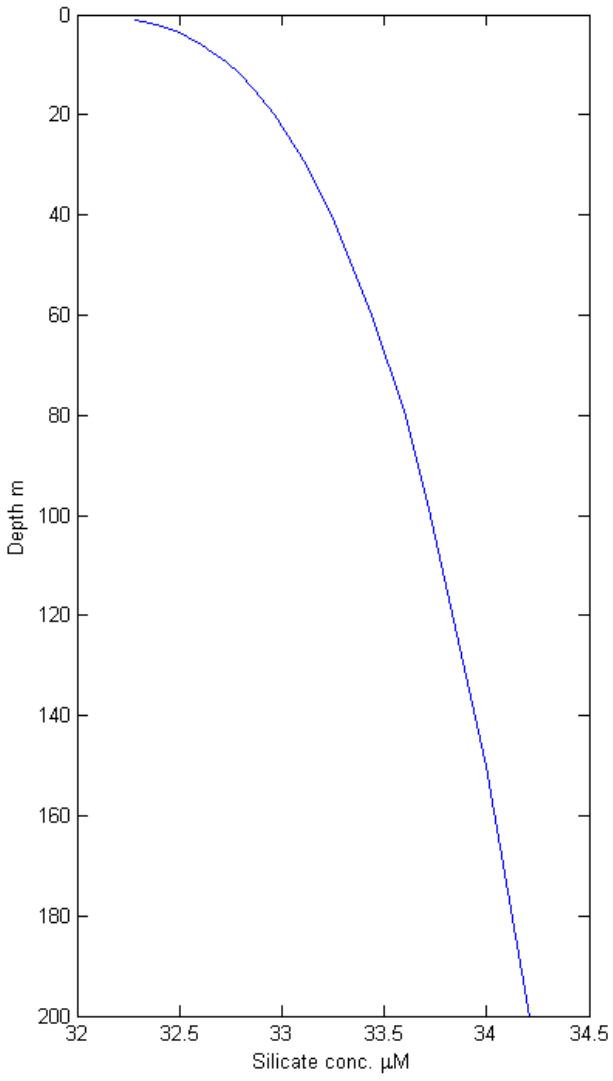

Figure 6.17: Vertical profile of silicate concentration used to initialise the model in the open ocean

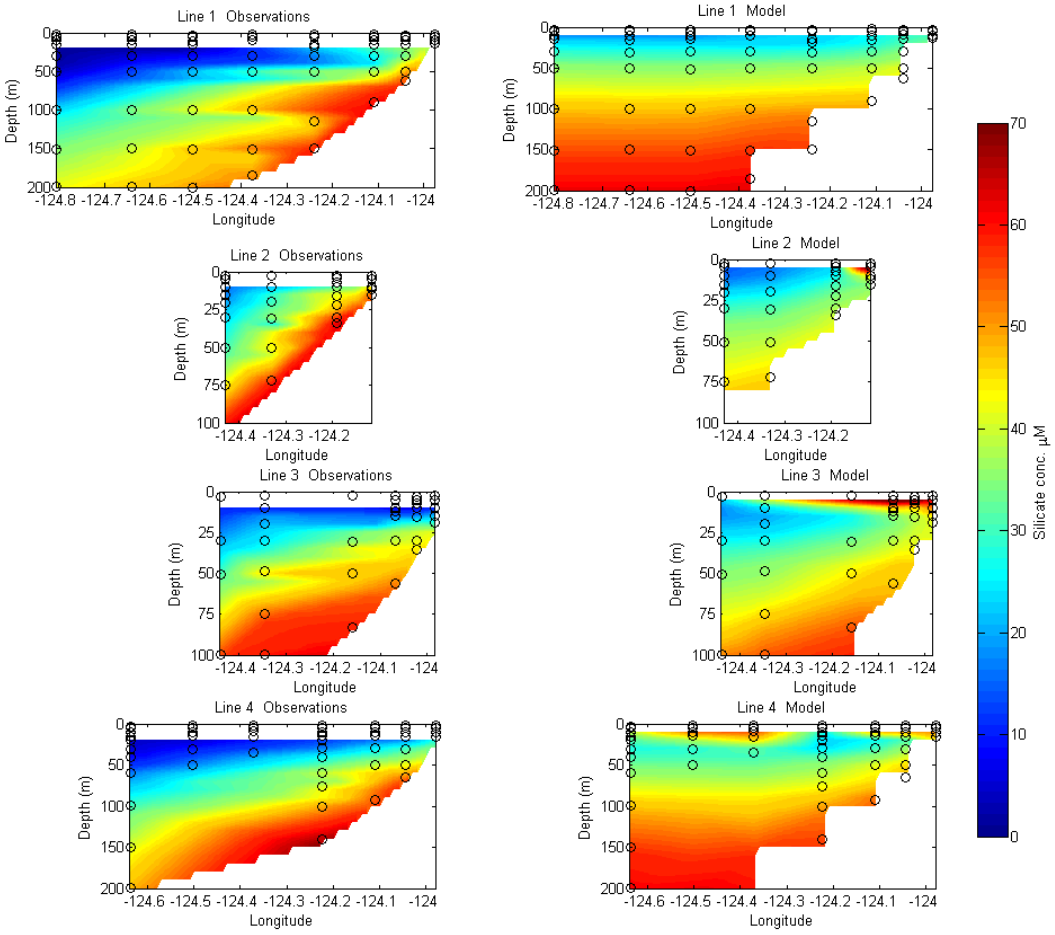

Figure 6.18: Cross-sections of silicate concentration along Lines 1, 2, 3 and 4 for observations (left) and model results (right)

upwelling winds has yet to be fully developed. Adding horizontally variable silicate fields could rectify this situation however conditions across the slope at the beginning of the survey were unknown.

6.5.2 Near-field investigation

A longer-term sampling site located off the Washington-Oregon coast, adjacent to the river mouth (ML in Table 6.1), was included in the RISE program (ML Figure 6.11). For this study, data from point ML taken during RISE 3 aboard RV Wecoma over a whole tidal cycle was considered. The point ML (near-field) was used to investigate the amount of biologically important chemicals that come from the river. In order to determine the concentration of the target nutrients, water samples were taken using a rosette of bottles attached to the CTD. The procedure involved in analysing the water samples, together with the limitation on the number of bottles that can be used on each cast, limited the quantity of data collected. This means the frequency of samples is low compared to CTD measurements and sampling depths are spread further apart. Since the river water has little dissolved salt compared to ocean water, salinity can be used as a tracer for chemicals such as silicate that are found in high quantities in the river water but are depleted in the ocean. The CTD was used to obtain salinity and temperature data at this point with 19 and 20 casts being made on the respective days.

Figure 6.19 shows salinity from the model runs at a horizontal grid point located at position ML for the whole of August 2005 (dashed lines). The measurements taken at point ML are overlaid (solid lines in red areas). There is a good coincidence between in-situ and model salinity for the two periods of sampling at point ML (10-11th and 20-21st August 2005). Wind data, tidal velocity and discharge that correspond to the times indicated by the red areas are presented in Figure 6.12. Figure 6.12 shows that winds were upwelling favourable during both sampling periods, however, tidal velocity and discharge differed. An increase in wind results in an increase in salinity as the

upwelling process brings deep saline waters to the surface where they are entrained into the plume. Given the good agreement between model and observations for the two days presented, it can be assumed that there was a similar agreement for the whole period of the RISE-3 cruise (4^{th} to 26^{th} August 2005). By considering wind, tide and discharge, over the period of the cruise, it is possible to investigate which of these three forcings is most crucial in determining the salinity, and therefore nutrient measurements, at point ML. By comparing the respective velocities of river discharge (Figure 6.12) it can be seen that tidal velocities are far greater than river discharge velocities. This means that the major forcings are wind and tide. By inspection of Figure 6.20 which presents the wind speed overlaid with the tidal velocity envelope (blue) and the normalised silicate concentration (green) expected at point ML, it can be seen that silicate concentration varies with a periodicity greater than the tidal modulation. This suggests that wind events dominate the concentration of silicate in this area with upwelling winds pulling the plume waters away from the coast and bringing up deeper shelf waters balanced against the effects of wind mixing during periods of strong winds.

6.6 Summary remarks on the large-scale investigation

The effect of wind forcing on the dynamics of the Columbia river plume and the distribution on riverine nutrients has been investigated here. Initially, the effect of constant northerly and southerly wind was demonstrated. As theory predicts, (Chao, 1988; Lentz, 2012) the plume acted very differently for the two cases. For the case of upwelling favourable northerly winds, the plume is advected away from the coast, forming a thin lens to the south-west of the river mouth. The downwelling favourable southerly winds produce a narrow plume that remains in contact with the bottom and travels north along the coast. In both cases it was observed that inertial oscillations dominate the internal vertical velocities in the domain for the first 5 days of the run and it is not until 10 days of simulation that these oscillations subside completely leaving only

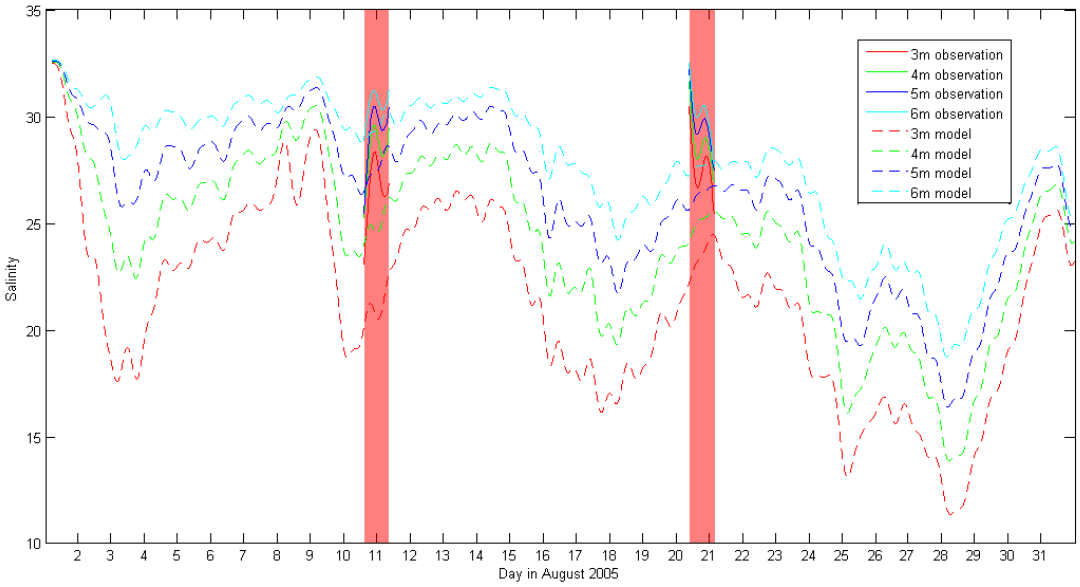

Figure 6.19: Salinities at 3, 4, 5 and 6m at point ML. Model results shown by dashed lines, observations by solid lines

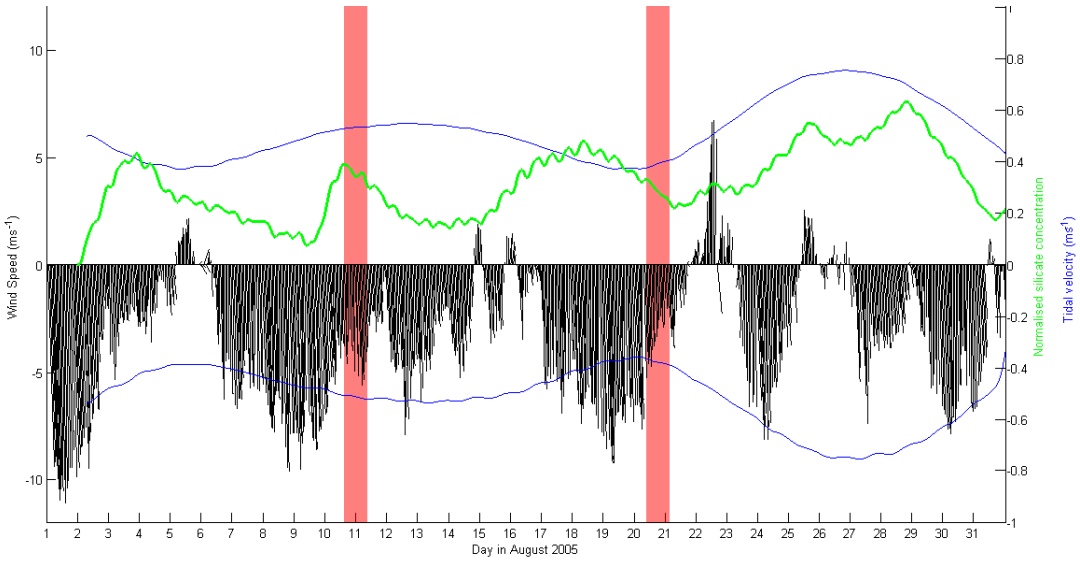

Figure 6.20: Wind speed (black), tidal velocity envelope (blue) and normalised silicate concentration at Ml (green) for August 2005

a tidal signature. This means the results of the modelling simulations can be trusted after this initial period of adjustment to the relatively sudden onset of wind.

The use of realistic wind forcing, taken from in-situ measurements, was next used to force the large-scale model for the period of August 2005, the time during which the RISE-3 samples were taken. This meant the modelling results could be compared to field observations and the results of previous modelling studies, using ROMS (MacCready et al., 2009) and SELFE (Burla et al., 2010). The MITgcm results improve on the previous modelling results when compared to observations taken along Line 1. The fact that the surface distribution of the plume shows similarities between all three models along with the coincidence of the MITgcm results and the observational cross-section indicate that the model is reproducing a realistic hindcast of the plume for this period.

By using a passive tracer field it was possible to produce a representation of silicate concentration in the Columbia River plume and observe how it is distributed as the plume spreads. This investigation had limited success largely due to the horizontally homogeneous initial field. When compared with observations the model did however produce some accurate results, especially later in the run at which point upwelling currents were producing a more correct silicate distribution across the slope. The analysis of observations at the near-field site ML compared to model salinities show a good coincidence. Salinity is also a tracer of the plume and the normalised inverse change in salinity can be interpreted in the near-field as variability in silicate. By comparing this variability over time with the external forcings it is possible to identify the wind as the dominant characteristic in determining silicate concentration at point ML.

6. LARGE-SCALE DYNAMICS OF THE COLUMBIA RIVER PLUME UNDER THE ACTION OF LONG-TERM WIND FORCING

Chapter 7

Conclusions and future recommendations

In this chapter, the findings of this study will be presented along with suggestions as to how the study may be continued in the future.

7.1 Conclusions

This study was successful in meeting its main aims: **(1)** To thoroughly investigate the vertical and horizontal structure and mixing effects produced by the Columbia river plume, including investigation of internal waves generated by the plume, analysis of mixing processes affecting the plume, determining the importance of non-hydrostaticity in modelling the plume and identifying a detailed understanding of near-field circulation. **(2)** To determine the nature of the large-scale dynamics of the plume under the action of wind forcing, including the description of the plume response to upwelling and downwelling winds, investigation into the effect of realistic wind forcing and the influence of plume dynamics on the nutrient circulation associated with the plume.

The objectives of aim **(1)** were met in the following ways. Firstly a high resolution (Δx=Δy=25 m) investigation managed to successfully reproduce an approximation of the near-field river plume. This model has shown that higher mode internal waves are produced at the plume head and that secondary fronts within the plume are a source of further internal waves. It was found that once the plume propagation slowed below 0.3 m s^{-1} the second mode wave separated and propagated freely away from the plume. The amplitude of these second mode waves is comparable to the first mode waves produced and they may produce a significant amount of mixing due to shear instabilities.

The second objective was met by performing an analysis of vertical velocities and plume volume that have resulted in the quantification of the mixing processes within the propagating plume. The use of a passive tracer allowed the boundary of plume water (C=0.1) to be compared to density isopycnals. At the lower boundary of the plume it was shown that entrainment of sea water into the plume was dominant and that seawater comprises 50% of the plume volume after 4 hours. This is biologically significant as it means a larger plume containing nutrients from both the river and sea water is produced which can then be transported across a large area due to spreading and surface forcing.

Thirdly, it was found by comparison of hydrostatic and non-hydrostatic model results, that a hydrostatic model at this model scale does not reproduce the internal wave structure as well as the non-hydrostatic model. The hydrostatic model was, however, still able to reproduce well the plumes spatial distribution. This means that the use of a hydrostatic model will be acceptable for future investigations, that do not aim to resolve the internal waves produced by the plume and only recreate the general spatial structure of the plume.

The last objective of this near-field investigation was also achieved. By the use of 27 Lagrangian drifters within the model at varying depths and horizontal starting locations the 3 dimensional circulation of the near-field plume is identified. The modelled plume surface waters (1 m depth) are shown to be carried offshore and to the north due to Coriolis. This result is in line with observations and theory. Therefore it gives confidence in the accuracy of the model in producing realistic results. It was also shown that the drifter circulation varied with depth and that there was a returning current at the plume boundaries allowing for plume recirculation to take place.

The large scale investigation, aim **(2)**, was also successful in meeting its outlined objectives and produced the following findings: The first objective to be realised was the successful implementation of a large-scale model run for a one month period with

unidirectional constant wind. It was found that for both, the case of northerly upwelling favourable winds and southerly downwelling favourable winds, the modelled plume responded as theory predicts: with a large, thin, south-westerly plume and narrow, thick, coastal plume produced for the respective scenarios . The generation of inertial oscillations caused by the onset of wind forcings was identified and seen to become insignificant after 10 days, at which point only tidal oscillations are observed.

In order to fulfil the next objective, the model was forced with variable realistic wind forcing taken from observations. The model was able to produce an accurate hindcast of the plume region when compared to observations and previous modelling results. In fact, the model outperformed the SELFE model when compared to observations taken along Line 1. These favourable comparisons give confidence that the model is accurately representing the response of the plume to the external forcing and can therefore be used for investigating the distribution of plume waters.

The final objective of this study was to use of nutrient tracer fields and make comparisons with observations. This was achieved, with success in identifying the behaviour of plume waters in the near-field, although far-field results can be improved by using a more representative initial field. Analysis of data from point ML showed that the near-field plume is not greatly influenced by river discharge or variations in the tidal cycle and that the dominant forcing here is the wind, which provides a source of mixing and also upwell silicate rich slope waters.

This study has given insight into the dynamics of the Columbia River plume at a range of scales and shown the value of modelling studies in understanding plume dynamics.

7.2 Future recommendations

The project is regarded as successful, however results presented here can be built on in the future by expanding the study in several ways. Firstly, the investigations into

the production of internal waves could be extended in two main directions. Given sufficient processing power and time it would be interesting to increase the horizontal resolution to less than 10 m in order to determine the effect of non-hydrostaticity on wave generation compared to the hydrostatic results. The second way in which this near-field could be extended is to increase the area represented in the model in order to determine if given sufficient time for the plume to spread and slow the third mode waves will be released and propagate freely beyond the plume.

There are several ways the large-scale investigation could be added to. One of these would be to include a surface heating scheme to the model so that a comparison with observed temperature fields may be undertaken. The next step in the modelling of nutrient distribution would be dependant on further data collection so that horizontally variable tracer fields may be applied to the model. Also, the addition of nutrient sinks and sources could be explored. There is also scope for developing a nested grid, combining a high resolution near-field plume with a larger far-field simulation.

References

Adcroft, A., Campin, C., Dutkiewicz, S., Evangelinos, C., Ferreira, D., Forget, G., Fox-Kemper, B., Heimbach, P., Hill, C., Hill, E., Hill, H., Jahn, O., Losch, M., Marshall, J., Maze, G., Menemenlis, D. and Molod, A. (2011), 'MITgcm User Manual'. **URL:** `http://mitgcm.org/public/r2_manual/latest/` 34, 35

Adcroft, A., Hill, C. and Marshall, J. (1997), 'Representation of topography by shaved cells in a height coordinate ocean model', *Monthly Weather Review* **125**, 2293–2315. 32

Aguilar-Islas, A. M. and Bruland, K. W. (2006), 'Dissolved manganese and silicic acid in the Columbia River plume: A major source to the California current and coastal waters off Washington and Oregon', *Marine Chemistry* **101**, 233–247. 22

Allen, S. E. and Hickey, B. M. (2010), 'Dynamics of advection-driven upwelling over a shelf break submarine canyon', *Journal of Geophysical Research* **115**, C08018. 12

Alpers, W. (1985), 'Theory of radar imaging of internal waves', *Nature* **314**, 245–247. 22

Banas, N. S., MacCready, P. and Hickey, B. M. (2009), 'The Columbia River plume as cross-shelf exporter and along-coast barrier', *Continental Shelf Research* **29**, 292–301. 11, 86

Barnes, C. A., Duxbury, A. C. and Morse, B. A. (1972), Circultaion and selected properties of the columbia river effluent at sea, *in* A. Pruter and D. Alverson, eds, 'The Columbia River Estuary and Adjacent Ocean Waters', University of Washington Press, pp. 41–80. 84

Britter, R. E. and Simpson, J. E. (1978), 'Experiments on the dynamics of a gravity current head', *Journal of Fluid Mechanics* **88**, 223–240. 7

Bruland, K. W., Lohan, M. C., Aguilar-Islas, A Mar-Islas, A. M., Smith, G. J., Sohst, B. and Baptista, A. (2008), 'Factors in fluencing the chemistry of the near-field Columbia River plume: Nitrate, silicic acid, dissolved Fe and dissolved Mn', *Journal of Geophysical Research* **113**, C00B02. 23, 86

Bruland, K. W., Rue, E. L. and J, S. G. (2001), 'Iron and macronutrients in California coastal upwelling regimes: Implications for diatom blooms', *Limnology and Oceanography* **46(7)**, 1661–1674. 15

Burla, M., Baptista, A. M., Zhang, Y. and Frolov, S. (2010), 'Seasonal and interannual variability of the Columbia River plume: A perspective enabled by multiyear simulation databases', *Journal of Geophysical Research* **115**, C00B16. 13, 106, 115

Chant, R. J., Glenn, S. M., Hunter, E., Kohut, J., Chen, R. F., Houghton, R. W., Bosch, J. and Schofield, O. (2008), 'Bulge formation of a buoyant river outflow', *Journal of Geophysical Research* **113**, C01017. 7

Chao, S.-Y. (1988), 'Wind-driven motion of estuarine plumes', *Journal of Physical Oceanography* **18**, 1144–1166. 84, 89, 113

Chao, S.-Y. (1990), 'Tidal Modulation of Estuarine Plumes', *Journal of Physical Oceanography* **20**, 1115–1123. 6

Chao, S.-Y. and Boicourt, B. (1986), 'Onset of estuary plumes', *Journal of Physical Oceanography* **16**, 2137–2149. 6

Csanady, G. T. (1978), 'Wind effects on surface to bottom fronts', *Journal of Geophysical Research* **83**, 4633–4640. 83

Egbert, G. D. and Erofeeva, S. Y. (2002), 'Efficient inverse modeling of barotropic ocean tides', *Journal of Atmospheric and Oceanic Technology* **19**, 183–204. 15

Fiedler, P. C. and Laurs, M. (1990), 'Variability of the Columbia River plume observed in visible and infrared satellite imagery.', *International Journal of Remote Sensing* **11**, 999–1010. 6, 11, 83, 84

Fong, D. A., Geyer, R. W. and Signell, R. P. (1997), 'The wind-forced response on a buoyant coastal current: Observations of the western Gulf of Maine plume', *Journal of Marine Systems* **12**, 69–81. 19, 89

Fong, D. A. and Geyer, W. R. (2001), 'Response of a river plume during an upwelling favorable wind event', *Journal of Geophysical Research* **106**, 1067–1084. 13, 84

Fong, D. A. and Geyer, W. R. (2002), 'The alongshore transport of freshwater in a surface-trapped river plume', *Journal of Physical Oceanography* **32**, 957–972. 83

Garcia Berdeal, I., Hickey, B. and Kawase, M. (2002), 'Influence of wind stress and ambient flow on a high discharge river plume.', *Journal of Geophysical Research* **107**, C9 13–1–13–24. 11, 13, 19, 84

Garrison, T. (1993), *Oceanography: An invitation to marine science*, Wadsworth Publishing company, Belmont. 83

Garvine, R. (1982), 'A steady state model for buoyant surface plume hydrodynamics in coastal waters.', *Tellus* **34**, 293–306. 6

Garvine, R. (1984), 'Radial spreading of buoyant, surface plumes in coastal waters', *Journal of Geophysical Research* **89**, 1989–1996. 70, 78

Garvine, R. W. (1987), 'Estuary plumes and fronts in shelf waters: A layer model', *Journal of Physical Oceanography* **17**, 1877–1896. 6

Garvine, R. W. (1998), 'Penetration of buoyant coastal discharge onto the continental shelf: A numerical model experiment', *Journal of Physical Oceanography* **29**, 1892–1909. 6

Garvine, R. W. and Monk, J. D. (1974), 'Frontal Structure of a River Plume', *Journal of Geophysical Research* **79**, 2251–2259. 6

Gaspar, P., Gregoris, Y. and Lefevre, J.-M. (1990), 'A simple eddy kinetic energy model for simulations of the oceanic vertical mixing: Tests at station Papa and long-term upper ocean study site', *Journal of Geophysical Researchphysical Research* **95**, 16,179–16,193. 41

Geyer, R. W. (1993), 'The importance of suppression of turbulence by stratification on the estuarine turbidity maximum', *Estuaries* **16**, 113–125. 18

Griffiths, R. W. and Hopfinger, E. J. (1983), 'Gravity currents moving along a lateral boundary in a rotating fluid.', *Journal of Fluid Mechanics* **134**, 357–399. 6

Hetland, R. D. (2008), 'Relating river plume structure to vertical mixing', *Journal of Physical Oceanography* **25**, 1667–1668. 13

Hetland, R. D. (2010), 'The effects of mixing and spreading on density in near-field river plumes', *Dynamics of Atmospheres and Oceans* **49**, 37–53. 13

Hickey, B., Geier, S., Kachel, N. and MacFadyen, A. (2005), 'A bi-directional river plume: The Columbia in summer', *Continental Shelf Research* **25**, 1631–1656. 15, 19, 21

Hickey, B. M. (1989), Patterns and processes of circulation over the shelf and slope, *in* M. Landry and B. Hickey, eds, 'Coastal Oceanography of Washington and Oregon', Elsevier Science, pp. 41–109. 84

Hickey, B. M. and Banas, N. S. (2008), 'Why is the northern end of the California Current system so productive?', *Oceanography* **21**, 90–107. 12

Hickey, B. M., Kudela, R. M., Nash, J. D., Bruland, K. W., Peterson, W. T., MacCready, P., Lessard, E. J., Jay, D. A., Banas, N. S., Baptista, A. M., Dever, E. P., Korso, P. M., Kilcher, L. K., Horner-Devine, A. R., Zaron, E. D., McCabe, R. M., Peterson, J. O., Orton, P. M., Pan, J. and Lohan, M. C. (2010), 'River Influences on Shelf Ecosystems: Introduction and synthesis', *Journal of Geophysical Research* **115**, C00B17. 1, 11, 14, 23, 88, 106

Hickey, B. M., Pietrafesa, L. J., Jay, D. A. and Boicourt, W. C. (1998), 'The Columbia River Plume Study: Subtidal variability in the velocity and salinity fields', *Journal of Geophysical Research* **103**, 10339–10368. 6, 84, 89

Hodges, B. R., Laval, B. and Wadzuk, B. M. (2006), 'Numerical error assessment and a temporal horizon for internal waves in a hydrostatic model', *Ocean Modelling* **13**, 44–64. 58

Horner-Devine, A. R. (2009), 'The bulge circulation in the Columbia River plume', *Continental Shelf Research* **29**, 234–251. 6, 7, 12

Horner-Devine, A. R., Jay, D. A., Orton, P. M. and Spahn, E. Y. (2009), 'A conceptual model of a strongly tidal Columbia River plume', *Journal of Marine Systems* **78**, 460–475. 12, 18

Hughes, F. W. and Rattray, M. (1980), 'Salt flux and mixing in the Columbia River Estuary', *Estuarine and Coastal Marine Science* **10**, 479–493. 15, 19

Huq, P. (2009), 'The role of Kelvin number on bulge formation from estuarine buoyant outflows', *Estuaries and Coasts* **32**, 709–719. 6

Jay, D. A., Zaron, E. and Pan, J. (2010), 'Analysis of internal solitary waves generated at the Columbia River plume front using SAR imagery.', *Journal of Geophysical Research* **115, C00B15, doi:10.1029/2008JC004996**, C00B15, doi:10.1029/2008JC004996. 53

Jickells, T. D. (1998), 'Nutrient bigeochemistry of the coastal zone.', *Science* **281**, 217–222. 5

Kilcher, L. F. and Nash, J. D. (2010), 'Structure and dynamics of the Columbia River tidal plume front', *Journal of Geophysical Research* **115**, C05S90. 13, 15

Klymak, J. M. and Legg, S. M. (2010), 'A simple mixing scheme for models that resolve breaking internal waves', *Ocean Modelling* **33**, 224–234. 41

Kourafalou, V. H. (1999), 'Process studies on the Po River plume, North Adriatic Sea', *Journal of Geophysical Research* **104**, 29963–29985. 19

Kourafalou, V. H., Oey, L. Y., Wang, J. D. and Lee, T. N. (1996*a*), 'The fate of river discharge on the continental shelf 1. Modelling the river plume and the inner shelf coastal current', *Journal of Geophysical Research* **101**, 3415–3434. 6, 84

Kourafalou, V. H., Oey, L. Y., Wang, J. D. and Lee, T. N. (1996*b*), 'The fate of river discharge on the continental shelf 2. Transport of coastal low-salinity waters under realistic wind and tidal forcing', *Journal of Geophysical Research* **101**, 3435–3455. 7

Kudela, R. M., Horner-Devine, A. R., Banas, N. S., Hickey, B. M., Peterson, T. D., McCabe, R. M., Lessard, E. J., Frame, E., Bruland, K. W., Jay, D. A., Peterson, J. O., Peterson, W. T., Kosro, M. P., Palacios, S. L., Lohan, M. C. and Dever, E. P. (2010), 'Multiple trophic levels fueled by recirculation in the Columbia River plume', *Geophysical Research Letters* **37**, L18607. 1

Kudela, R. M. and Peterson, T. (2009), 'Influence of a buoyant river plume on phytoplankton nutrient dynamics: What controls standing stocks and productivity?', *Journal of Geophysical Research* **114**, C00B11. 22

Landry, R. M., Postel, J. R., Peterson, W. K. and Newman, J. (1989), Broad-scale distributional patterns of hydrographic variables on the Washington/Oregon shelf, *in* R. Landry and B. Hickey, eds, 'Coastal Oceanography of Washington and Oregon', ElsevierSci, Amsterdam, pp. 1–40. 12

Large, W. G., McWilliams, J. C. and Doney, S. C. (1994), 'Oceanic vertical mixing: A review and a model with a nonlocal boundary layer paraterizaion', *Reviews of Geophysics* **32**, 363–403. 41

Lentz, S. (2004), 'The response of buoyant coastal plumes to upwelling-favourable winds', *Journal of Physical Oceanography* **34**, 2458–2469. 13

Lentz, S. (2012), Buoyant coastal currents, *in* E. Chassignet, C. Cenedese and J. Verron, eds, 'Buoyancy-Driven Flows', Cambridge University Press, pp. 164–202. 83, 85, 91, 113

Lohan, M. C. and Bruland, K. (2006), 'Importance of vertical mixing for additional sources of nitrate and iron to surface waters of the Columbia River plume: Implications for biology', *Marine Chemistry* **98**, 260–273. 1, 7, 22, 23

Luketina, D. A. and Imberger, J. (1987), 'Characteristics of a surface buoyant jet.', *Journal of Geophysical Research* **92**, 5435–5447. 48, 70, 72, 78

MacCready, P., Banas, N. S., Hickey, B. M., Dever, E. P. and Liu, Y. (2009), 'A model study of tide- and wind-induced mixing in the Columbia River Estuary and plume', *Continental Shelf Research* **29**, 278–291. 7, 11, 106, 115

MacDonald, D. G. and Geyer, R. (2004), 'Turbulent energy production and entrainment at a highly stratified estuarine front', *Journal of Geophysical Research* **109**, C05004. 8

Marshall, J., Adcroft, A., Hill, C., Perelman, L. and Heisey, C. (1997), 'A finite-volume, incompressible Navier Stokes model for studies of the ocean on parallel computers', *Journal of Geophysical Research* **102**(C3), 5753–5766. 32, 34

Marshall, J., Hill, C., Perelman, L. and Adcroft, A. (1997), 'Hydrostatic, quasi-hydrostatic, and nonhydrostatic ocean modeling', *Journal of Geophysical Research* **102**(C3), 5733–5752. 30, 32

Masse, A. K. and Murthy, M. R. (1992), 'Analysis of the Niagra River Plume dynamics', *Journal of Geophysical Research* **97**, 2403–2420. 84

McCabe, R. M., Hickey, B. and MacCready, P. (2008), 'Observational estimates of entrainment and vertical salt flux in the interior of a spreading river plume', *Journal of Geophysical Research* **113**, C08027. 66, 72, 73, 75

McCabe, R. M., McCready, P. M. and Hickey, B. M. (2009), 'Ebb tide dynamics and spreading of a large river plume.', *Journal of Physical Oceanography* **39**, 2839–2856. 66, 67, 78

Mellor, G. L. and Yamada, T. (1982), 'Development of a turbulence closure model for geophysical fluid problems', *Reviews of Geophysics and Space Physics* **20**, 851–875. 41

Munchow, A. and Garvine, R. W. (1993), 'Dynamical properties of a buoyancy-driven current', *Journal of Geophysical Research* **98**, 20063–20077. 83

Nash, J. D., Kilcher, L. F. and Moum, J. N. (2009), 'Structure and composition of a strongly stratified tidally pulsed river plume', *Journal of Geophysical Research* **114**, C00B12. 18

Nash, J. D. and Moum, J. N. (2005), 'River plumes as a source of large-amplitude internal waves in the coastal ocean', *Nature* **437**(7057), 400–403. 12, 21, 22, 23, 24, 43, 53, 76

National Oceanic and Atmospheric Administration (2011).
URL: `http://co-ops.nos.noaa.gov/tides04/tab2wc1b.html` 16

Oey, L. and Mellor, G. (1993), 'Subtidal variability of estuarine outflow, plume and coastal current: a model study.', *Journal of Physical Oceanography* **23**, 164–171. 6

Orlanski, I. (1976), 'A simple boundary condition for unbounded hyperbolic flows', *Journal of Computational Physics* **21**, 251–269. 40

Orton, P. M. and Jay, D. (2005), 'Observations at the tidal plume front of a high-volume river outflow', *Geophysical Research Letters* **32**, L11605. 8, 16

Pacanowski, R. C. and Philander, S. G. H. (1981), 'Parameterization of vertical mixing in numerical models of tropical oceans.', *Journal of Physical Oceanography* **11**, 1443–1451. 41

Pan, J. and Jay, D. A. (2009*a*), 'Dynamic characteristics and horizontal transports of internal solitons generated at the Columbia River plume front', *Continental Shelf Research* **29**, 252–262. 12

Pan, J. and Jay, D. A. (2009*b*), 'Effects of ambient velocity shear on nonlinear internal wave associated mixing at the Columbia River plume front', *Journal of Geophysical Research* **114**, C00B07. 12, 53, 62, 76

REFERENCES

Pan, J., Jay, D. A. and Orton, P. M. (2007), 'Analysis of internal solitary waves generated at the columbia river plume front using sar imagery.', *Journal of Geophysical Research* **112**, C07014, doi:10.1029/2006JC003688. 43, 44, 48, 53, 66

Pond, S. and Pickard, G. L. (1983), *Introductory Dynamical Oceanography (2nd Edition)*, Elsevier Butterworth-Heinemann, Oxford, UK. 81

Pritchard, M. and Huntley, D. A. (2002), 'Instability and mixing in a small estaurine plume front', *Estuarine and Coastal Marine Science* **55**, 275–285. 8

Scotti, A. and Mitran, S. (2008), 'An approximated method for the solution of elliptic problems in thin domains: Application to nonlinear internal waves', *Ocean Modelling* **25**, 144–153. 50

Shchepetkin, A. F. and McWilliams, J. C. (2003), 'A method for computing horizontal pressure-gradient force in an oceanic model with a nonaligned vertical coordinate.', *Journal of Geophysical Research* **108**, doi:10.1029/2001JC001047. 88

Shchepetkin, A. F. and McWilliams, J. C. (2005), 'The regional oceanic modeling system (roms): a split-explicit, free-surface, topography-following-coordinate oceanic model.', *Ocean Modelling* **9**, 347–404. 88

Simenstad, C. A., Jay, D. A. and Sherwood, C. R. (1992), Impacts of watershed management on land-margin ecosystems: the Columbia River Estuary as a case study, *in* R. Naimen, ed., 'New Perspectives for Watershed Management - Balancing Long-term Sustainability with Cumulative Environmental Change', Springer-Verlag New York, pp. 266–306. 18

Simpson, J. E. (1982), 'Gravity currents in the laboratory, atmosphere, and ocean.', *Annual Review of Fluid Mechanics* **14**, 213–234. 5

Simpson, J. E. (1997*a*), *Gravity currents in the environment and laboratory. Second Edition*, Cambridge University Press. 7

Simpson, J. H. (1997*b*), 'Physical processes in the ROFI regime.', *Journal of Marine Systems* **12**, 3–15. 5

Souza, A. J. and Simpson, J. H. (1997), 'Controls of stratification in the rhine rofi system', *Journal of Marine Systems* **12**, 311–323. 84

Stashchuk, N. and Vlasenko, V. (2009), 'Generation of internal waves by a supercritical stratified plume', *Journal of Geophysical Research* **114**, C01004. 12, 15, 19, 44, 46, 47, 48, 50, 53, 76

Stefansson, U. and Richards, F. A. (1963), 'Processes contributing to the nutrient distribution off the Columbia River and Strait of Juan de Fuca', *Limnology and Oceanography* **8**, 394–410. 107

Stern, M. E., Whitehead, J. A. and Hua, B. L. (1982), 'The intrusion of a density current along the coast of a rotating fluid.', *Journal of Fluid Mechanics* **123**, 237–265. 6

Thomas, A. C. and Weatherbee, R. A. (2006), 'Satellite-measured temporal variability of the Columbia River plume', *Remote Sensing of Environment* **100**, 167–178. 12, 13

Turner, R. E. and Rabalais, N. N. (1994), 'Coastal eutrophication near the Mississippi river delta', *Nature* **368**, 619–621. 22

U.S. Census Bureau (2010), Coastline Population Trends in the United States: 1960 to 2008, Technical report, U.S. Census Bureau.
URL: `http://www.census.gov/prod/2010pubs/p25-1139.pdf` 1

Vitousek, S. and Fringer, O. B. (2011), 'Physical vs. numerical dispersion in nonhydrostatic ocean modelling', *Ocean Modelling* **40**, 72–86. 50

Walker, N. D. (1994), 'Satellite assessment of Mississippi River plume variability: Causes and predictability.', *Remote Sensing of Environment* **58**, 21–35. 6

Wiseman, W. J. and Garvine, R. W. (1995), 'Plumes and coastal currents near large river mouths', *Estuaries* **18**, 509–517. 6

Yankovsky, A. E. (2000), 'The cyclonic turning and propagation of buoyant coastal discharge along the shelf', *Journal of Marine Research* **58**, 585–607. 83

Yankovsky, A. E. and Chapman, D. C. (1997), 'A simple theory for the fate of buoyant coastal discharges', *Journal of Physical Oceanography* **27**, 1386–1401. 7

Yelland, M. and Taylor, P. T. (1996), 'Wind stress measurements from the open ocean', *Journal of Physical Oceanography* **26**, 541–558. 99

Zhang, Y. and Baptista, A. M. (2008), 'SELFE: A semi-implicit Eulerian-Lagrangian finite-element model for cross-scale ocean circulation.', *Ocean Modelling* **21**, 71–96. 88

Zhang, Y., Baptista, A. M. and Myers, E. P. (2004), 'A cross-scale model for 3D baroclinic circulation in estuary-plume-shelf systems: I. Formulation and skill assessment.', *Continental Shelf Research* **24**, 2187–2214. 88